# STRUCTURAL STUDIES OF ADSORBATE COVERED METAL AND METAL OXIDE SURFACES

A thesis submitted to the University of Manchester

for the degree of PhD

in the Faculty of Engineering and Physical Sciences

2008

**Benjamin G. Daniels**

School of Chemistry



ProQuest LLC.
789 East Eisenhower Parkway
P.O. Box 1346
Ann Arbor, MI 48106 – 1346

# Contents

**Main text word count 27,790**

# List of Figures

# List of tables

# Abstract

Surface X-ray diffraction (SXRD) and scanning tunneling microscopy (STM) have been used to study the geometry of adsorbate covered single crystal surfaces displaying low energy electron diffraction patterns indicating the presence of an expanded surface unit cell.

Surface X-ray diffraction has been employed to study the structure of Ni(110)c(2×2)-CN, focusing primarily on the geometry of the metal substrate. It was concluded that the ordered CN phase produces significant substrate relaxation, but no significant substrate reconstruction was demonstrated. A value of $11 \pm 2\%$ has been derived for the expansion of the spacing between the top two nickel layers, relative to bulk termination. This agrees well with previously published experimental determinations of this parameter and the results of subsequent DFT calculations.

Surface X-ray diffraction has also been used to investigate the structure of $TiO_2$(110)(3×1)-S. In concert with existing STM data it has been shown that on formation of a (3×1)-S overlayer, sulphur adsorbs in a position bridging 6-fold titanium atoms, and all bridging oxygens are lost. Sulphur adsorption gives rise to significant restructuring of the substrate which has been detected as deep as the fourth layer of the selvedge. The replacement of a bridging oxygen atom with sulphur is thought to give rise to a significant motion of co-ordinated 6-fold titanium atoms away from the adsorbate, along with a concomitant rumpling of the second substrate layer.

STM and low energy electron diffraction (LEED) have been used to examine the structure of ordered adlayers of Ca on $TiO_2$(110)-1×1 formed by metal vapor deposition. A comparison is made with structures formed by segregation of Ca from the bulk, with similar structures being found for the two preparation methods below a monolayer coverage. At low coverages, rows with widths in the region of 1 nm develop in the $[1\bar{1}0]$ and [001] azimuths. At coverages equivalent to a single calcium layer, a c(6×2) overlayer is formed. At coverages above a single layer, a disordered structure develops with a LEED pattern indicating a $\begin{pmatrix} 2 & 0 \\ -\frac{1}{5} & 1 \end{pmatrix}$ surface structure.

# Declaration

With the exception of such figures in chapters 1–4 that are explicitly indicated, no portion of the work referred to in this thesis has been submitted in support of an application for another degree or qualification of this or any other university or other institution of learning.

# Copyright statement

iv. Further information on the conditions under which disclosure, publication and exploitation of this thesis, the Copyright and any Intellectual Property Rights and/or Reproductions described in it may take place is available from the Head of School of chemistry(or the Vice-President).

# About the author

The author graduated from the University of Leicester with a 2:1 MPhys (Hons) in 1999, and from the Victoria University of Manchester with an MRes degree in Surface and Interface Science and Technology in 2000. The intervening time has been spent in active research at the University of Manchester School of Chemistry.

## Publications


1. B.G. Daniels, F. Schedin, O. Bikondoa, G. Thornton, and R. Lindsay. A surface X-ray diffraction study of Ni(110)c(2x2)-CN.
   *Surf. Sci*, 572:433–438, 2004.

2. O. Bikondoa, C.L. Pang, C.A. Muryn, B.G. Daniels, S. Ferrero, E. Michelangeli, and G. Thornton. Ordered overlayers of Ca on $TiO_2$(110)-1×1.
   *J. Phys. Chem. B*, 108:16768–16771, 2004.

3. R. Lindsay, E. Michelangeli, B.G. Daniels, M. Polcik, A.Verdini, L. Floreano, A. Morgante, and G. Thornton. Impact of bulk reduction on $TiO_2$(100)/K.
   *Surf. Sci.*, 566:921–925, 2004.

4. R. Lindsay, E. Michelangeli, B.G. Daniels, M. Polcik, A. Verdini, L. Floreano, A. Morgante, J. Muscat, N.M. Harrison, and G. Thornton. Surface to bulk charge transfer at an alkali metal/metal oxide interface.
*Surf. Sci.*, 547:L859–L864, 2003.

5. R. Lindsay, E. Michelangeli, B.G. Daniels, T.V. Ashworth, A.J. Limb, G. Thornton, A. Gutierrez-Sosa, A. Baraldi, R. Larciprete, and S. Lizzit. Impact of defects on the surface chemistry of $ZnO(000\bar{1})$-O.
*J. Am. Chem. Soc.*, 124:7117–7122, 2002.

6. R. Lindsay, B.G. Daniels, and G. Thornton. Geometry of adsorbates on metal oxide surfaces. In *The chemical physics of solid surfaces.* D.P. Woodruff, editor. Elsevier, 2001.

7. B.G. Daniels, R. Lindsay, and G. Thornton. A review of quantitative structural determinations of adsorbates on metal oxide surfaces.
*Surf. Rev. Lett.*, 8:95–120, 2001.

*When in a Search of any Nature the Understanding stands suspended, then Instances of the Fingerpost shew the true and inviolable Way in which the Question is to be decided. These Instances afford great Light, so that the Course of the Investigation will sometimes be terminated by them.*

Francis Bacon

*The interests of a writer and the interests of his readers are never the same and if, on occasion, they happen to coincide, this is a lucky accident.*

Wystan H. Auden

# Acknowledgements

I owe a great debt of thanks to the many people without whose support and expertise this thesis would have not been possible. Particular thanks are due to Rob Lindsay, Paul Howes, Oier Bikondoa and Chris Walker, all of whom have given freely of their time and expertise, and without whose guidance this work would have been impossible. I should also like to thank the many other people who have helped in myriad ways.

At Daresbury; Steve Bennett, George Miller, Alan Porter and Alton Alexander, and particular thanks to Dave Fletcher of the CDS for pandering to my every whim.

Members of the ROD development community who have released their work into the public domain, particularly Olaf Svensson.

From the Department of Chemistry thanks are due to the staff of the electrical and mechanical workshop for their consistently excellent work and assistance, to Dave Gordon for skilled glass blowing, and postgraduate administrators Elaine Smith and Lorraine Onabanjo who have worked tirelessly to remove obstacles from my path.

Thanks to my supervisor Geoff Thornton for his stimulating advice and guidance and to EPSRC for footing the bill.

My special thanks to "Uncle" Chris Muryn for putting up with me for so long, and thanks to past and present members of my research group who have all helped in ways small and large, particularly Tim von Basel, Chi Pang, Adam Limb and Christine Martyniuk. Also thanks to the students and postdocs of the Proctor and Coe groups for their friendship and convivial company.

Many thanks to my mother for her unflagging support in all ways. Thanks to my partner Tom for his love and friendship, and for putting up with far, far, more PhD than he could have ever expected. Thanks also to my friends Adrian and Sophie for their friendship, love and guidance.

Finally thanks to my many colleagues in the wider community who have made trips to conferences, summer schools, and synchrotrons an unalloyed pleasure.

**This thesis is dedicated to my mother, without whose love and support none of this would have been possible.**

# Chapter 1

# Introduction

The Royal Institution was founded more than two hundred years ago to " . . . teach the application of science to the common purposes of life" [1]. Such a view holds with, if anything, greater force today. Governments across the world have identified the application of fundamental research to the development of technology as a key driver of prosperity; for instance the drive for European nations to raise research expenditure to 3% of GDP by 2010 [2]. Interestingly the view that technology is nothing more than applied science is disputed by many of those who study science as a social phenomena — rather the progress of science and technology is described as a complex interplay between the two fields [3].

The history of what is now referred to a surface science has typified this view. Although the field was pioneered in the early twentieth century by a handful of luminaries such as Langmuir, the field only blossomed in response to technological

developments, such as the commercial availability of UHV equipment [4]. Likewise the availability of synchrotron radiation sources, providing intense, tunable X-ray and ultraviolet radiation had a revolutionary effect on the field. The experimental techniques employed in the present work would be impossible without modern, solid state electronics and powerful digital computers.

The designation surface science encompasses a wide and growing field of study encompassing both "hard" and "soft" condensed matter. The surfaces studied range from biological membranes and polymers to single crystal, quasicrystal and polycrystalline metal, semiconductor and metal oxide surfaces. Fundamental studies of surfaces have the potential to inform and influence the discovery and development of diverse technologies; heterogeneous catalysts, corrosion resistant materials, electronic and spintronic devices and bio-compatible materials to name but a few.

The present work is concerned with highly idealised model systems; single crystal substrates prepared in ultra high vacuum environments, with flat, highly ordered surface layers. It is only by the study of such model systems that a deep understanding of the physical and chemical properties of more complex surfaces may be arrived at. In particular, an atomic scale knowledge of the geometry of surfaces is an essential prerequisite of a predictive understanding of surface properties.

In the present work, two widely used and complementary probes of surface structure with quite different capabilities have been employed. Surface X-ray diffraction (SXRD) is one of the few techniques available which is capable of rigorously

determining atomic positions in a surface with high precision. This technique is described in chapter 2; the theory of X-ray scattering from surfaces is outlined, and experimental and analysis methods are described.

As a diffraction technique SXRD is only able to meaningfully probe surfaces which are ordered on a scale of at least 100 Å. Scanning tunneling microscopy, by contrast, is an entirely local probe, capable of resolving individual atoms, and directly yielding real space images of surfaces. Scanning tunneling microscopy is considered in chapter 3, where some key theoretical results are described and the apparatus and experimental methods employed are described.

Chapter 4 briefly describes the surface preparation methods used, including UHV compatible sources of adsorbates, and ancillary surface characterisation techniques.

Chapter 5 and chapter 6 describe surface structure studies employing SXRD. In chapter 5 an investigation of Ni(110)c(2×2)-CN is described, whilst chapter 6 contains an account of the study of the $TiO_2$(110)(3×1)-S surface. In chapter 7 an STM study of ordered calcium overlayers on the $TiO_2$(110)-1×1 surface is described. The presented work is summarised in chapter 8, where future work is also discussed.

The substrate materials employed in this work are described in the remaining part of this chapter.

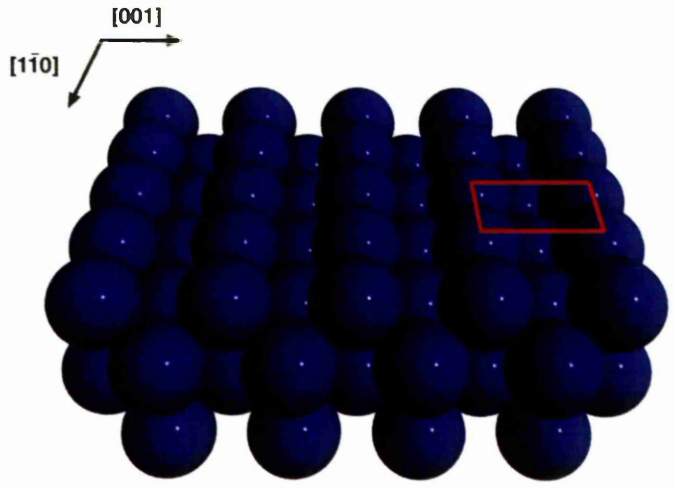


Figure 1.1: Hard sphere model of the Ni(110) surface. A 1×1 unit cell is outlined on the right.

## 1.1 Ni(110)

Nickel crystallises in the face centered cubic structure, with a cell size $a_0 = 3.52$ Å, and nearest neighbour bond lengths of 2.48 Å. The Ni(110)-(1×1) surface is characterised by rows of Ni atoms oriented in the [1$\bar{1}$0] direction, the rows are separated by $\frac{1}{\sqrt{2}}a_0 = 2.48$ Å. A hard sphere model of the surface is shown in figure 1.1. The (110) surface retains an ABAB ... packing, with nickel atoms in the second layer offset by $\frac{1}{2\sqrt{2}}a_0 = 1.24$ Å in the [001] and [1$\bar{1}$0] directions. The surface unit cell measures $a_0 \times \frac{1}{\sqrt{2}}a_0 = 3.52 \times 2.48$ Å. A number of LEED and ion scattering studies have elucidated the structure of this surface [5–8]. Symmetry constraints imply that only relaxations perpendicular to the surface are present; the outer layer contracts by approximately 9%, in common with observations of many simple metal surface [9]. The second to third layer spacing increases by around 3.5% from the bulk value.

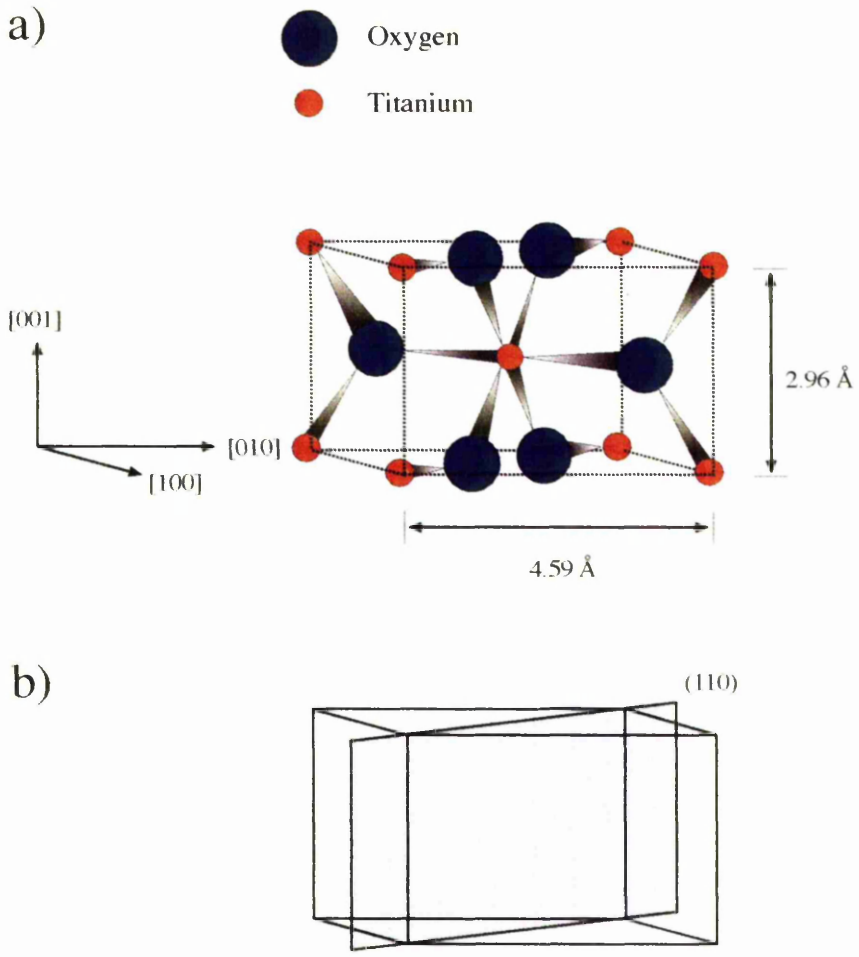


Figure 1.2: a) The bulk unit cell of rutile $TiO_2$. Large spheres represent oxygen atoms, small spheres represent titanium atoms. b) Schematic representation of the intersection of the (110) plane with the bulk unit cell. Reproduced from [10].

## 1.2 $TiO_2$(110)

Titanium dioxide is usually found in the rutile or anatase polymorphs. Whilst the majority of surface studies have concentrated on rutile surfaces, there has recently been increased interest in anatase surfaces, for instance [11] and references therein.

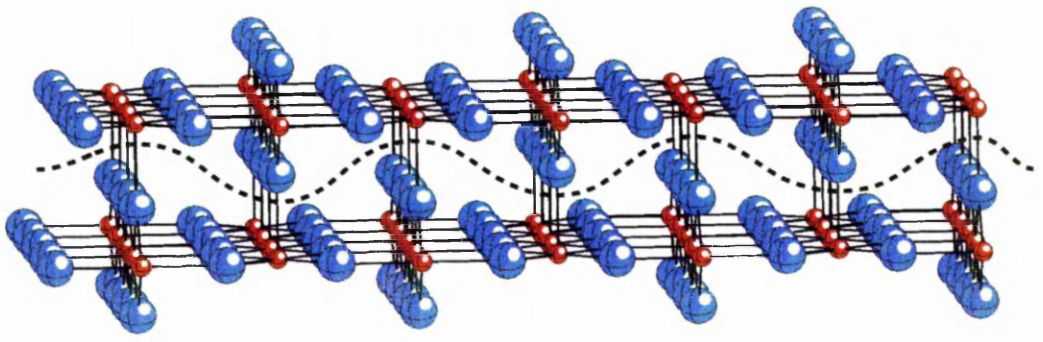

Figure 1.3: Ball and stick model illustrating formation of the $TiO_2(110)$ surface — cleavage occurs long the plane indicated with a dotted line. The large spheres represent titanium atoms, small spheres represent oxygen atoms. Reproduced from [10].

Bulk rutile $TiO_2$ possess a tetragonal unit cell with dimensions of 2.96 × 4.59 Å, with titanium atoms at the corners and a distorted $TiO_6$ octahedron at the center of the unit cell, see figure 1.2. Distortion of the octahedra means titanium co-ordinates to four oxygens at a distance of 1.94 Å and a further two at 1.99 Å. Although $TiO_2$ is partially ionic, its bonds also have some covalent character due to significant overlap between O 2p and Ti 3d orbitals. Whilst $TiO_2$ has a large (3 eV) band gap, and is insulating when stoichiometric, high temperature UHV annealing creates titanium interstitials which, in effect, *n*-dope the lattice, increasing bulk conductivity [12]. This property opens up the possibility of studying $TiO_2$ surfaces with scanning tunneling microscopy and electron spectroscopies.

The formation of a $TiO_2(110)$-1×1 surface can be imagined as the cleavage resulting in the severance of the longest Ti–O bonds (figure 1.3), this reduces the co-ordination of atoms on the newly created surface by the smallest possible

amount. The resulting surface is characterised by bridging oxygen rows running in the [001] direction; titanium atoms situated underneath these oxygen atoms are 6-fold co-ordinated. Parallel with, and equidistant between the bridging oxygen rows, in the plane of the surface, is a row of 5-fold co-ordinated titanium atoms. Both 5 and 6-fold titanium atoms co-ordinate to 3-fold co-ordinated "in-plane" oxygen atoms. The unit cell of the 1×1 surface measures 6.50 by 2.96 Å, and is indicated on the surface model in figure 1.4. The structure of the $TiO_2$(110)-1×1 surface has excited much interest, with a consensus between structures determined by a variety of experimental and theoretical methods only emerging recently [13, 14].

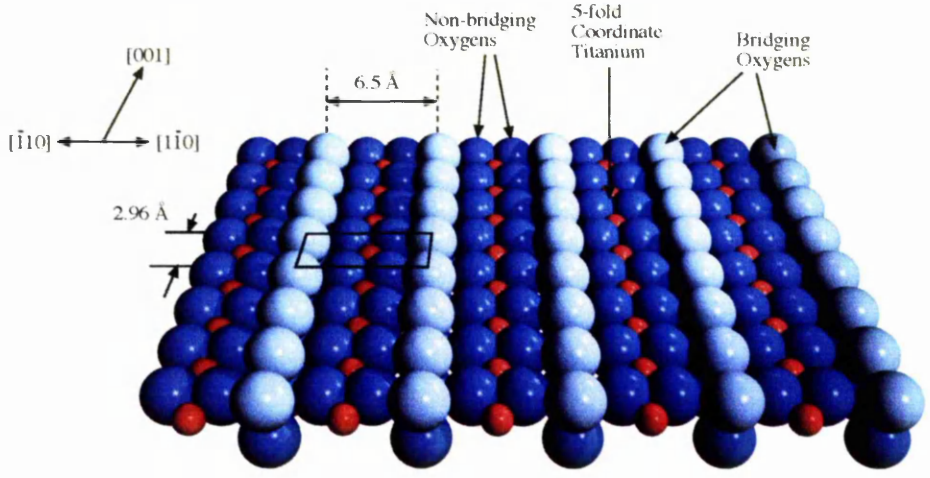


Figure 1.4: Hard sphere model of the $TiO_2$(110) surface. The large spheres represent oxygen atoms, the small spheres titanium atoms. Reproduced from [15].

# References


[1] M. Berman. *Social change and scientific organization – The Royal Institution, 1799–1844.* 1978.

[2] More research for Europe; Towards 3% of GDP, 2003. Communication from the European commission — available at http://europa.eu.int/comm/research/era/pdf/com3percent_en.pdf.

[3] W. Bauchspies, J. Croissant, and S. Restivo. *Science, Technology, and Society: A Sociological Perspective.* Oxford: Blackwell, 2005.

[4] C.B. Duke, editor. *Surface Science – The first thirty years.* North-Holland, 1994.

[5] W. Reimer, V. Penka, M. Skottke, R.J. Behm, G. Ertl, and W. Moritz. *Surf. Sci.*, 186:45–54, 1987.

[6] S.M. Yalisove, W.R. Graham, E.D. Adams, M. Copel, and T. Gustafsson. *Surf. Sci.*, 171:400–414, 1986.

[7] M.L. Xu and S.Y.Tong. *Phys. Rev. B*, 31:6332–6336, 1985.

[8] D.L. Adams, L.E. Petersen, and C.S. Sorensen. *J. Phys. C*, 18:1753–1766, 1985.

[9] M.A. van Hove. *Structure of solids.* Verlag Chemie, 1991.

[10] A.J. Limb. *Scanning Tunnelling Microscopy: Studies of Fe, Cr and $SO_2$ Adsorption on Rutile $TiO_2$ (110).* PhD thesis, University of Manchester, 2002.

[11] A.G. Thomas, W.R. Flavell, A.K. Mallick, A.R. Kumarasinghe, D. Tsoutsou, N. Khan, C. Chatwin, S. Rayner, G.C. Smith, R.L. Stockbauer, S. Warren, T.K. Johal, S. Patel, D. Holland, A. Taleb, and F. Wiame. *Phys. Rev. B*, 75:035105, 2007.

[12] U. Diebold. *Surf. Sci. Rep.*, 48:53–229, 2003.

[13] G. Cabailh, X. Torrelles, R. Lindsay, O. Bikondoa, I. Joumard, J. Zegenhagen, and G. Thornton. *Phys. Rev. B*, 75:241403, 2007.

[14] R. Lindsay, A. Wander, A. Ernst, B. Montanari, G. Thornton, and N.M. Harrison. *Phys. Rev. Lett.*, 94:246102, 2005.

[15] T.V. Ashworth. *Scanning Probe Microscopy studies on Metal Oxide Surfaces.* PhD thesis, University of Manchester, 2003.

# Chapter 2

# Surface X-ray diffraction

## 2.1 Introduction

Bulk X-ray diffraction is long established as a routine technique which may determine bulk structures of considerable complexity. Surface X-ray diffraction (SXRD) is one of the few techniques which can be used to rigorously determine surface structures with precision as small as 0.01 Å. The strong penetration of X-rays mean that the technique is equally suited to use in UHV and to the study of gas-solid, liquid-solid and solid-solid interfaces. In contrast to electron diffraction techniques, single scattering calculations are sufficient, thus the calculation of theoretical data sets may be undertaken in seconds rather than hours. However, to undertake SXRD measurements on a realistic time scale requires a very intense X-ray source, and in practice, SXRD studies are confined to synchrotron radiation sources. A number of authors have published comprehensive reviews of practical and theoretical aspects of SXRD [1–4].

In the first section of this chapter the theory of SXRD is described. The SXRD studies presented in chapters 5 and 6 were undertaken at beamline 9.4 of the synchrotron radiation source (SRS), Daresbury; in the second section of this chapter the experimental apparatus employed, including beamline instrumentation and UHV chamber are described. In the final section, analysis of SXRD data is described.

## 2.2 Theoretical considerations

In this section, key results in the kinematic theory of X-ray scattering are derived and their application to surface X-ray diffraction is outlined. The present treatment owes much to the work of Als-Nielson [5], Fiedenhansl'l [1], Robinson [2] and Howes [6].

The scattering cross section of X-rays is much smaller than that of electrons, thus the scattering of X-rays may be adequately described by assuming single scattering — the kinematic approximation [5]. Inelastic or Compton scattering may also be neglected as it will not give rise to coherent diffraction features. If $\mathbf{k_i}$ represents an incident wave vector in momentum space, and $\mathbf{k_f}$ represents the wave vector of a scattered wave, then for elastic scattering:

$$|\mathbf{k_f}| = |\mathbf{k_i}| \tag{2.1}$$

$$\mathbf{k_f} - \mathbf{k_i} = \mathbf{Q} \tag{2.2}$$

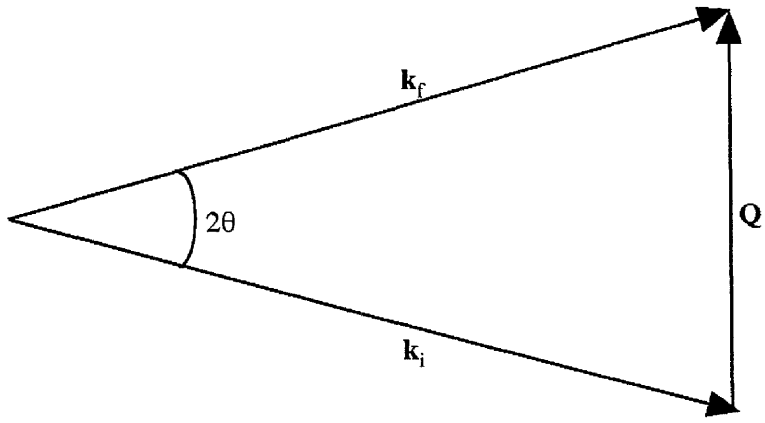


Figure 2.1: Incident and exit wave vectors for the case of elastic scattering

where **Q** is the scattering vector equal to the momentum transfer on scattering. This is illustrated in figure 2.1.

### 2.2.1 Atomic form factor

The scattering of an incident plane wave by a single electron is first considered. The incident plane wave will be scattered into a spherical wave with electric field amplitude $E$ given by the Thompson formula [7], provided that the amplitude of the scattered wave is negligible as compared to the incoming wave, and that the point of observation at a radius $R$ is a large distance from the electron at a position defined by a vector **r** then:

$$\mathbf{E}(\mathbf{Q}) = E_0 \frac{e^2}{mc^2 R} P^{\frac{1}{2}} \mathrm{e}^{i(\mathbf{Q}.\mathbf{r})} \tag{2.3}$$

where $E_0$ is the amplitude of the incident wave and $P$ is the polarisation factor which is introduced to account for trigonometric variation in acceleration of the electron seen by an observer moving in the plane of the incident wave.

If an atom is considered as an electron cloud described by a density distribution function $\rho(\mathbf{r}')$, then the amplitude of scattering by an isolated atom is given by integrating over the electron distribution function around the atom position $\mathbf{r}$ [7]:

$$\mathbf{E}_{atom}(\mathbf{Q}) = E_0 \frac{e^2}{mc^2 R} P^{\frac{1}{2}} \int \rho(\mathbf{r}') \mathrm{e}^{i\mathbf{Q}.(\mathbf{r}+\mathbf{r}')} d\mathbf{r}' \tag{2.4}$$

and

$$\mathbf{E}_{atom}(\mathbf{Q}) = E_0 \frac{e^2}{mc^2 R} P^{\frac{1}{2}} \mathrm{e}^{i(\mathbf{Q}.\mathbf{r})} \int \rho(\mathbf{r}') \mathrm{e}^{i\mathbf{Q}.(\mathbf{r}')} d\mathbf{r}' \tag{2.5}$$

Thus the atomic form factor can then be defined as the Fourier transform of the electron density:

$$f(\mathbf{Q}) = \int_{atom} \rho(\mathbf{r}) \mathrm{e}^{i\mathbf{Q}.\mathbf{r}} d\mathbf{r} \tag{2.6}$$

and equation 2.5 now becomes:

$$\mathbf{E}_{atom}(\mathbf{Q}) = E_0 \frac{e^2}{mc^2 R} P^{\frac{1}{2}} f(\mathbf{Q}) \mathrm{e}^{i\mathbf{Q}.\mathbf{r}} \tag{2.7}$$

It is apparent that scattering will be dominated by electrons — the ratio of charge to mass will be roughly two thousand times smaller in the case of protons in the nucleus. A comprehensive tabulation of calculated form factors is given in [8], though a convenient empirical approximation is generally used in crystallographic software [5]. Although values from both sources do not account for the presence of chemical bonds, they are generally adequate for the work of the present kind.

It is convenient to ignore constant factors and define the scattering amplitude as:

$$A_{atom}(\mathbf{Q}) = f(\mathbf{Q}) \mathrm{e}^{i\mathbf{Q}.\mathbf{r}} \tag{2.8}$$

### 2.2.2 Diffraction by a lattice

A bulk crystal may be described by a stacking of repeated unit cells. The periodic lattice of unit cells is described by a vector $\mathbf{R}$, defined as:

$$\mathbf{R} = n_1\mathbf{a_1} + n_2\mathbf{a_2} + n_3\mathbf{a_3} \tag{2.9}$$

where $n_1, n_2, n_3$ are integers, and $\mathbf{a_1}, \mathbf{a_2}, \mathbf{a_3}$ are the basis vectors of the lattice. The position of the $j$th atom in a unit cell is given by the vector $\mathbf{r_j}$, hence the position of an atom in the crystal is given by:

$$\mathbf{R} + \mathbf{r_j} \tag{2.10}$$

The scattering amplitude of the crystal is then given by the phase sum of the individual scattering amplitudes of the constituent atoms:

$$A^{\,crystal}(\mathbf{Q}) = \sum_{j,n_1,n_2,n_3} f_j(\mathbf{Q}) e^{i\mathbf{Q}.(\mathbf{R}+\mathbf{r_j})} \tag{2.11}$$

which factorises to:

$$A^{\,crystal}(\mathbf{Q}) = \sum_{r_j} f_j(\mathbf{Q}) e^{i(\mathbf{Q}.\mathbf{r_j})} \sum_{R} e^{i(\mathbf{Q}.\mathbf{R})} \tag{2.12}$$

The left hand term is the sum of contributions to the scattering from the atoms in one unit cell — this defines the structure factor $F(\mathbf{Q})$. By comparison with equation 2.6 the structure factor can be seen to be the Fourier transform of the electron density function of the unit cell, $\rho_u$:

$$F(\mathbf{Q}) = \sum_{r_j} f_j(\mathbf{Q}) e^{i(\mathbf{Q}.\mathbf{r_j})} = \int_{unit\ cell} \rho_u(\mathbf{r}) e^{i(\mathbf{Q}.\mathbf{r})} d\mathbf{r} \tag{2.13}$$

Equation 2.12 now becomes:

$$A^{\,crystal}(\mathbf{Q}) = F(\mathbf{Q}) \sum_{R} e^{i(\mathbf{Q}.\mathbf{R})} \tag{2.14}$$

The right hand term is a summation over the lattice defined by the vector $\mathbf{R}$. This sum will take on an appreciable value only when contributions from the whole crystal add in-phase:

$$\mathbf{Q}.\mathbf{R} = 2n\pi \quad \text{where} \quad n = integer \tag{2.15}$$

Solutions may be found by constructing a lattice in wave vector space. Reciprocal lattice vectors $\mathbf{b_j}$ are defined such that:

$$\mathbf{a_i} \cdot \mathbf{b_j} = 2\pi\delta_{i,j} \tag{2.16}$$

where $\delta_{i,j}$ is the Kronecker delta which takes a value of unity when $i = j$ and is zero otherwise. Thus points in reciprocal space are defined by vectors of the form:

$$\mathbf{G} = h\mathbf{b}_1 + k\mathbf{b}_2 + l\mathbf{b}_3 \tag{2.17}$$

where $h, k, l$ take integer values which are the Miller indices. Taking the scalar product:

$$\mathbf{G}.\mathbf{R} = 2\pi(hn_1 + kn_2 + ln_3) \tag{2.18}$$

The terms in the brackets on the right hand side are all integer, so equation 2.15 is satisfied when:

$$\mathbf{G} = \mathbf{Q} \tag{2.19}$$

Hence there will be an appreciable intensity of scattered X-rays only when the momentum transfer $\mathbf{Q}$ coincides with a reciprocal space vector $\mathbf{G}$ — the Laue condition [5]. An alternative statement of the Laue condition which satisfies

equation 2.15 is:

$$\begin{aligned} \mathbf{a_1}.\mathbf{Q} &= 2\pi h \\ \mathbf{a_2}.\mathbf{Q} &= 2\pi k \\ \mathbf{a_3}.\mathbf{Q} &= 2\pi l \end{aligned} \tag{2.20}$$

A more rigorous treatment [5] takes the electron density to be the convolution the lattice sum and the unit cell electron density, and demonstrates that where the Laue condition is met, the resulting diffraction peaks take the form of sharp delta functions. The introduction of a shape function demonstrates that in real crystals of finite size, the delta functions are broadened to sinc functions.

If the real space positions of atoms within the unit cell are expressed in fractional co-ordinates of the basis vectors:

$$\mathbf{r_j} = x_j\mathbf{a_1} + y_j\mathbf{a_2} + z_j\mathbf{a_3} \tag{2.21}$$

from equations 2.16 and 2.17, the structure factor (equation 2.13) can now be given as:

$$F_{hkl} = \sum_j f_j \mathrm{e}^{2\pi i(hx_j+ky_j+lz_j)} \tag{2.22}$$

Thermal vibration scatters intensity into an incoherent background reducing the intensity of diffraction features. This effect is more pronounced at large momentum transfers, and can be accounted for by introducing a prefactor into the summation in the equation above.

$$F_{hkl} = \sum_j f_j \mathrm{e}^{\frac{-B_j Q^2}{16\pi^2}} \mathrm{e}^{2\pi i(hx_j+ky_j+lz_j)} \tag{2.23}$$

where the Debye-Waller factor $B$ is related to the mean square thermal vibration amplitude $< u^2 >$ as:

$$B = 8\pi^2 < u^2 > \tag{2.24}$$

### 2.2.3 Surface diffraction

The presence of a surface breaks the periodicity of a crystal, giving rise to a lattice which is semi-infinite in the direction perpendicular to the surface. Consequently the Laue condition is relaxed perpendicular to the surface. Scattering is no longer isotropic, with streaks of diffracted intensity appearing perpendicular to the surface, passing through the bulk diffraction points — crystal truncation rods (CTRs). The crystal remains infinite parallel to the surface, and the transverse shape of the CTRs is still described by delta functions. This is shown schematically in figure 2.2.

The general form of the CTRs can be elucidated by representing the surface as the multiplication of the electron density function of the crystal lattice $\rho_{lattice}(\mathbf{z})$, by a step function $s(\mathbf{z})$, where $\mathbf{z}$ represents the direction perpendicular to the surface. The scattered amplitude will be given by the Fourier transform of the resulting electron density, which is equivalent to the convolution of the Fourier transform of $\rho_{lattice}(\mathbf{z})$ and the Fourier transform of $s(\mathbf{z})$. The former is a delta function, and the latter equal to $i/q_z$ , where $q_z$ is momentum transfer away from the Bragg points, thus scattered amplitude falls as $1/q_z$ [2, 5].

An expression for the intensity distribution of a CTR can be derived by a straight

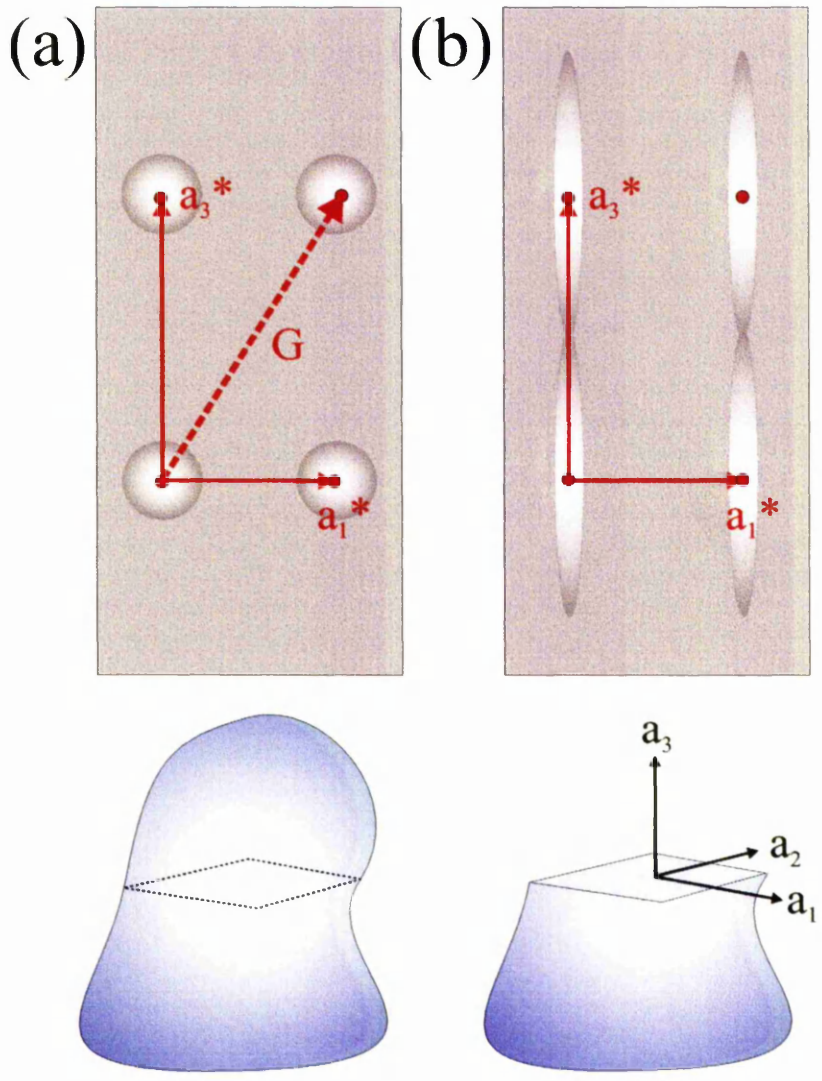


Figure 2.2: a) Reciprocal space map (top) of a large crystal (bottom). b) Reciprocal space map resulting from creation of a surface, showing streaks of scattering perpendicular to the surface. Taken from *Elements of Modern X-ray Physics* by Jens Als-Nielsen and Des McMorrow. Copyright John Wiley and Sons Limited 2001. Reproduced with permission.

forward method due to Robinson [2]. The scattered amplitudes from successive layers $A(\mathbf{Q})$ are summed with a suitable phase factor. If the attenuation of X-rays by the sample is neglected:

$$F^{CTR} = A(\mathbf{Q}) \sum_{j=0}^{\infty} \mathrm{e}^{iQ_z a_3 j} = \frac{A(\mathbf{Q})}{1 - \mathrm{e}^{iQ_z a_3}} \tag{2.25}$$

where $Q_z$, the momentum transfer along the surface normal can be taken to be:

$$Q_z = \frac{2\pi l}{a_3} \tag{2.26}$$

Hence:

$$F^{CTR} = \frac{A(\mathbf{Q})}{1 - \mathrm{e}^{i2\pi l}} \tag{2.27}$$

The intensity distribution of the CTR is then given by:

$$I^{CTR} = |F^{CTR}|^2 = \frac{|A(\mathbf{Q})|^2}{(1 - \mathrm{e}^{i2\pi l})(1 - \mathrm{e}^{-i2\pi l})} = \frac{|A(\mathbf{Q})|^2}{4\sin^2(\pi l)} \tag{2.28}$$

Scattering amplitude diverges at integer values of $l$ when the Laue condition is met, but scattering between these points is non-zero. A $\pi$ change in the phase of the scattered wave occurs at the Bragg peaks.

In the kinematic approximation the total scattered amplitude can be given simply as the phase sum of bulk and surface scattering [2]:

$$F_{hk}^{sum}(l) = F_{hk}^{bulk}(l) + F_{hk}^{surface}(l) \tag{2.29}$$

where $F_{hk}^{surface}(l)$ is simply the sum of scattering over the surface unit cell. This has the advantage that scattering is simply divided into contributions from the bulk and from a "surface" region, representing an arbitrary number of atomic layers of the selvedge. Both the bulk and surface structure now contribute to

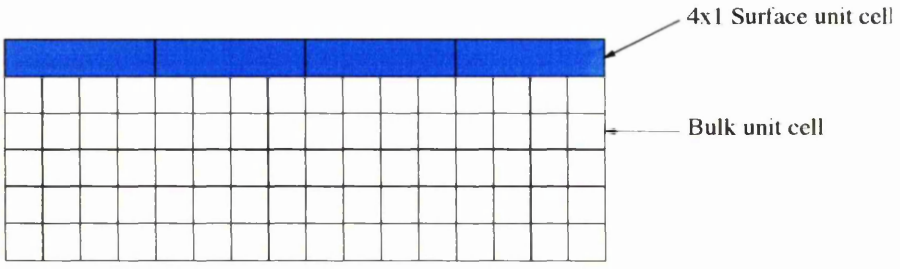


Figure 2.3: Schematic real space representation of a (4×1) surface structure. The unfilled squares represent bulk unit cells; the turquoise rectangles represents (4×1) surface unit cells. Reproduced by kind permission of C.J.Walker

the scattered intensity. At integer points scattering is dominated by the bulk structure. Equidistant between integer points — the anti-Bragg condition — bulk scattering is largely out of phase, and the intensity of scattering from the bulk is of the same order as from a single layer of atoms [6], thus this region is most sensitive to surface structure. Interference between surface and bulk terms is critically dependent on surface structure. The phase and amplitude of the bulk terms are well defined, thus CTRs can potentially be used to determine the atomic co-ordinates of atoms in the selvedge with high precision.

Generally the structure of the selvedge is different from that of the bulk. Formation of a surface leaves dangling bonds, and the surface may restructure to minimize its free energy. A larger surface unit cell may arise from adsorption of an overlayer or from a reconstruction of the selvedge. Larger unit cells give rise extra streaks of diffuse scattering perpendicular to the surface, in-between the CTRs — fractional order rods. This is illustrated in figures 2.3 and 2.4. Fractional order rods are of considerable use when investigating the structure of the selvedge as their intensity derives from the reconstructed portion of the selvedge only.

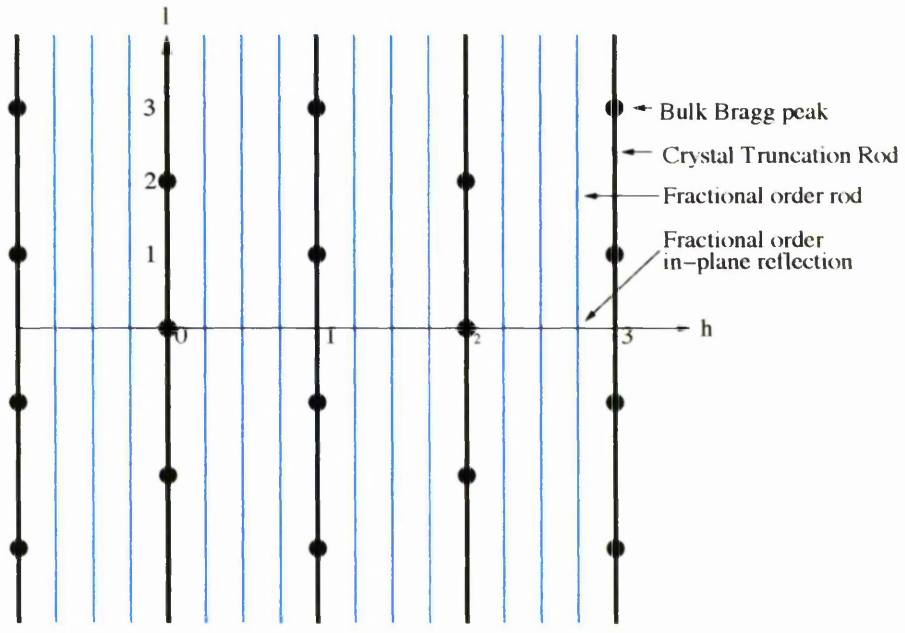


Figure 2.4: Reciprocal space view of (4×1) reconstruction. CTRs are shown in black, fractional (overlayer) rods are shown in turquoise. Reproduced by kind permission of C.J.Walker

Overlayer structures can be described with the Wood notation [9]. A $(n \times m)$ overlayer possess a unit cell with a periodicity of $m$ substrate unit cells in the $\mathbf{a_1}$ direction and $n$ unit cells in the $\mathbf{a_2}$ direction. If the unit cell of the surface contains an additional lattice point at the center of the unit cell, it may be described as centered, c$(n \times m)$. If diffraction from a surface is indexed with reference to a centered cell, alternate reflections will be systematic absent. The Park and Madden notation may express more complex reconstructions which cannot be described with Wood's notation. Here the unit cell of the reconstruction is written in terms of the product of a square matrix and the substrate unit cell vectors [10]:

$$\begin{pmatrix} \mathbf{a}_1^{\mathrm{rec}} \\ \mathbf{a}_2^{\mathrm{rec}} \end{pmatrix} = \begin{pmatrix} m_{11} & m_{12} \\ m_{21} & m_{22} \end{pmatrix} \begin{pmatrix} \mathbf{a_1} \\ \mathbf{a_1} \end{pmatrix} \tag{2.30}$$

In the particular case of centered overlayers, it may be possible to describe a smaller, primitive unit cell, containing only one lattice point by employing Park and Madden notation, see for example figure 7.4b on page 156.

The transverse width of CTRs, away from the bulk peaks, and the width of fractional order rods throughout their length, will be broadened by an amount inversely proportional to the size of the surface domains. A full analysis where surfaces of varying size are described by a correlation function [11] indicates that the peak shape will be Lorentzian with a full width at half maximum of:

$$\Delta \mathbf{Q}_{fwhm} = \frac{a_1}{\pi L} \tag{2.31}$$

where $L$ is the average domain size.

The surface may be composed of domains related by rotation or reflection, particularly in the case of a reconstructed surface, or surfaces covered by an ordered overlayer. If individual domains are large as compared with the coherence width of the X-ray beam, then intensities derived from the domains are averaged, otherwise the amplitudes of scattering from the different domains is averaged.

## 2.3 Experimental apparatus

### 2.3.1 Synchrotron radiation

Robinson has pointed out that intensity of X-rays scattered from a surface layer will typically be $\sim 10^5$ smaller than scattering from the bulk, necessitating a very intense source of X-rays [2]. Synchrotron sources provide very intense radiation

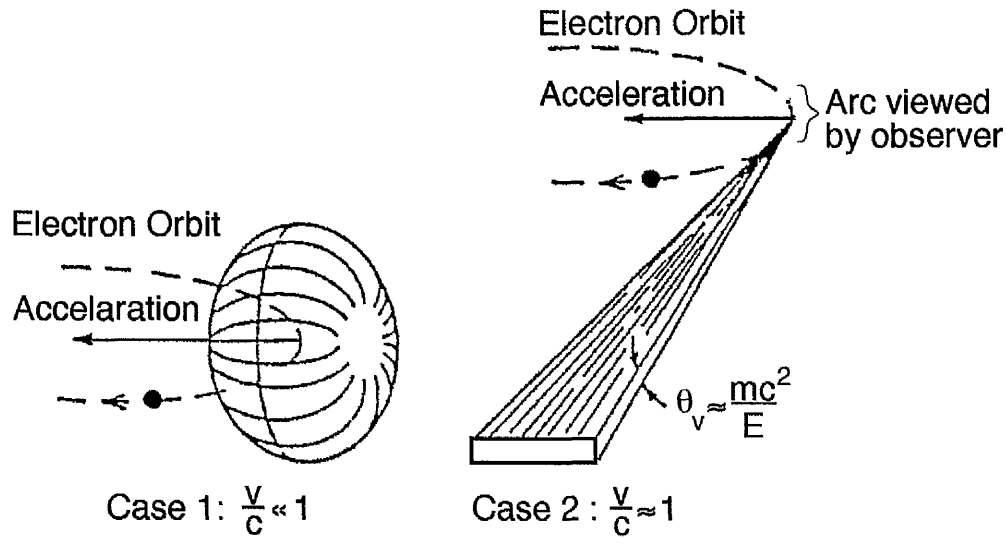


Figure 2.5: Spatial distribution of radiation emitted by electrons moving in a circular orbit. Case 1: classical. Case 2: relativistic. Reproduced from [14].

over a broad spectrum of wavelengths, from infrared to hard X-rays. With the addition of suitable monochromation, a continuously tunable source of X-rays can be created. Synchrotron radiation is typically highly collimated, with well defined polarization properties [12]. Synchrotron radiation is generated by the acceleration of electrons moving close to the speed of light [13]. Electrons moving in a circular orbit emit radiation with a toroidal spatial distribution, but when traveling near the speed of light relativistic effects distort the distribution observed in the laboratory frame, and radiation is emitted in the direction of the electrons velocity, see figure 2.5. A detailed description of synchrotron radiation is given in [5]. In a typical synchrotron radiation source, a beam of electrons moves in a quasi-circular orbit, constrained by a number of bending magnets, X-rays are emitted at the bending magnets, tangential to the electron orbit, and from insertion devices in straight sections between bending magnets.

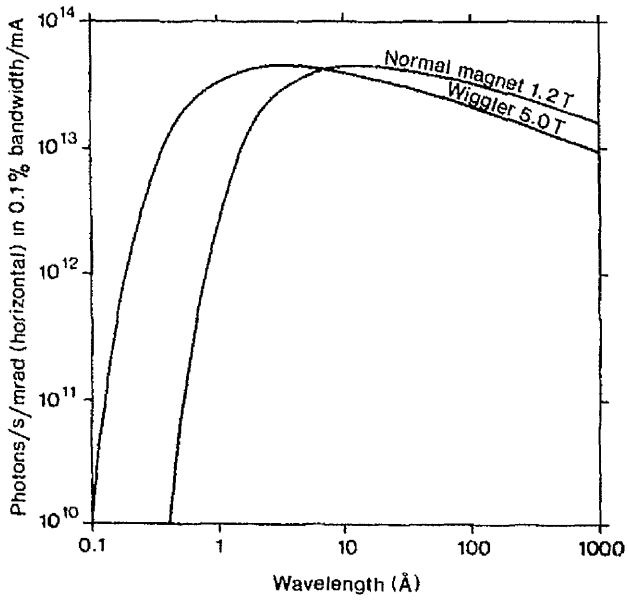


Figure 2.6: Comparison of synchrotron radiation emitted from a 1.2 T bending magnet and the 5 T wavelength shifter. Reproduced from [15].

The SRS, Daresbury, UK, is one of the earliest purpose built synchrotron radiation sources. In its ultimate configuration it operates with an electron energy of 2 GeV and a circulating current of 150–250 mA. The lifetime $\tau$, defined as the time for beam current to fall by a factor of e, is typically greater than 24 hours, and a new electron beam is typically injected once every 24 hours.

The source of X-rays used in the present work is a 5 T wavelength shifter [15] located in a straight section between two bending magnets. This consists of three superconducting magnets which induce a sharp kink in the electron path, shifting the peak output to shorter wavelengths, particularly increasing the intensity of X-rays with wavelength in the region of 1 Å. A comparison with a typical bending magnet source is shown in figure 2.6.

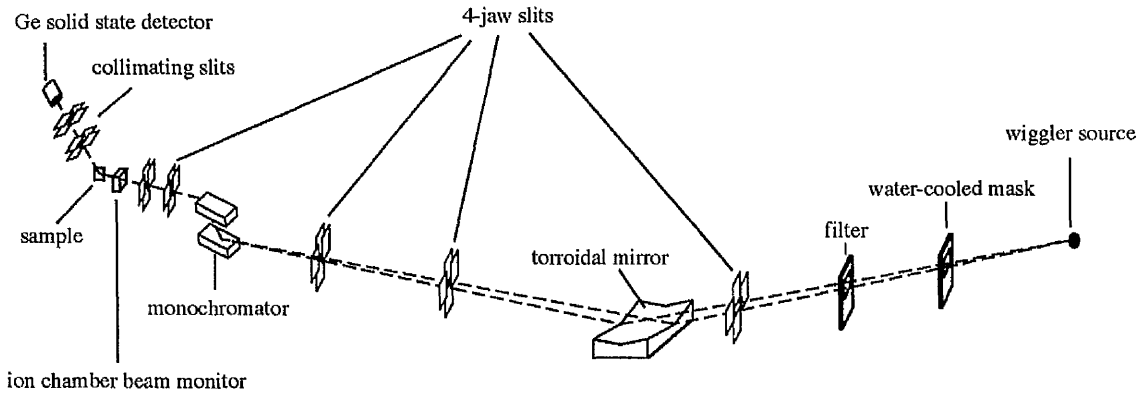


Figure 2.7: Schematic diagram of beamline 9.4 at the SRS, Daresbury. Reproduced from [14].

### 2.3.2 Beamline 9.4

The wavelength shifter source generates a 63 mrad fan of radiation, of which the central 4 mrad is used by beamline 9.4. A toroidal mirror 18.2 m from the source, inclined at 5.5 mrad from the horizontal, focuses X-rays on to the sample 38 m from the source. A water cooled, channel cut, Si(111) monochromating crystal located 36.6 m from the source allows continuous tuning of the X-ray wavelength between 0.7 Å and 1.8 Å, with a wavelength resolution $\frac{\delta\lambda}{\lambda} < 10^{-3}$. A rack of aluminium foil attenuators is provided to reduce the beam intensity for measurements near to bulk Bragg peaks. The beamline is terminated in a set of slits which define the dimensions of the beam that is projected onto the sample. An air-filled ionisation chamber is provided at the end of the beamline to measure the incident X-ray flux. The beamline is shown schematically in figure 2.7, and the reader is referred to [16] for a detailed description.

### 2.3.3 Diffractometer

The scattering geometry of a typical SXRD experiment is show in figure 2.8. Precise control of scattering angles is provided by a six-circle diffractometer, which is shown schematically in figure 2.9. The incident X-rays are polarised in the (horizontal) plane of the synchrotron, so a vertical scattering geometry (with the surface normal aligned horizontally) is employed. This has the advantage that scattered intensity does not fall to zero as the in-plane scattering angle $2\theta$ approaches 90°. The diffractometer consists of a conventional four-circle diffractometer mounted on a rotating table, with the detector mounted on an additional out-of-plane arm.

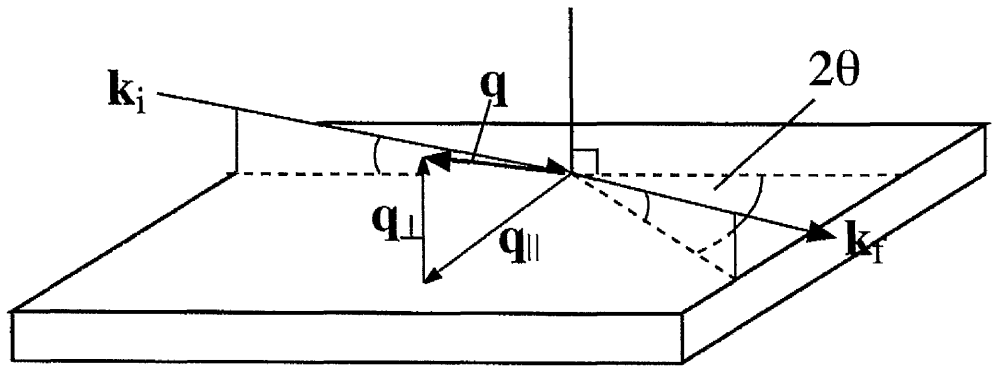


Figure 2.8: SXRD scattering geometry. The incident and scattered wave vectors $\mathbf{k_i}$ and $\mathbf{k_f}$ are shown, as is the in-plane scattering angle $2\theta$. Reproduced from [14].

The $\delta$ and $\omega$ circles of the four-circle diffractometer are concentric. The sample rotation $\phi$ is mounted on the $\chi$ circle which is in turn mounted on the $\omega$ circle. The $\chi$ circle is implemented as a pair of arcs with a range of $\pm 20°$. The fifth circle is provided by the rotating table $\alpha$, which rotates the other circles around

a vertical axis perpendicular to the common $\delta$, $\omega$ axis, and perpendicular to the incoming beam. The sixth circle, $\gamma$ is mounted on the $\delta$ arm and rotates around an axis perpendicular to the $\delta$, $\omega$ axis.

Three circles are necessary for alignment of the sample, two additional circles allow the angle of incidence ($\beta_{in}$) or exit angle ($\beta_{out}$) to be set whilst keeping the surface normal in a fixed alignment. In this work the surface normal was set horizontal, this minimises variation in both the illuminated area of the sample, and the detector resolution [17]. The availability of the $\gamma$ motion nearly doubles the out-of-plane momentum transfer, improving sensitivity to out-of-plane motions [18].

The diffractometer circles are driven by computer-controlled DC motors, whilst optical encoders provide position feedback. Movement along the additional out-of-plane arm is not motorised, the detector is moved manually between two fixed positions $\gamma = 0°$ and $\gamma = 15°$, fine motions being provided by the $\chi$ circle [18]. Whilst this arrangement considerably reduces mechanical complexity, the calculation of circle positions is more involuted and less intuitive than for true six-circle diffractometers where the detector may move continuously along the $\gamma$ circle. For example, in the case of the present apparatus the angles $\beta_{in}$ and $\beta_{out}$ are functions of three angles $\chi, \omega$ and $\alpha$ or $\gamma$ respectively, whereas for a true six-axis diffractometer $\beta_{in} = \alpha$ and $\beta_{out} = \gamma$, the $\chi$ and $\phi$ circles are used only for alignment of the surface normal and remain fixed during measurements [17].

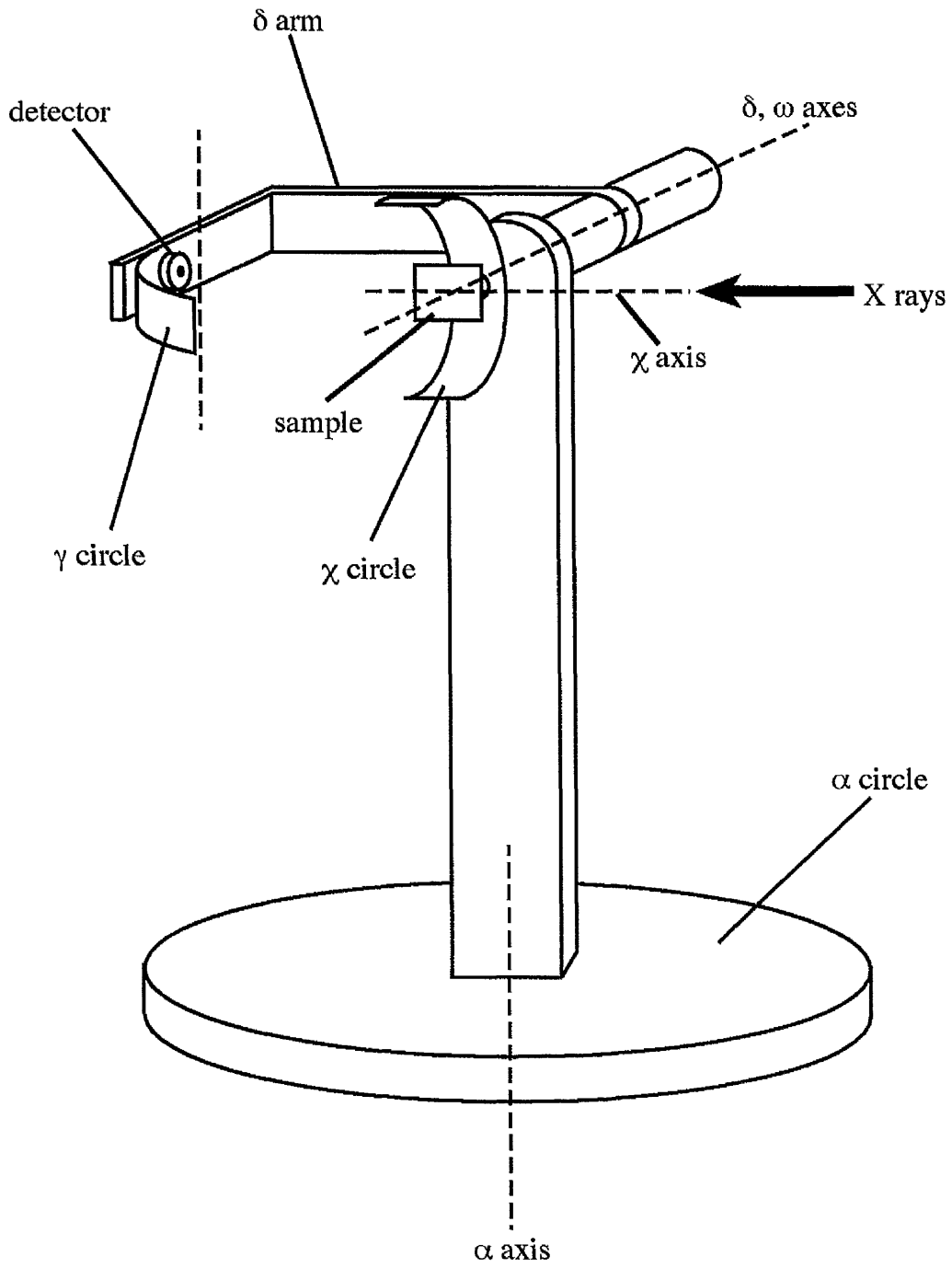


Figure 2.9: Schematic diagram of the 6-circle diffractometer used for the present work. Reproduced from [14].

### 2.3.4 X-ray detector

X-rays are detected with a single element, solid state detector consisting of a cryo-cooled, ultra-pure Germanium crystal. Incident X-rays generate a charge which is multiplied by a voltage applied across the crystal, the size of the resulting charge pulse is proportional to the incident energy. A discriminator circuit is used to collect only those peaks resulting from elastically scattered X-rays, and filter out fluorescence and higher harmonics of the monochromator.

Slits placed in front of the detector determine the detector resolution. In the in-plane direction they are opened fully, so the detector integrates over the full width of the selected diffraction feature in the $h$ and $k$ directions. The slit aperture in the out-of-plane direction determines $\Delta l$, the range of $l$ that is integrated [19].

### 2.3.5 Sample alignment

First the surface normal is aligned. A laser beam reflected by the sample is projected onto a screen and the $\chi$ and $\phi$ circles are adjusted until the precession of the projected spot, when $\omega$ is rotated by 180°, is minimised.

Crystallographic alignment is undertaken by locating two or more bulk Bragg peaks and adjusting the diffractometer circles to optimise their intensity. The optimised positions are used to calculate an alignment matrix, which with the optimised values of $\chi$ and $\phi$ obtained from the optical alignment and a matrix describing the diffractometer, contain all the information required to calculate the

diffractometer position corresponding to a given $h, k, l$, for a specified $\beta_{in}$ or $\beta_{out}$. The calculation of diffractometer positions is described in detail by Vlieg [17], and is implemented by in-house software.

### 2.3.6 Data collection

In principle is possible to simply measure the intensity of the diffracted peaks. In practice this value is affected by the degree of ordering of the sample, and beam collimation, so measuring integrated intensity gives a more accurate result [1]. Ideally intensity is collected by scanning at right angles across the rods. In practice rotating the sample around its normal ($\phi$) is adequate. As rods are continuous in the out-of-plane direction, such a scan will collect a finite segment of the rod determined by the detector slits.

To account for variation in X-ray flux as the circulating beam current decays, the measurement of a point on the $\phi$ scan is specified to continue for the time taken to record a specified number of counts with the ionisation chamber located at the end of the beamline.

Reflections with maximum momentum transfer will be most sensitive to surface structure; hence care is taken to extend the data collection to maximum possible in-plane and out-of-plane momentum transfer. This will largely be a function of the selected X-ray wavelength, but the width of the beryllium window also puts an upper limit on the out-of-plane momentum transfer. Data collected with small $\beta_{in}$ or $\beta_{out}$ will be largely insensitive to out-of-plane motions. Hereafter

this is termed an in-plane data set. In principle a rod collected in the specular geometry $\beta_{in} = \beta_{out}$ will be sensitive to out-of-plane motions only; however as this represents a simple reflection from the surface, regions with no lateral ordering will also contribute.

### 2.3.7 INGRID

The present work employed the INGRID (INstrument for GRazing Incidence Diffraction) UHV chamber for sample preparation and measurement. This chamber is largely based on a previous system described in the literature [20, 21]. A photograph of the chamber in use at station 9.4 is shown in figure 2.10.

X-rays may pass in and out of the chamber via a beryllium window 75 mm wide and occupying 220° of the chamber circumference. The sample manipulator, which is bolted onto the $\phi$ circle of the diffractometer, is connected to the main chamber by a large bellows, which allows for motion of the $\chi$ circle, and a two-stage differentially pumped rotary seal that allows the sample to be rotated independently of the chamber.

Samples are fixed to a molybdenum backplate with tantalum straps. This method requires steps to be machined into the sample so the straps do not protrude above the sample surface. A tungsten filament behind the backplate allows for resistive heating and heating by electron bombardment. Temperature can be measured by a chromel-alumel (K-type) thermocouple held under a tantalum strap, or with an optical pyrometer.

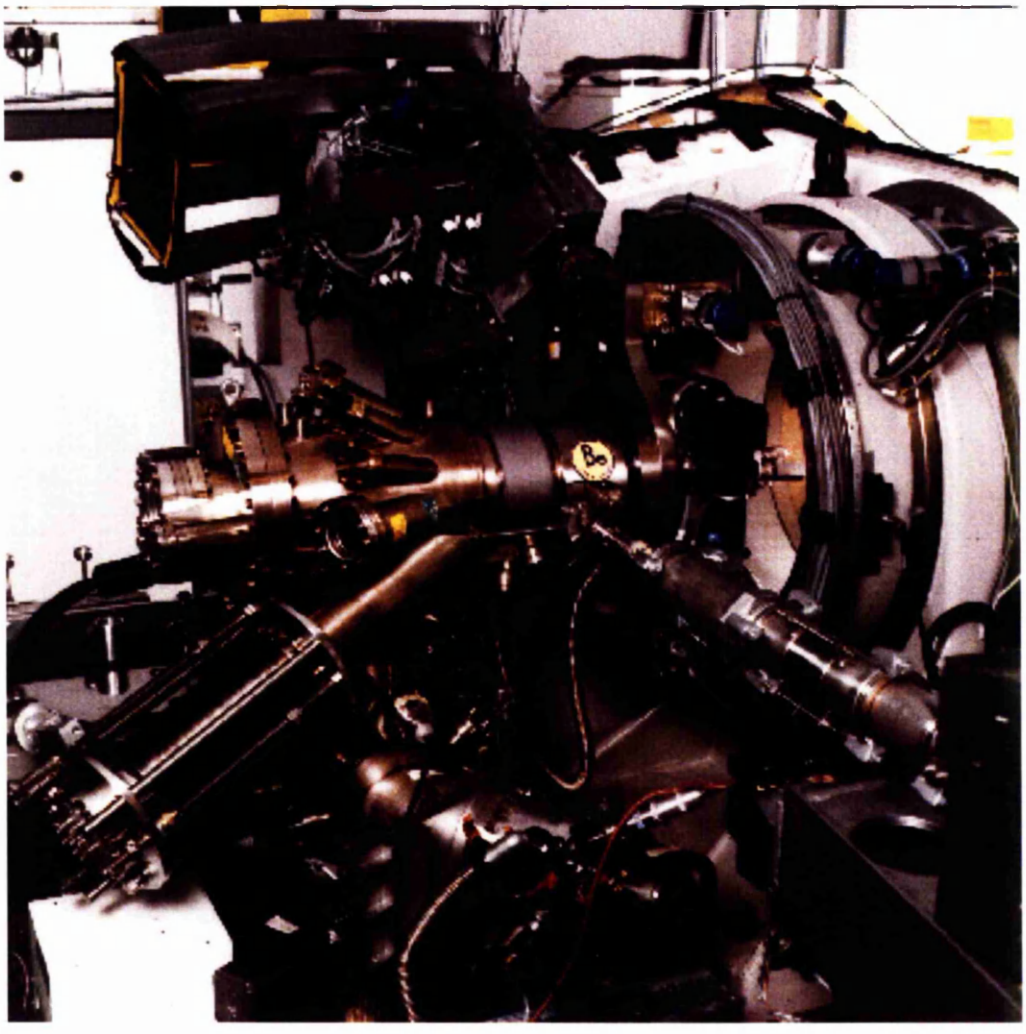

Figure 2.10: The INGRID vacuum chamber in use at station 9.4. The diffractometer is located at the right of the picture, the out-of-plane arm and detector can be seen at the top of the picture. The beamline protrudes from the lower right of the picture. The INGRID chamber can be seen at the center of the picture; the long, upward facing bellows on the left houses the CMA, and the light grey area is the beryllium window. Reproduced by kind permission of STFC.

Radial ports facing the sample accommodate an ion gun for sample preparation, LEED apparatus, a combined cylindrical mirror analyser and electron gun for Auger electron spectroscopy (AES) and a residual gas analyser. A fast entry lock, to allow the interchange of samples without breaking vacuum is provided but was out of commission during the present work. The chamber is pumped by a turbo-molecular pump, ion pump and titanium sublimation pump. Gate valves allow the isolation the the turbo-molecular and ion pumps. Gases may be introduced via three precision leak valves. After baking to approximately 250 °C for 12–24 hours, base pressures in the region of $10^{-11}$ mbar are routinely achieved.

## 2.4 Data analysis

Data analysis employed the ANA-AVE-ROD suite of software written by Elias Vlieg [22]. In the first stage structure factors are calculated by integrating and applying correction factors. Equivalent reflections are then averaged to give the final data set. Analysis of the data proceeds by comparison of the data with calculated structure factors for possible models, and optimisation of geometric and other parameters of the surface model.

### 2.4.1 Data integration and correction

Data may be integrated numerically, with the background estimated from points at the edges of the scan. Integration may also be undertaken by fitting a functional form and background to the data. The preferred method is to integrate scans numerically, but use a fit to the peak to give a value for the background. This is a more robust method, not requiring an exact fit to the shape of the peak, and provides a good estimate of the background even for relatively noisy scans.

Once the data has been integrated it is necessary to apply a number or resolution and geometric correction factors to convert the data into structure factors:

$$F_{hkl} = \sqrt{\frac{I_{int}}{C_{tot}}} \tag{2.32}$$

where:

$$C_{tot} = PLC_{rod}C_{area} \tag{2.33}$$

Here $P$ is the polarisation factor, $L$ is the Lorentz factor, $C_{rod}$ the rod interception correction and $C_{area}$ corrects for the active sample area and beam profile. They are discussed briefly in the following sections. The derivation of correction factors is described in detail by Vlieg [19].

#### Polarization factor

The polarisation factor was introduced in section 2.2.1. The incident X-rays are assumed to be completely polarised in the plane of the synchrotron, hence as the detector moves out of the vertical plane parallel to the incident X-rays, the

observed intensity will fall off sinusoidally:

$$P = \cos^2 \psi \tag{2.34}$$

where $\psi$ is the angle between incoming and scattered beams in the horizontal plane. This is independent of sample orientation and can conveniently be expressed in terms of $\alpha$, $\delta$, and $\gamma$.

$$P = 1 - (\sin\alpha \cos\delta \cos\gamma + \cos\alpha \sin\gamma)^2 \tag{2.35}$$

It can be seen that for observation of in-plane data, when $\gamma \sim 0$ and $\alpha \sim 0$, $P \sim 1$.

### Lorentz factor

This corrects for variation in intensity arising from the Ewald sphere cutting the rod at different angles. A shallow angle will lead to a broader peak and larger integrated intensity than if the Ewald sphere intersects the rod near normal. For rocking scans and the present diffractometer geometry the Lorentz factor is given as:

$$L = \frac{1}{\sin\delta \cos\beta_{in} \cos\gamma} \tag{2.36}$$

### Rod interception

The diffraction features of interest are sharp in the $h$ and $k$ directions, but continuous in the $l$ direction. Thus each scan integrates the rod over a range $\Delta l$ which is a function of the out-of-plane detector slit width, and varies with the

angle between the rod and the detector opening. In the present geometry a rather complicated correction factor is required to account for this effect:

$$C_{rod} = \frac{2\cos\beta_{in}\cos\gamma}{cos\alpha + cos(\alpha - 2\beta_{in}) + \sin(2\alpha - 2\beta_{in}) + 2\sin^2(\alpha - \beta_{in})\cos\delta\cos\gamma} \tag{2.37}$$

### Area and beam correction factors

Under normal experimental conditions the beam illuminates a stripe across the sample. The width of the beam is defined by the vertical separation of the end of beam slits. The active area of the sample is the parallelogram defined by the coincidence of the illuminated stripe and the projection of the out-of-plane detector slits, this is illustrated in figure 2.11. A simple analytical form for the active area can be derived, but this breaks down at small $\delta$ when the parallelogram extends beyond the sample. Variation in the active area and the beam profile are accounted for by a simple numerical ray tracing routine in the ANA software [19]. The sample surface is broken up into grid of squares and the incident flux calculated for each square that is on the sample and visible to the detector. Summation over the sample allows the calculation of correction factor $C_{area}$.

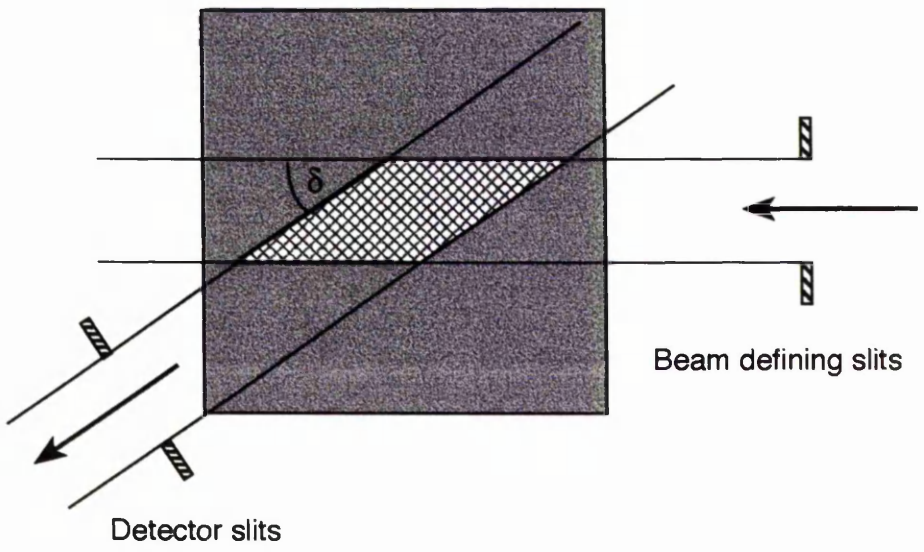


Figure 2.11: Active area correction — the active area is a parallelogram (hatched), defined by end of beam and detector slits.

### 2.4.2 Averaging

Whenever possible one or more symmetry equivalent reflections are recorded. This helps to identify anomalous data points, and allows the estimation of systematic errors in the data arising from small misalignments, sampling of different areas of the surface etc. The AVE program calculates the weighted average of symmetry equivalent structure factors, and calculates final errors in the structure factors using a method described in detail by Walker [23].

For a set of $E$ symmetry equivalent reflections AVE calculates; the variance in the set of structure factors ($\sigma_1$), the standard deviation of the statistical average

of the structure factors ($\sigma_2$), and the agreement factor:

$$\varepsilon_{h,k,l} = \frac{\sigma_1}{\bar{F}_{h,k,l}} \tag{2.38}$$

Points of insufficient quality are excluded from calculations of the agreement factor, usually by discarding points where $F_{h,k,l} < 2\sigma_2$. The average agreement factor over the whole data set, which is a measure of the systematic error, is given by:

$$\bar{\varepsilon} = \frac{1}{M} \sum_{data\ set} \varepsilon_{h,k,l} \tag{2.39}$$

where M is the number of non-equivalent reflections. This normally takes values in the region of 10% and is a useful indicator of the consistency of the data set. The final error in a given structure factor is then given by:

$$\sigma^{expt} = \sqrt{\bar{\varepsilon}^2 \bar{F}^2 + \sigma_2^2} \tag{2.40}$$

where $\bar{F}^2$ is the weighted average of the square of the measured structure factors. This approach has the advantage that a realistic estimate of errors can be given even for sections of the data where no equivalent reflections are available. The systematic error usually dominates the data set, but large errors in individual values of $F_{h,k,l}$ are also reflected in the final error.

### 2.4.3 Structure determination

Whilst the structure factor is a Fourier transform of the spatial distribution of electron density, it is not possible to simply determine the surface structure by calculating the inverse Fourier transform. Experimentally only intensity and

not amplitude may be recorded, thus no phase information can be collected. Determination of surface structure proceeds by comparing the experimental data with calculated structure factors, and seeking models that give a good fit to the data.

The reduced $\chi^2$ agreement factor ($\chi^2_\nu$) is used to evaluate the quality of fit of a given model to the experimental data:

$$\chi^2_\nu = \frac{1}{N-p} \sum_{hkl} \left( \frac{|F^{calc}_{hkl}| - |F^{expt}_{hkl}|}{\sigma_{F^{expt}_{hkl}}} \right)^2 \tag{2.41}$$

where $N$ is the number of data points, $p$ the number of free parameters in the model and $\sigma_{F^{expt}_{hkl}}$ the experimental error of $F^{expt}_{hkl}$ [24]. In the absence of a normal distribution of $\sigma_{F^{expt}_{hkl}}$, $\chi^2$ no longer conforms to a well defined probability distribution and is used simply as a convenient measure of quality of fit. This has the unfortunate side effect that it is not possible to calculate a threshold value of $\chi^2_\nu$ that indicates adequate quality of fit, and there is no rigorous criteria that can be brought to bear to judge the significance of improvements in $\chi^2_\nu$ [25]. However $\chi^2_\nu \sim 1$ is generally taken to be an empirically validated indication of adequate quality of fit [1]. Robinson has pointed out that $\chi^2$ alone can never show a model is correct, but can only be used to discard incorrect models [3].

Calculation of theoretical structure factor amplitudes is undertaken with the ROD programme [22]. In addition to geometric parameters other surface properties can be included in the model; atom occupancies, thermal vibrations, domains described by rotations and reflections, surface roughness etc. Parameters may be optimised by the least squares method employing the Levenberg-Marquard algorithm [26], or by simulated annealing [25]. As it is impossible to be certain

that a given $\chi^2_\nu$ constitutes the global minimum of the $\chi^2_\nu$ hypersurface, great care must be taken to ensure adequate searching of the parameter space. The following strategies have been found to have some value in revealing otherwise overlooked minima.

- Using different initial values for geometric parameters; starting from clean and bulk terminated surfaces, starting parameters at a range of plausible values, starting parameters at extreme values.
- Careful application of limits to parameters to force optimisations into particular regions or to prevent the appearance of unphysical parameters.
- Trialing models with different allowed motions; e.g. first constraining all atoms in a layer to have the same motions before allowing individual motions.
- Optimising parameters in different orders; all parameters optimised simultaneously, heaviest atoms optimised first, atoms nearest the surface optimised first etc.
- Use of simulated annealing; as implemented this rarely reaches a convincing global minimum but is useful for discovering unexpected areas of moderately good fit.

The practice of cyclically optimising individual parameters one at a time was generally avoided as it is expected to increase the likelihood of the optimisation becoming stuck in a local minima.

The uncertainties in the structural parameters are calculated by varying the parameter, while the others are kept fixed, until $\chi^2_\nu$ has increased by $1/(N-p)$ from its minimum value [3].

# References


[1] R. Feidenhans'l. *Surf. Sci. Rep.*, 10:105–188, 1989.

[2] I.K. Robinson and D.J. Tweet. *Rep. Prog. Phys.*, 55:599–651, 1992.

[3] I.K. Robinson. *Surface Crystallography*, volume 6 of *Handbook on Synchrotron Radiation*. North-Holland, 1986.

[4] E. Vlieg and I.K. Robinson. Two-dimensional crystallography. In P. Coppens, editor, *Synchrotron Radiation Crystallography*. Academic Press, 1992.

[5] J. Als-Nielsen and D. McMorrow. *Elements of Modern X-ray Physics*. Wiley, 2001.

[6] P.B. Howes. *The formation of gold-semiconductor interfaces determined by SXRD*. PhD thesis, University of Leicester, 1993.

[7] J.M. Cowley. *Diffraction physics*. North-Holland, 1975.

[8] A.J.C. Wilson and E. Prince, editors. *International tables for crystallography*. IUCR, 2nd edition, 1999.

[9] E.A. Wood. *J. Appl. Phys.*, 35:1306, 1964.

[10] R.L. Park and H.H. Madden. *Surf. Sci.*, 11:188, 1968.

[11] E. Vlieg, J.F. Van der Veen, S.J. Gurman, C. Norris, and J.E. Macdonald. *Surf. Sci.*, 210:301–321, 1989.

[12] P. Coppens. *Synchrotron Radiation Crystallography.* Academic Press, 1992.

[13] F.R. Elder, A.M. Gurewitsch, R.V. Langmuir, and H.C. Pollock. *Phys. Rev.*, 71:829–830, 1947.

[14] G.M. Charlton. *Atomic structure of transition metal oxide surfaces and interfaces.* PhD thesis, University of Manchester, 1997.

[15] N. Marks, G.N. Greaves, M.W. Poole, V.P. Suller, and R.P. Walker. *Nucl. Inst. Method.*, 208:97–103, 1983.

[16] C. Norris, M.S. Finney, G.F. Clark, G.Baker, P.R. Moore, and R. van Silfhout. *Rev. Sci. Instrum.*, 63:1083–1086, 1992.

[17] M. Lohmeier and E. Vlieg. *J. Appl. Crystallogr.*, 26:706–716, 1993.

[18] J.S.G. Taylor, C. Norris, E. Vlieg, M. Lohmeier, and T.S. Turner. *Rev. Sci. Instrum.*, 67:2658–2659, 1996.

[19] E. Vlieg. *J. Appl. Crystallogr.*, 30:532–543, 1997.

[20] J.S.G. Taylor and C. Norris. *Rev. Sci. Instrum.*, 68:3256–3257, 1997.

[21] C.L. Nicklin, J.S.G. Taylor, N. Jones, P. Steadman, and C. Norris. *J. Synchrotron Rad.*, 5:890–892, 1998.

[22] E. Vlieg. *J. Appl. Crystallogr.*, 33:401–405, 2000.

[23] C.J. Walker. *X-ray diffraction of some technologically important surfaces.* PhD thesis, University of Leicester, 2003.

[24] P.B. Bevington and D.K. Robinson. *Data Reduction and Error Analysis for the Physical Sciences.* McGraw-Hill, 3rd edition, 2003.

[25] W.H. Press, S.A. Teukolsky, W.T. Vetterling, and B.P. Flannery. *Numerical Recipes in C.* Cambridge University Press, 2nd edition, 1992.

[26] D.W. Marquardt. *J. Soc. Ind. App. Math.*, 11:431–441, 1963.

# Chapter 3

# Scanning tunneling microscopy

## 3.1 Introduction

Since the construction of the first scanning tunneling microscope (STM) in the early 1980s, the use of STM has proliferated to a remarkable extent. STMs are available commercially from a number of manufacturers, and imaging of individual atoms is undertaken routinely. STM has been applied in remarkably diverse areas, not only to the highly ordered single crystal surfaces of traditional surface science, but to liquid films, polymer surfaces and biological systems. STM has been used to manipulate individual surface atoms to striking effect.

The generation of real space images down to the atomic scale, which may be understood in a highly intuitive fashion, is perhaps the greatest attraction of STM. Such images can be highly illuminating, and are very useful in generating candidate models for trial and error methods (such as SXRD), particularly for

complex structures. STM is a highly local probe, requiring no long range ordering, and thus is very useful in the study of disordered surfaces and aperiodic structures such as quasi-crystals, defects, domain boundaries etc. Whilst STM is frequently undertaken in UHV, it is also able to image in liquids, and operate at ambient and higher pressures. The ability to rapidly re-image an area of surface allows the study of dynamic processes.

Set against the considerable advantages of the technique are a number of limitations. Whilst simple interpretation is possible, truly unambiguous interpretation of STM images requires detailed simulation of the tunneling processes. STM lacks elemental specificity, and at best spatial resolution does not approach that of diffraction techniques. The fabrication of atomically sharp tips remains a black art, and the highest resolution images are frequently only achieved after long periods of trial and error.

STM revolves around the phenomena of quantum tunneling. An atomically sharp metal tip is located a few angstroms above a surface, and a bias voltage applied across the gap. A small current is generated by quantum mechanical tunneling of electrons across the insulating gap between the tip and the surface. This current strongly depends on the width of the gap, giving rise to sensitivity to surface topography. The electronic structure of the surface also has a large impact on the tunneling current as is discussed in later sections of this chapter.

In section 3.2 rather than review state of the art modeling of STM, a number of idealised models of tip-surface tunneling which illuminate the practice of STM are

described. In section 3.3 the experimental apparatus used for the STM studies in chapter 7 are described. Figures in this chapter are reproduced from [1–3].

## 3.2 Theoretical considerations

### 3.2.1 Tunneling across a one dimensional barrier

In its simplest form the vacuum gap between tip and surface can be modeled as a one dimensional energy barrier [4]. Classically a particle with energy $E_0$ which is less than the barrier height $V_0$ cannot cross the barrier, as shown schematically in figure 3.1a. In a quantum mechanical treatment the particle exists as a continuous wave function whose amplitude describes the probability of the particle being located at a given point. For a particle with energy less than the barrier height, there is now a small probability that the particle may tunnel through the barrier. The particle is described by wave functions on either side of the barrier, and a decaying exponential within the barrier, as is shown in figure 3.1b.

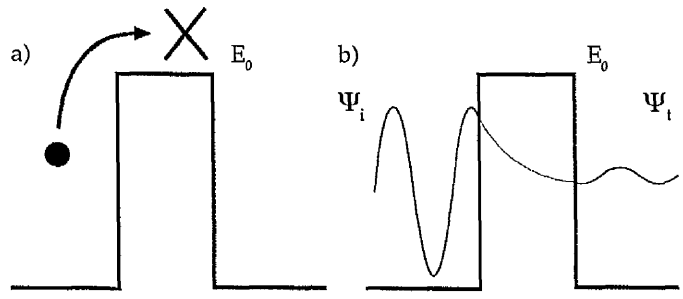


Figure 3.1: A schematic of a one-dimensional barrier. a) The classical description. b) Quantum tunnelling, $\Psi_i$ and $\Psi_t$ represent the incident and transmitted wave functions respectively.

At low $V_0$, and low temperature the tunneling current across the barrier is given by [5]:

$$I \propto \frac{V_0}{d} e^{(-2\kappa d)} \tag{3.1}$$

where $V_0$ is the bias voltage, $d$ is the width of the barrier (tip-surface distance) and $\kappa$ is the decay constant for the wave within the barrier given by:

$$\kappa = \sqrt{\frac{2m\Phi}{\hbar^2}} \tag{3.2}$$

Here $m$ is the mass of the electron and $\Phi$ is the average work function of the tip and surface. It can be seen that the tunneling current depends exponentially on the tip-sample distance $d$. For typical values of the work function (in the range of a few eV) changes of $d$ in the region of 1 Å give rise to an order of magnitude variation in tunneling current. This is the origin of STM's atomic scale sensitivity to surface topography [4].

### 3.2.2 Tersoff and Hamann

A more sophisticated approach to determining the tunneling current is to consider the overlap of the tip wave function $\Psi_\mu$ and the sample wave function $\Psi_\nu$. This has been undertaken by Tersoff and Hamann [6, 7] with highly idealised models of the tip. Using this approach, tunneling current is given by an expression due to Bardeen; for first order perturbation at low $V_0$, and low temperature, the tunneling current across the barrier is given as [8]:

$$I \propto V_0 \sum_{\mu,\nu} |M_{\mu\nu}|^2 \delta(E_\nu - E_f) \cdot \delta(E_\mu - E_f) \tag{3.3}$$

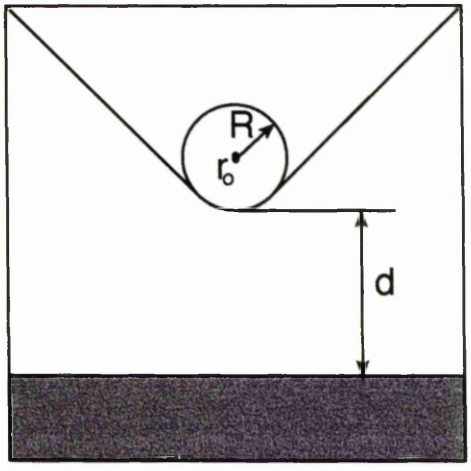


Figure 3.2: Schematic of Tersoff and Hamann's model of the tip as a spherical potential well [6, 7]. R represents the radius of the well located at a position $\mathbf{r_0}$, a height $d$ above the surface.

where $V_0$ is the bias voltage, $E_f$ is the Fermi energy, and $E_{\mu,\nu}$ are eigen-energies of the states $\Psi_\mu$, and $\Psi_\nu$ in the absence of tunneling. The delta functions enforce elastic tunneling, and $M_{\mu\nu}$ represents the tunneling matrix between the states:

$$M_{\mu\nu} = \frac{-\hbar^2}{2m} \int \left(\psi_\mu^* \nabla \psi_\nu - \psi_\nu \nabla \psi_\mu^*\right) \cdot d\mathbf{S} \tag{3.4}$$

which is expressed as an integral of wave functions over a notional surface between tip and sample. Tersoff and Hamann first evaluate the tunneling matrix by representing the tip as a point charge at a position $\mathbf{r_0}$ in which case the tunneling matrix simply evaluates to the amplitude of the surface wave function $\Psi_\nu$ at $\mathbf{r_0}$, hence equation 3.3 becomes:

$$I \propto V \sum_\nu |\psi_\nu(\mathbf{r_0})|^2 \delta(E_\nu - E_f) \tag{3.5}$$

Thus the tunneling current is proportional to the Fermi level local density of states (LDOS) of the surface, at the tip position. A more sophisticated model [7] considers the tip as a spherical potential well of radius R, as shown in figure 3.2.

Thus the tip electrons are described by spherically symmetric, asymptotic wave functions — hereafter $s$-waves. In this case the tunneling current is given by:

$$I \propto V\rho_s(\mathbf{r_o}; E_f)\rho_t(E_f) \tag{3.6}$$

where $\rho_s(\mathbf{r_o}; E_f)$ represents the Fermi energy, surface density of states at $\mathbf{r_o}$ (the center of the tip) and $\rho_t(E_f)$ represents the Fermi energy density of states of the tip. So with this more realistic tip model, it can again be seen that the STM signal depends on the LDOS.

It can also be seen that the current is a function of bias voltage. By controlling the voltage, occupied and unoccupied states can be imaged, as shown in figure 3.3. The transmission probability for tunnelling is greatest for the electrons closest to the Fermi level of the negative electrode [9] as indicated by the lengths of the arrows.

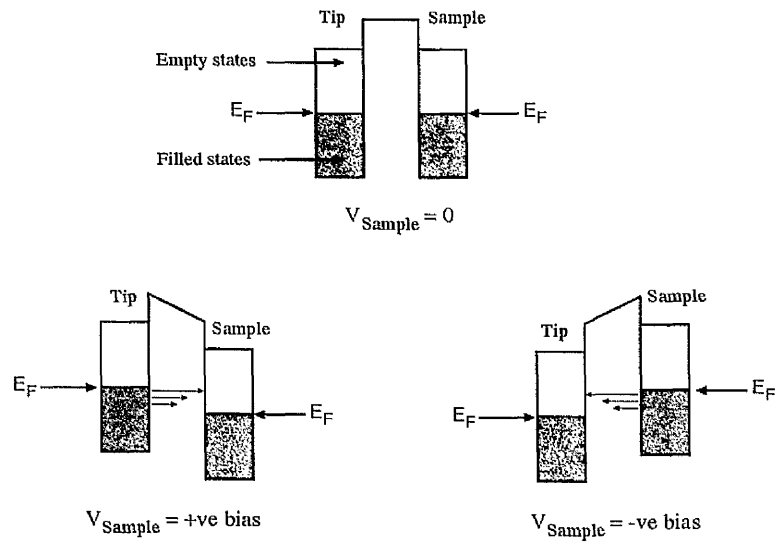


Figure 3.3: Bias dependant tunnelling between tip and sample states.

### 3.2.3 Lang

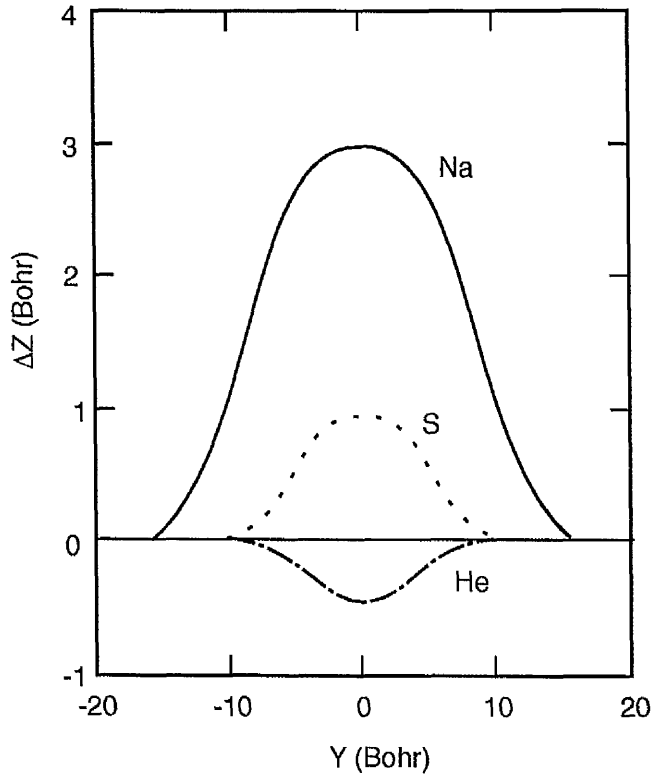


Figure 3.4: Change in tip distance ($\Delta Z$) versus lateral separation (Y) of the adsorbates for small voltages (1 Bohr = 0.529 Å) [10, 11].

The models presented above take no account of the composition of tip or surface. Lang has extended the wave function approach described in the previous section to consider the imaging of different atomic species [10, 11].

Tip and surface are modeled as flat jellium electrodes — an electron sea on a uniform positive background charge. A single atom is adsorbed on each electrode; an electrode with an adsorbed sodium atom is taken to be the tip and an electrode with a single adsorbed sodium, sulphur or helium represents a surface. For a small bias voltage, the tip height giving rise to a constant tunneling current is calculated as the tip is scanned over the three different surfaces, see figure 3.4.

It can be seen that STM will record a much larger height when scanning over a sodium atom as compared to a sulphur atom. In addition to the larger radius of the sodium atom, this reflects a higher density of states at $E_f$ for sodium than sulphur. For the case of a helium atom, a negative tip displacement is observed; helium is imaged as a depression despite the atom sitting above the jellium surface. This arises from the low energy of the closed valence shell of the helium atom, which polarises substrate states away from the Fermi energy, reducing the density of states at the Fermi level.

### 3.2.4 Chen

The approaches described in the previous two sections rely on modeling the tip electrons with spherically symmetric $s$-wave functions, and predict lateral resolution limits of between 6 Å [6, 7] and 9 Å [10] inconsistent with studies apparently resolving atoms at a spacing of $\sim$ 3 Å. Chen [12] points out that the $s$-wave approximation is unlikely to be valid for common tip materials (W,Pt,Ir) whose Fermi level DOS are largely composed of $d$ states, tungsten in particular is known to form highly localized $d_{z^2}$ dangling bonds.

Chen approaches this issue by considering a surface of highly localised metallic $d_{z^2}$ dangling bonds [12]. An $s$-wave tip scanned across a metal surface follows a contour of LDOS which in the case of this surface is highly corrugated, see figure 3.5. It is then argued by reciprocity that scanning a tip described by $s$-waves over a surface consisting of $d_{z^2}$ dangling bonds is identical to scanning a $d_{z^2}$ tip

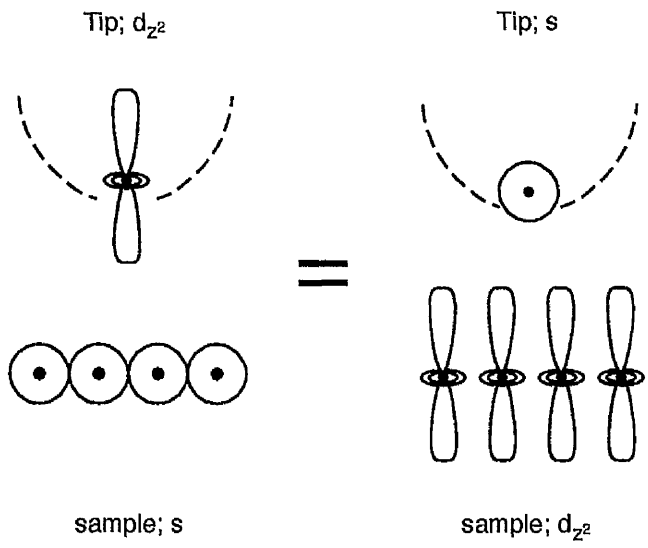


Figure 3.5: Schematic diagram illustrating Chen's reciprocity argument [12].

over a surface described by $s$-wave functions, as shown schematically in figure 3.5. Hence the presence of $d_{z^2}$ states on the tip considerably enhances the apparent corrugation of the surface. A more detailed treatment determines that in the presence of $p_z$ and $d_{z^2}$ dangling bonds states on the tip, a contour determined by the derivatives of the surface wave functions of the sample is followed. This contour will exhibit a far stronger corrugation than that of the LDOS, thus it is possible for individual atoms to be resolved.

### 3.2.5 STM of metal oxide surfaces

In semiconductors including some transition metal oxides such as $TiO_2$, the Fermi level lies in the band gap, hence tunneling occurs between the tip and high-lying valence states or low-lying conduction states.

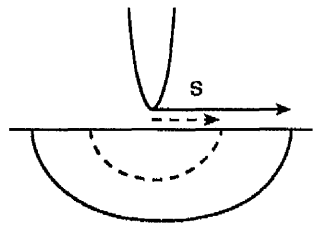


Figure 3.6: Schematic diagram of the space charge region in the vicinity of an STM tip.

The low conductivity of many transition metal oxides imposes a fundamental limit on spatial resolution due to space charge effects [13]. In the models described above, the voltage across the vacuum gap is taken to be identical to the sample-tip bias voltage. In low conductivity metal oxide surfaces some of the applied voltage is dropped across the space charge region directly below the tip as shown schematically in figure 3.6. This has the effect of smearing out the electronic structure of the surface, limiting the spatial resolution to some fraction of the size of the space charge region $S$. A simple expression for $S$ at zero bias is:

$$S = \sqrt{\frac{2\epsilon kT}{q^2 N}} \tag{3.7}$$

where $q$ is the charge of an electron, $\epsilon$ is the sample's permittivity, $N$ is the density of charge carriers, $k$ is the Boltzmann constant and $T$ is the temperature. Thus it can be seen that as the local charge carrier concentration increases, the space charge region diminishes. For Si(111)-(7×7), $S$ has been calculated to be 2 Å, whereas for ZnO predicted space charges range between 2 and 200 Å. Bonnel argues that atomic resolution imaging of oxides with such small space charge diameters should be possible, regardless of band gaps exceeding 3 eV [13].

## 3.3 Experimental apparatus

STM measurements in chapter 7 were undertaken using an Omicron UHV low temperature STM and Omicron UHV room temperature combined STM/AFM. Whilst the AFM/STM operates at room temperature, the low temperature microscope stage is contained in a bath cryostat that can operate at temperatures as low as 5 K, however all the present work was undertaken at room temperature. In the next section the vacuum systems containing the two microscopes are considered, and in the subsequent sections relevant experimental aspects of STM common to both apparatus are considered.

### 3.3.1 Vacuum systems

A schematic of the low temperature STM vacuum system is shown in figure 3.7 and the AFM/STM vacuum system is shown in figure 3.8. The vacuum systems consist of load-locks for the introduction of samples without breaking vacuum, preparation and analysis chambers, and STM chambers containing the STM stages. The preparation and analysis chambers are equipped with ion guns for cleaning samples by ion bombardment, residual gas analysers, and low energy electron diffraction (LEED) apparatus. Precision leak valves allow the introduction of gases from an inlet manifold. The low temperature STM is equipped with an electron gun, X-ray gun and hemispherical electron energy analyser for X-ray photoelectron spectroscopy (XPS) and Auger electron spectroscopy (AES) measurements. The STM/AFM is equipped with a LEED apparatus which can

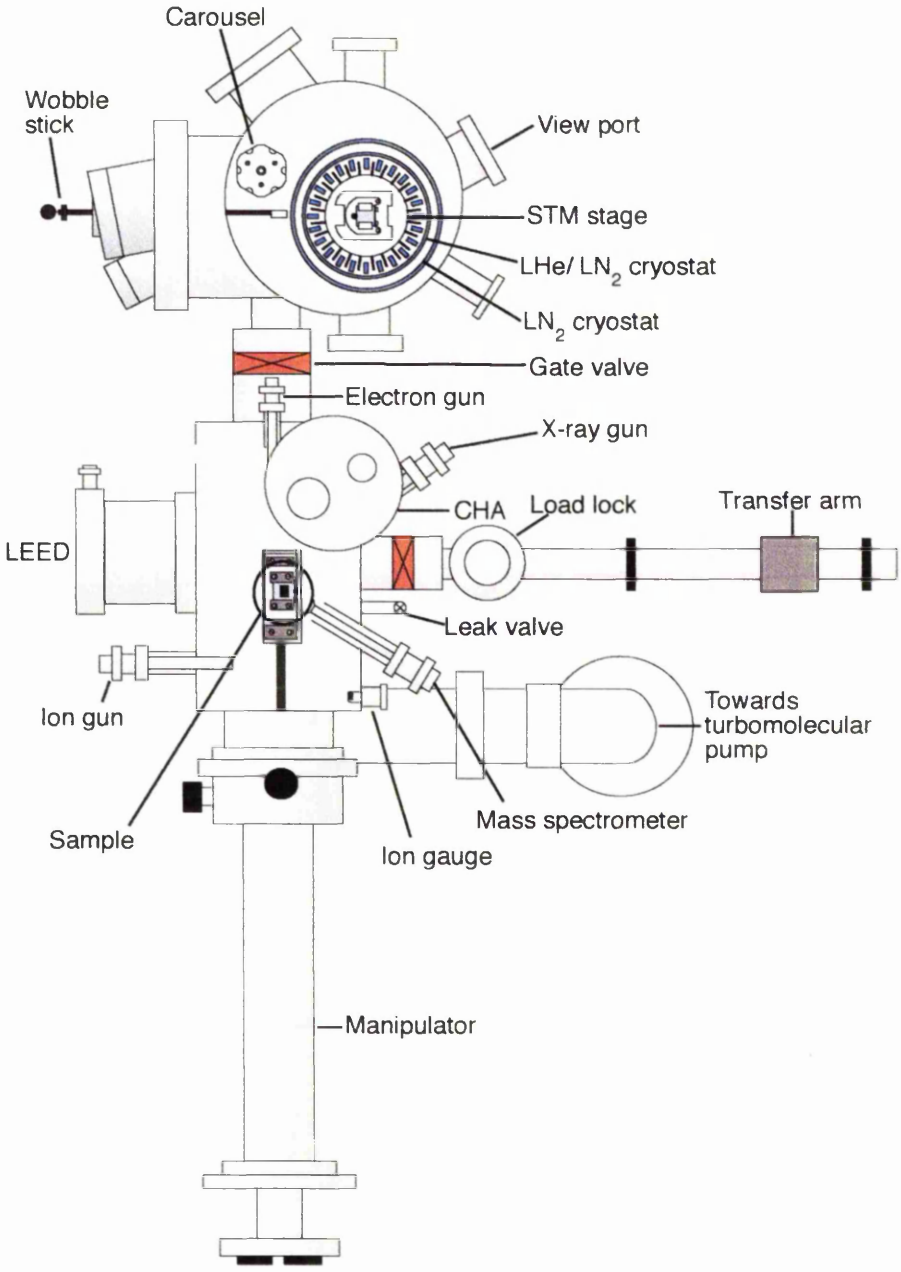


Figure 3.7: Schematic diagram of the low temperature STM UHV system.

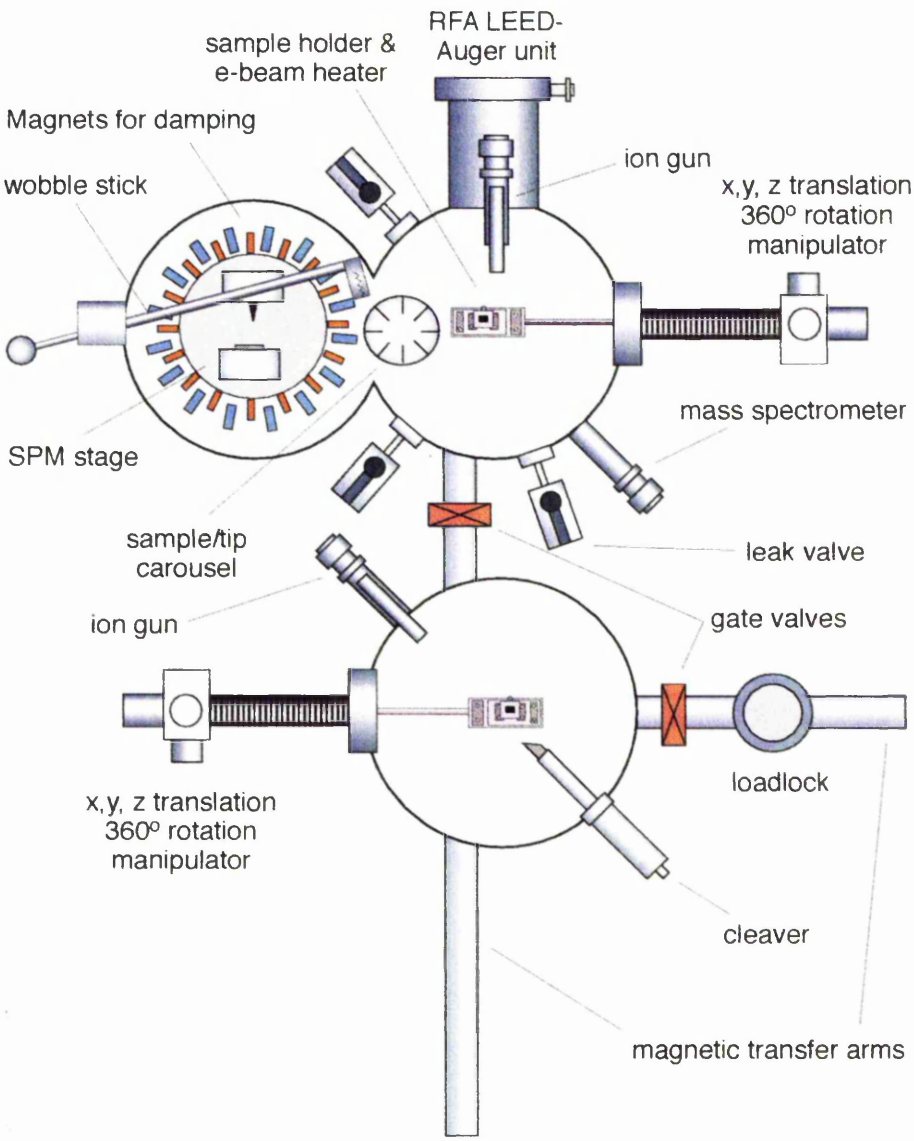


Figure 3.8: Schematic diagram of the room temperature STM/AFM UHV system.

also be used to undertake retarding field AES, using the LEED electron gun and the grids of the LEED optics as an electron energy analyser.

Vacuum is maintained using a combination of pumps. The load locks and preparation chambers evacuated with turbo-molecular pumps, at lower pressures, ion pumps and a titanium sublimation pumps are also used. During STM measurements vibration is minimised by employing only ion and titanium sublimation pumps. After baking to approximately 150 °C, base pressures in the region of $10^{-10}$ mbar are routinely obtained.

Samples are fastened onto tantalum plates with spot welded tantalum strips. The plates are introduced via the load locks and placed on the manipulators with the magnetic transfer arms. When mounted on the manipulator the sample plate may be heated by electron bombardment. The sample temperature may be monitored with a chromel-alumel (K-type) thermocouple and optical pyrometer. The manipulators allow location of a sample within the preparation chamber, and transfer into the STM chamber. Sample plates are transferred between manipulator and STM stage with a pincer-grip "wobble stick".

### 3.3.2 Tip fabrication

Preparation of sharp tips where the tunnelling is limited to a single metal atom or a small atomic cluster at the tip end is crucial if high quality STM images are to be obtained [14], a number of methods for tip preparation have been reported [15]. In the present work, tips were prepared by electrochemical etching. The equipment

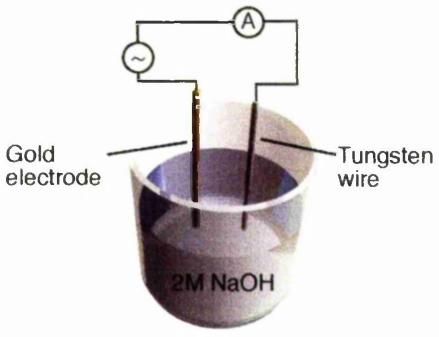


Figure 3.9: Schematic diagram of the electrochemical tip etching apparatus.

used for tip etching is illustrated in figure 3.9. Tungsten wire with a diameter of 0.38 mm is suspended such that it is partially immersed in a 2 M solution of NaOH. The tungsten wire acts as an anode, the NaOH acts as an electrolyte and a gold wire is used as a cathode — a 7 V ac bias generates an etching current of 2–3 A. Etching occurs at the air-electrolyte interface, a neck is formed, and the immersed portion of the wire eventually drops off. The oxide layer coating the tip is immediately washed off with distilled water and acetone, and the tip sharpness is verified by optical microscopy. Once under vacuum, the tip is annealed to ensure the complete removal of the oxide layer and any adsorbed contaminants.

### 3.3.3 Scanning tunneling microscopes

#### Vibration damping

Effective mechanical isolation is essential if atomic resolution images are to be obtained. The instruments were located in basement rooms carefully surveyed

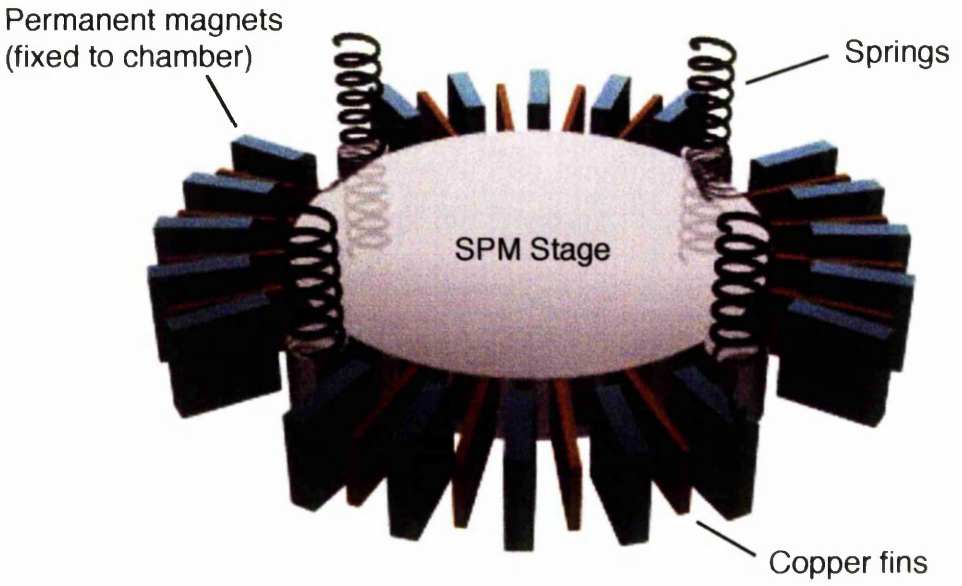


Figure 3.10: Schematic diagram of the vibration isolation mechanism.

for level of structural vibration. During measurements the scanning stages are suspended from four vertical springs. An eddy damping system consisting of copper fins and permanent magnets (figure 3.10) keeps vibrations to a workable minimum.

### Piezoelectric scanner

To form STM images it is necessary to scan the tip across the surface in a regular fashion with angstrom scale precision and repeatability. This is achieved with piezoelectric crystals which change length in response to an applied electric field. The apparatus discussed in this chapter employs a tube form scanner [16] as shown in figure 3.11. The scanner consists of a tube of piezoelectric material surrounded by four electrodes. Movements in the **x** and **y** directions are produced

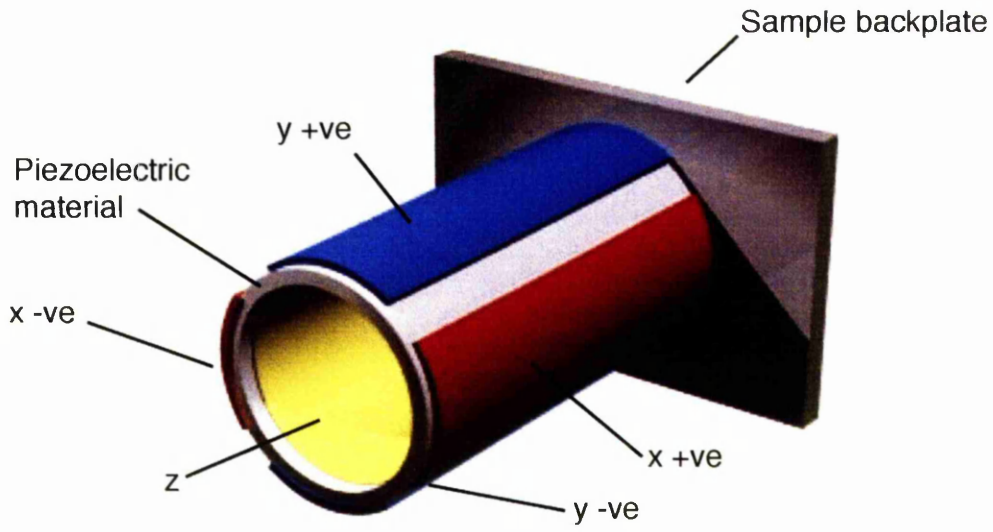


Figure 3.11: Schematic diagram of a piezoelectric tube scanner.

by applying a voltage to two opposite electrodes to bend the tube. The **z** motion is obtained by applying the voltage to the inner electrode to adjust the length of the whole tube. Coarse motion of the tip, in the mm range, is provided by a piezoelectric stick-slip mechanism. This allows the tip to range over the whole of the surface, and allows the tip to be withdrawn for safe exchange of samples.

### STM scanning

STM images are accumulated by regular scanning of an STM tip across the surface whilst recording a signal that acts as a proxy for surface structure. In constant height scanning the tip stays at a constant height above the surface and the tunneling current is recorded. Whilst fast scanning is possible this method is best suited to atomically flat surfaces, and is not ideal for corrugated surfaces such as $TiO_2(110)$.

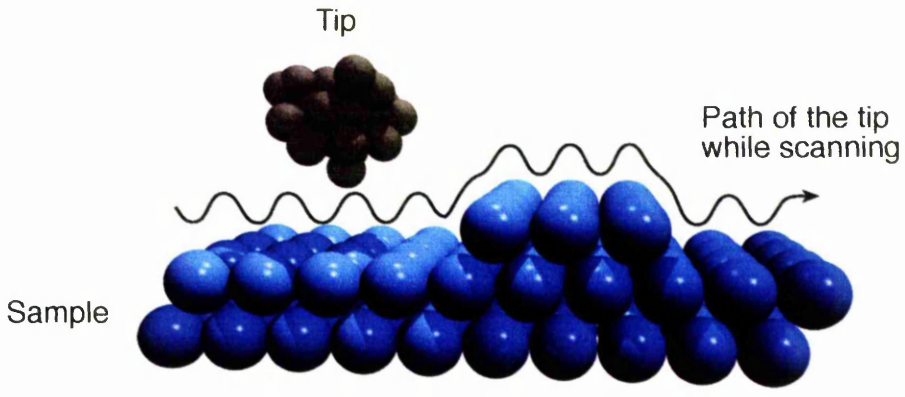


Figure 3.12: Illustration of constant current scanning.

In constant current mode a feedback circuit (figure 3.13) is used to control the height of the tip above the surface to keep the tunneling current constant, and the **z** voltage applied to the tube scanner is recorded. This scanning mode is shown schematically in figure 3.12. Vertical displacement of the tip corresponds to a change in the surface height or a change in the local density of states. This method is preferred for more corrugated surfaces.

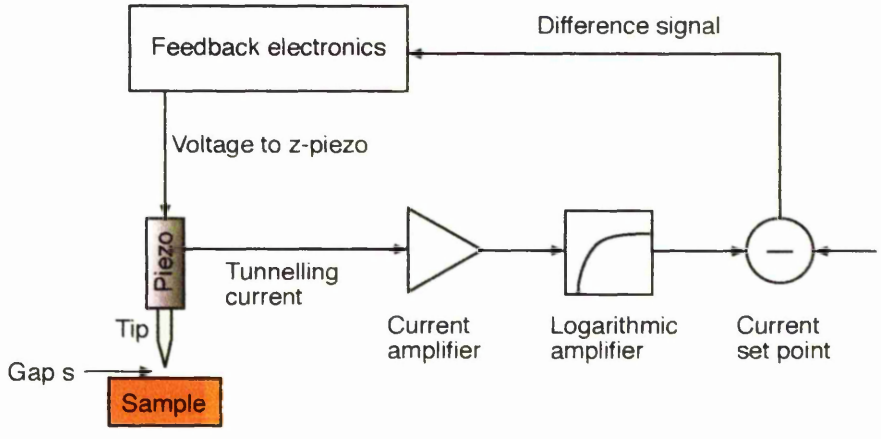


Figure 3.13: Block diagram of the feedback mechanism used for constant current scanning

# References


[1] T.V. Ashworth. *Scanning Probe Microscopy studies on Metal Oxide Surfaces.* PhD thesis, University of Manchester, 2003.

[2] L. Leung. *Microscopy and Spectroscopy of Nanoscale Structures.* PhD thesis, University of Manchester, 2005.

[3] A.J. Limb. *Scanning Tunnelling Microscopy: Studies of Fe, Cr and $SO_2$ Adsorption on Rutile $TiO_2$ (110).* PhD thesis, University of Manchester, 2002.

[4] G. Binnig and H. Rohrer. *Helv. Phys. Acta*, 55:128–128, 1982.

[5] J. Frenkel. *Phys. Rev.*, 36:1604–1618, 1930.

[6] J. Tersoff and D.R. Hamann. *Phys. Rev. Lett.*, 50:1998–2001, 1983.

[7] J. Tersoff and D.R. Hamann. *Phys. Rev. B*, 31:805–813, 1985.

[8] J. Bardeen. *Phys. Rev. Lett.*, 6:57–59, 1961.

[9] R. Wiesendanger. *Scanning probe microscopy and spectroscopy.* Cambridge University Press, 1994.

[10] N.D. Lang. *Phys. Rev. Lett.*, 55:230–233, 1985.

[11] N.D. Lang. *Phys. Rev. Lett.*, 56:1164–1167, 1986.

[12] C.J. Chen. *Phys. Rev. Lett.*, 65:448–451, 1990.

[13] D.A. Bonnel. *Prog. Surf. Sci.*, 57:187–252, 1998.

[14] G. Binning, H. Rohrer, C. Gerber, and E. Weibel. *Phys. Rev. Lett.*, 49:57–61, 1982.

[15] R. Zhang and D.G. Ivey. *J. Vac. Sci. Technol. B*, 14:1–10, 1996.

[16] G. Binnig and D.P.E. Smith. *Rev. Sci. Instrum.*, 57:1688–1689, 1986.

# Chapter 4

# Surface preparation

In this chapter the methods used to prepare flat, well ordered, clean surfaces are briefly described, as are the UHV compatible sources used to create adsorbate covered surfaces. The ancillary surface characterisation techniques employed, low energy electron diffraction (LEED) and Auger electron spectroscopy (AES), are briefly described.

## 4.1 Clean surface preparation

In the present work, surface contamination was removed by bombarding the surfaces with $Ar^+$ ions with energies in the range 0.5–1.0 keV. This leaves a surface which, though clean, is not well ordered. For binary surfaces, such as $TiO_2$ (110), preferential loss of one elemental species is common [1]. Surface order was restored by high temperature annealing. Whilst metals surfaces can

generally be prepared by rapid "flash" annealing, metal oxides generally require protracted periods of annealing to order them [2].

All the apparatus used in the present work employed electron beam bombardment to heat samples. The samples were fixed to refractory metal plates located in front of a tungsten filament. A heating current of a few amps was passed through tungsten filaments, and thermionicaly emitted electrons accelerated towards the sample plate by a positive bias in the region 500–1000 V. Samples can easily be heated to temperatures in excess of 1000 K by this method.

## 4.2 Adsorbate delivery

### 4.2.1 Cyanide

A cyanide covered nickel surface was generated by exposure to a pressure of $1\times10^{-5}$ mbar cyanogen gas ($C_2N_2$). Cyanogen was produced through thermal decomposition of silver cyanide in an evacuated stainless steel tube. The tube was heated resistively to 600 K as measured by a chromel-alumel (K-type) thermocouple. The silver cyanide was degassed by a period of heating under vacuum. Cyanogen gas was introduced into the UHV chamber via a precision leak valve.

### 4.2.2 Calcium

Calcium was deposited from a vapour source based on the design of Taylor and Newstead [3], which is shown in figure 4.1. The source consists of a resistively heated alumina crucible located within a stainless steel heat shield which may be cooled with chilled water. The crucible temperature may be monitored with a chromel-alumel thermocouple, and a shutter provides precise control of dosing time. If the source is thoroughly degassed, then the chamber pressure during dosing stays below $1\times10^{-10}$ mbar.

High purity calcium (99.9%) was evaporated by heating to approximately 650 K. A coverage in the region of one monolayer was formed after dosing for around one minute. Metallic calcium rapidly forms an oxide layer on exposure to air, indeed high purity calcium is packed in an inert atmosphere, thus a preliminary investigation was undertaken to confirm that calcium oxide formation did not affect the purity of the deposited metal. To do so, calcium was dosed onto a clean copper surface which was subsequently probed with AES. No evidence for the deposition of any material other than calcium was found.

### 4.2.3 Sulphur

Sulphur was generated by electrochemical decomposition of silver sulphide in a solid state electrochemical cell, as described by Wagner [5]. The cell is shown schematically in figure 4.2. The cell consists of a silver iodide electrolyte, silver

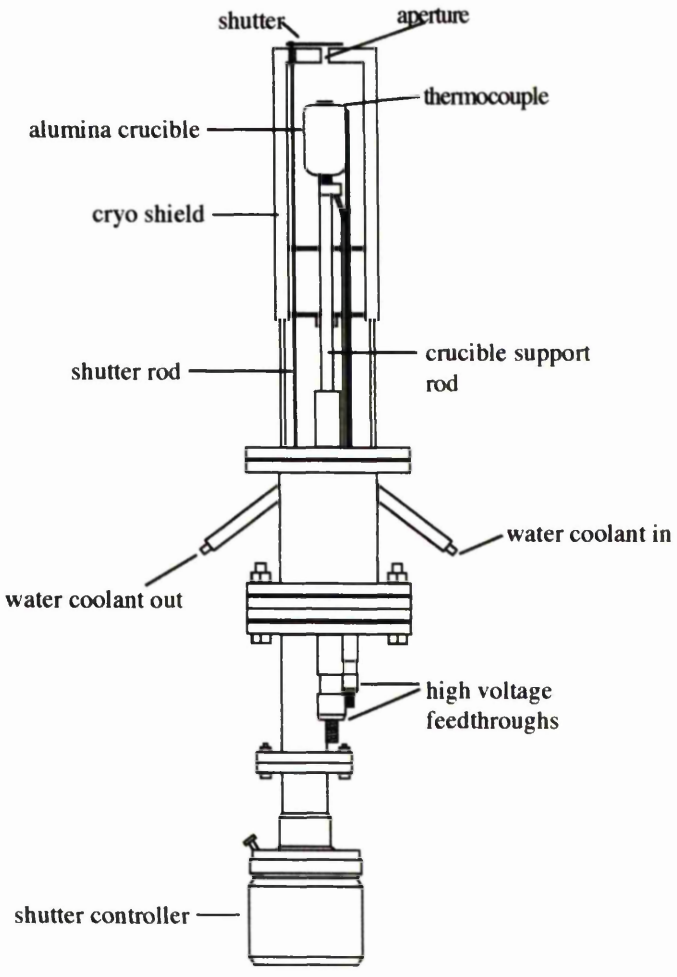


Figure 4.1: Diagram of vapour source used for calcium deposition. Reproduced from [4].

sulphide anode and silver cathode. It has been demonstrated that a cell temperature of 485 K and a driving voltage in the region of 0.15 volts results almost exclusively in $S_2$ formation [6]. This type of cell was first used as a UHV source for surface studies by Heegemann and co-workers [7].

The cell was constructed by pressing silver iodide (99.99%) and silver sulphide (99.9%) into 10 mm diameter pellets, the pellets were contained in a 10 mm

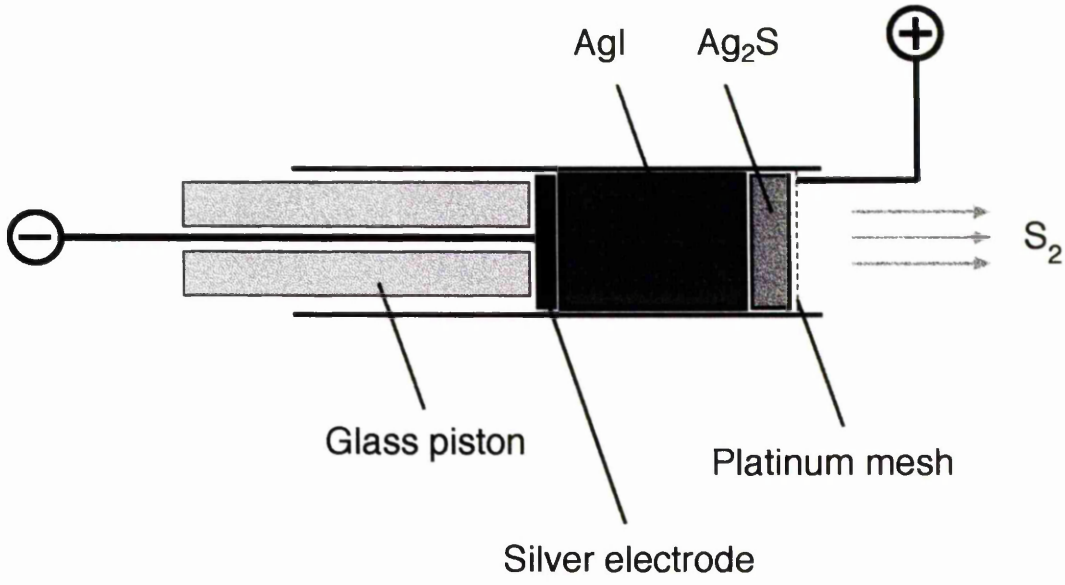


Figure 4.2: Schematic of the electrochemical cell used for sulphur deposition. The heating wires, heat shield and compression springs are omitted for clarity.

internal diameter pyrex tube. The $Ag_2S$ end of the tube was closed with a fine platinum mesh (99.99%) fused into the tube, to provide an electrical connection to the anode and allow egress of $S_2$. The silver cathode (99.97%) was held in place by a sprung glass piston. The pyrex tube was surrounded by a copper foil heat shield, and heating was by a 0.2 mm diameter tungsten wire electrically isolated from the heat shield by ceramic beads. The cell temperature was monitored with a chromel-alumel thermocouple placed under the heat shield. The cell was mounted on a 30 cm long rod attached to a 10 cm travel, linear transfer mechanism to allow positioning near the sample.

A residual gas analyser was used to confirm that only traces of sulphur molecules larger than $S_2$ were present. It was found to be beneficial to heat the cell for

a period of around 1 hour before use, and keep the cell hot between uses. The resistance of the cell provided a convenient indicator of the readiness of the cell. A driving voltage of 0.2 V gave rise to a current flow of approximately 10 mA. If thoroughly degassed, the cell operated in the $10^{-9}$ mbar range.

## 4.3 Low energy electron diffraction

Low energy electron diffraction (LEED) is a widely used and convenient probe of the unit cell dimensions, symmetry and ordering of surfaces. A monochromatic beam of electrons with an energy in the range 20–200 eV is directed at the surface. In this energy range the de Broglie wavelength of the electrons is comparable with inter-atomic spacing, and a sufficiently ordered surface will diffract electrons into a pattern which is a projection of the reciprocal space surface structure. Electrons in this energy range have a mean free path of a few tens of angstroms, rendering the technique surface sensitive.

A conventional LEED apparatus consisting of three concentric grids and a phosphor screen is shown schematically in figure 4.3. The first grid is earthed to provide a field free region between the grid and the sample. The next two grids are held at negative potentials and act to filter out inelastically scattered electrons. The phosphorescent screen is held at a high voltage which accelerates the elastically scattered electrons onto the screen. Sharp spots and a low background indicate that a surface that is well ordered on the scale of the electron beams coherence width — typically $\sim$ 100 Å. A comprehensive treatment of the LEED technique is given in [8].

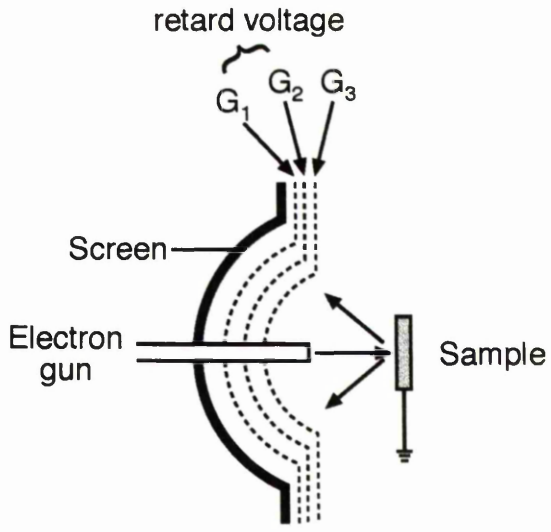


Figure 4.3: Schematic diagram of the LEED apparatus. Electrons are back scattered form the surface. Grid $G_3$ provides a field free region, and grids $G_2$ and $G_1$ filter out inelastically scattered electrons. Elastically scattered electrons are accelerated towards the phosphor screen which fluoresces in the presence of an electron beam.

## 4.4 Auger electron spectroscopy

In the present work, Auger electron spectroscopy (AES) was used as a convenient indicator of the cleanliness of surfaces, and as an approximate indicator of the adsorbate coverage. A detailed description of the technique can be found in [9].

If a surface is irradiated with X-rays or bombarded with energetic electrons a core electron may be ejected and an electron will drop from a higher energy level to fill the vacancy. The excess energy is either emitted as a photon or communicated to a shallowly bound electron which leaves the atom; this is the Auger process. The energy of the Auger electron is determined by the energy levels of the atom, and is independent of the irradiating energy. Thus Auger electrons occur at characteristic energies which are well known and can be used to identify the

elemental species present on a surface. The surface sensitivity of this technique arises from the short mean free path of the emitted Auger electrons, whose energy typically falls in the range 10–1000 eV, resulting in a mean free path of less than 20 Å.

In practice, an electron beam energy in the region of 3 keV is typically employed. In the present work a variety of different electron energy analysers were employed, and the reader is referred to [9] for a detailed account of the operation of electron energy analysers. It is noted that Auger peaks are generally small features on a rising background of secondary electrons, and some processing of the data is required to clearly identify features.

# References


[1] U. Diebold. *Surf. Sci. Rep.*, 48:53–229, 2003.

[2] V.E. Henrich and P.A. Cox. *The surface science of metal oxides.* Cambridge University Press, 1994.

[3] J.S.G. Taylor and D.A. Newstead. *J. Phys. E*, 20:1288–1289, 1987.

[4] G.M. Charlton. *Atomic structure of transition metal oxide surfaces and interfaces.* PhD thesis, University of Manchester, 1997.

[5] C. Wagner. *J. Chem. Phys.*, 21:1819–1827, 1953.

[6] D. Detry, J. Drowart, P. Goldfing, H. Keller, and H. Rickert. *Z. Phys. Chem. (Frankfurt am Main)*, 55:314–319, 1967.

[7] W. Heegemann, K.H. Meister, E. Bechtold, and K. Hayek. *Surf. Sci.*, 49:161–180, 1975.

[8] L.J. Clarke. *Surface crystallography - An introduction to low energy electron diffraction.* Wiley-Interscience, 1985.

[9] D.Briggs and M.P. Seah. *Practical surface analysis.* John Wiley and sons, 2nd edition, 1996.

# Chapter 5

# A surface X-ray diffraction study of Ni(110)c(2×2)-CN

## 5.1 Introduction

Understanding the interaction of cyanide (CN) with solid surfaces is of significant interest, both fundamentally and technologically (e.g. [1, 2] ). This has stimulated a range of fundamental studies of the adsorption of CN on model metal surfaces in ultra high vacuum, for example [3–12]. One conclusion of note emerging from this body of work is that $CN^-$ typically bonds with its molecular axis approximately parallel to the surface plane. This adsorption geometry contrasts sharply with the end-on binding configuration characteristically exhibited by its isoelectronic counterpart CO, and other diatomics (e.g. NO, $N_2$) [13]. One specific example of a system adopting this flat-lying adsorbate geometry, which has been the subject

of a number of previous investigations [3, 6–9], including several quantitative structural determinations [10–12], is Ni(110)c(2×2)-CN.

The first quantitative structural study of Ni(110)c(2×2)-CN employed scanned-energy mode photoelectron diffraction (PhD) from the C and N 1s core levels, in tandem with near edge X-ray absorption fine structure (NEXAFS) measurements [10]. As indicated above, the C–N bond axis was found to be approximately parallel to the surface plane. Yet contrary to previous angle resolved photoemission and cluster calculations [7], which concluded that the CN molecular axis was oriented along the $[1\bar{1}0]$ azimuth (i.e. parallel to the close packed surface Ni rows), a perpendicular azimuthal orientation was elucidated. Furthermore, it was determined that CN is located above a second layer Ni with C being approximately 3-fold co-ordinated to Ni atoms, and N bridging two surface Ni atoms. A space filling model of a c(2×2)-CN overlayer on Ni(110), exhibiting this local adsorption geometry, is shown in figure 5.1.

Interestingly, it is stated in the PhD/NEXAFS study that the fractional order c(2×2)-CN low energy electron diffraction (LEED) beams are relatively intense, suggesting that the adsorbate overlayer may induce a substrate reconstruction [10]. On this basis several reconstructed surface models were tested during the PhD analysis, but no positive evidence for reconstruction emerged. However, as PhD primarily probes the location of atoms closest to the photoelectron emitters (i.e. C and N), it is reasonable to suppose that this technique may be insensitive to atomic displacements involved in the reconstruction (e.g. second Ni layer rumpling). Given this limitation further structural determinations of

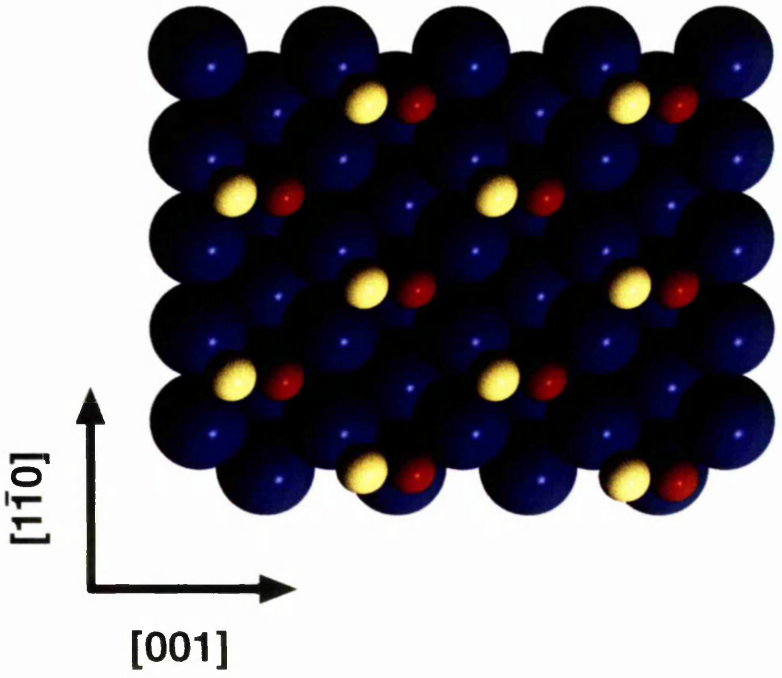


Figure 5.1: Space filling model of the geometry of Ni(110)c(2×2)-CN, as determined by PhD [10]. Larger spheres represent Ni atoms, the smaller red spheres represent C and the yellow spheres N.

Ni(110)c(2×2)-CN have been undertaken. Medium energy ion scattering (MEIS) has been used to investigate the relaxation of the surface [11], and quantitative LEED (LEED-IV) has been used to explore the possibility of substrate reconstruction [12]. Since the publication of the present work [14] this system has also been investigated with density functional theory (DFT) [15]. Both this work and the LEED-IV study explicitly investigated the possibility of substrate reconstruction, and conclude that the surface does not reconstruct to any significant degree.

In this chapter the question of adsorbate-induced substrate reconstruction of Ni(110)c(2×2)-CN is revisited with surface X-ray diffraction (SXRD) [16]. Given

that SXRD is rather sensitive to lateral atomic displacements, as has been amply demonstrated by its successful application to the reconstruction of a number of metal and semiconductor surfaces [16], this investigation complements the previous quantitative structural determinations [10–12].

## 5.2 Experimental details

Experimental work was conducted at beamline 9.4 [17] of the Synchrotron Radiation Source, Daresbury, employing the ultra high vacuum (UHV) endstation INGRID. A full description of the beamline and instrumentation is given in chapter 2. In-situ surface preparation consisted of repeated cycles of argon ion bombardment and substrate annealing to approximately 1000 K, to form a clean and well ordered Ni(110) surface, followed by generation of a c(2×2) overlayer of CN. This latter task was achieved by exposing the Ni sample, at room temperature, to cyanogen gas ($C_2N_2$) admitted to the chamber via a precision leak valve. From previous studies, it is well known that cyanogen adsorbs dissociatively on Ni(110) to form an ordered overlayer of CN moieties [7]. Cyanogen was produced by thermal decomposition of well-degassed silver cyanide, located in an evacuated stainless steel tube. LEED and Auger electron spectroscopy (AES) were utilised to assess surface order and composition respectively. The presence of the c(2×2)-CN phase was confirmed by the observation of sharp, intense, fractional order LEED beams.

For the SXRD measurements, INGRID was coupled to a five-circle diffractometer, equipped with an additional manual sixth circle, which almost doubles the amount of accessible reciprocal space in the out-of-plane direction [18]. An X-ray wavelength of 0.9 Å was selected to maximise the available reciprocal space, whilst maintaining a usable photon flux. Data were accumulated using rocking scans in which the sample is rotated about its surface normal while the scattered X-ray intensity is recorded with a cryogenically cooled, single element, germanium detector. Such scans were performed for a given integer $(h, k)$ as a function of $l$, providing profiles of scattered intensity, $I_{hk}$, versus perpendicular momentum transfer — crystal truncation rods (CTRs). Also, in-plane rocking scans were acquired at both integer and appropriate fractional $(h, k)$ points, using small incidence and exit angles for the X-rays to give small values of perpendicular momentum transfer ($l = 0.15$). All data were recorded with the substrate at room temperature. LEED and AES were used to monitor possible degradation of the surface.

The resulting scans were integrated and corrected for effective sample area, X-ray beam polarisation and Lorentz factor to give structure factor amplitudes. Wherever possible, one or more symmetry-equivalent reflections were recorded and equivalent structure factors were averaged together to give the final data set. The variation between equivalent data points was used to estimate the systematic error, which at $\sim \pm 8\%$ is the dominant error in the data set. The data are indexed with reference to the (1×1) unit cell of the (110) surface; defined such that $\mathbf{a_1}$ and $\mathbf{a_2}$ are orthogonal in the plane of the (110) surface, in the [001] and [0$\bar{1}$1]

directions respectively, with $\mathbf{a_3}$ perpendicular to the surface in the [110] direction. The magnitudes of the vectors are $a_1 = a_0$ and $a_2 = a_3 = \frac{a_0}{\sqrt{2}}$ where $a_0 = 3.52$ Å is the lattice constant of nickel. Reciprocal space axes $h, k, l$ are parallel to $\mathbf{a_1}$, $\mathbf{a_2}$ and $\mathbf{a_3}$, respectively. Integer $h, k$ corresponds to to crystal truncation rods, and $h, k = \frac{1}{2}, \frac{3}{2}, \frac{5}{2} \ldots$ corresponds to fractional order data.

## 5.3 Results

The collected data consisted of 104 symmetry inequivalent reflections including three CTRs ($(h,k) = (1,0), (1,1)$, and $(0,1)$), and an in-plane data set consisting of 11 points up to $\mathrm{h}_{max} = 4$ and $\mathrm{k}_{max} = 3$. It is important to note that significant intensity was found at only one fractional order reflection, namely $(\frac{1}{2}, \frac{1}{2})$, at all other such points it was not possible to resolved diffraction features above the baseline noise of the scan. Crystal truncation rod data is displayed in figure 5.2 and in-plane data is displayed in figure 5.3.

As a first step towards elucidating the structure of the Ni(110)c(2×2)-CN phase, vertical shifts of entire Ni layers beneath a c(2×2)-CN overlayer were considered. Permitting the two uppermost surface Ni layers to relax in this fashion led to a significant improvement in $\chi^2_\nu$, reducing it from 10.9 for the bulk terminated surface to 2.33. It was ascertained that the present SXRD data are poorly sensitive to the positions of C and N, due to the weak X-ray scattering of both of these atoms relative to Ni. In consequence CN was treated as a rigid unit (Svenssons Extension to ROD [19]), and confined to the adsorption geometry determined

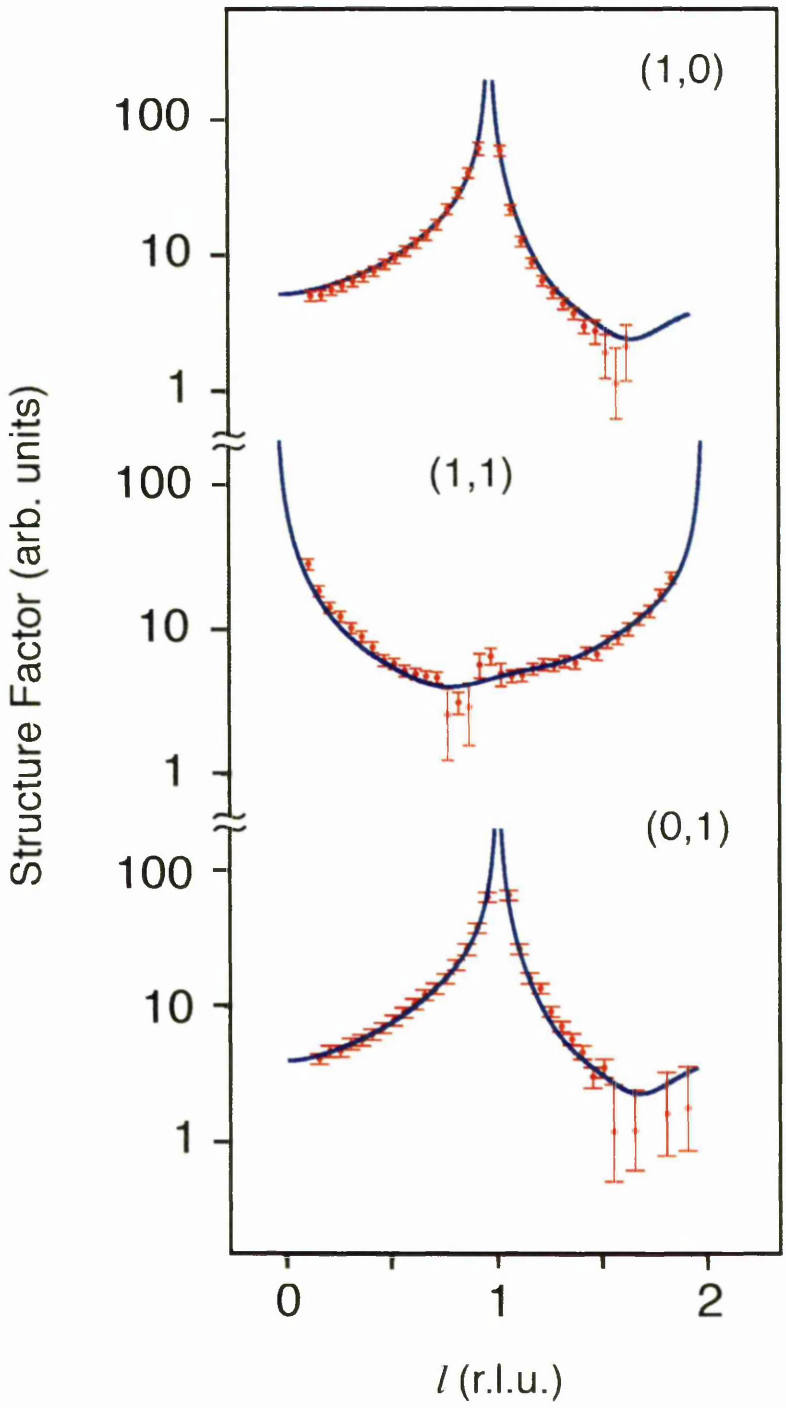


Figure 5.2: Comparison of crystal truncation rod data and calculated best fit model data. Structure factors (F) are given in arbitrary units, out-of-plane momentum transfer ($l$) is given in reciprocal lattice units. Experimental data are plotted in red with error bars, calculated data are shown as a continuous blue line.

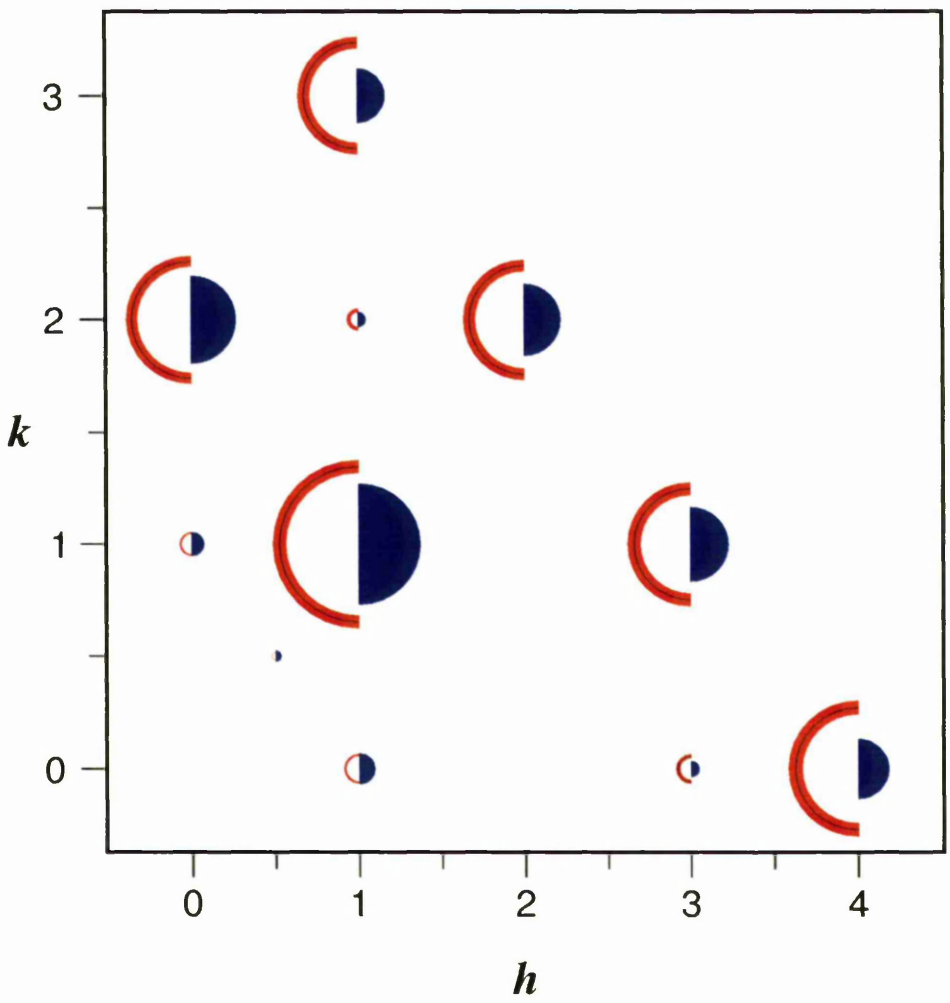


Figure 5.3: Reciprocal space diagram of in-plane structure factors measured at $l = 0.15$. Calculated structure factors are represented by filled blue semi-circles with radius proportional to the structure factor. Experimental data is represented by a red arc whose inner and outer radii represent the lower and upper error bars. For $F_{h,k,0.3} > 0.7$ the measured structure factor is represented as a thin black arc. Note the single fractional order point at $(\frac{1}{2}, \frac{1}{2})$.

from PhD [10], with only the vertical height of the ensemble being optimised.

Subsequent to the above optimisation, evidence for further substrate distortion, or even reconstruction was sought. Mimicking the previous LEED-IV study [12], a comprehensive range of geometrical models consistent with a c(2×2) translational symmetry were explored. Structures tested included one in which every second surface layer Ni atom was absent, a second involving alternate lateral shifts of the surface layer Ni atoms in the [001] azimuth to form zigzag chains, and another consisting of vertical rumpling of the topmost Ni layer. In addition to these models, which all reduce the point group of the surface, atomic displacements which maintain this symmetry were also probed, including vertical rumpling and lateral shifts in the [001] azimuth of second layer Ni atoms. Models involving the topmost Ni layer are illustrated in figure 5.4.

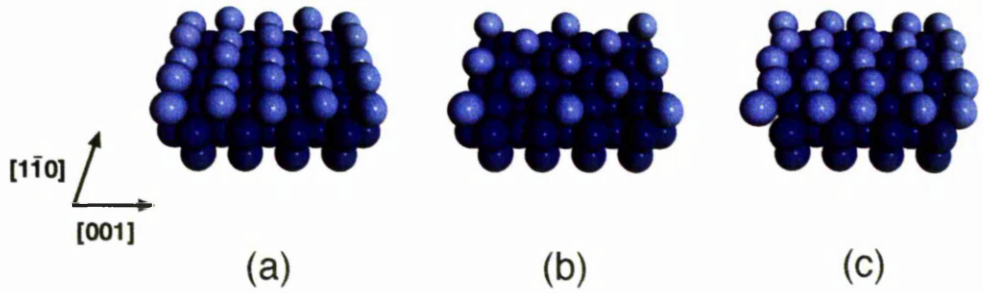


Figure 5.4: Ball models illustrating investigated top layer reconstructions; (a) rumpling (b) systematic absences (c) alternate lateral shifts.

No significant improvements in the fit between experiment and theory emerged from this rather extensive survey of geometrical parameter space, with $\chi^2_\nu$ typically becoming larger for any substantive atomic displacements away from the simple relaxed layer model. For example, a lateral zigzag of the first layer Ni

atoms in the [001] azimuth of 0.1 Å increases $\chi^2_\nu$ to 2.59, and the lowest $\chi^2_\nu$ found for the model in which every second surface Ni atom is missing is greater than 9. The best fit obtained was for a structure exhibiting a top layer vertical rumple of magnitude 0.13 Å. However, despite the introduction of an additional geometric parameter the improvement in $\chi^2_\nu$ is minimal, being reduced to 2.29 from a value of 2.33 for the simple relaxed surface; the author is confident that this improvement in $\chi^2_\nu$ may be regarded as insignificant. Thus it is concluded that the Ni(110)c(2×2)-CN surface does not display any substantial substrate atom displacements beyond simple vertical relaxations.

A comparison of experimental and theoretical CTR data for the fully optimised structure, involving only vertical relaxation of substrate layers, is shown in figure 5.2, and a comparison of experimental and theoretical in-plane data is shown in figure 5.3. A model of the structure is displayed in figure 5.5. As implied in this figure the third layer of Ni atoms was allowed to relax in a final cycle of structural optimisation. This procedure reduced $\chi^2_\nu$ to 2.15, although clearly the displacement of this layer is not strictly significant as it has a value of 0.02±0.02 Å. The position of the CN species is not noted, as the associated error is so great (approximately ±0.4 Å) that this information is of little value. Following the earlier LEED work [12], the vibrational amplitude (Debye-Waller parameter) of top layer Ni atoms, and the CN molecule were optimised. Whilst this improved the quality of fit, the impact on the geometrical parameters of the final structure was minimal.

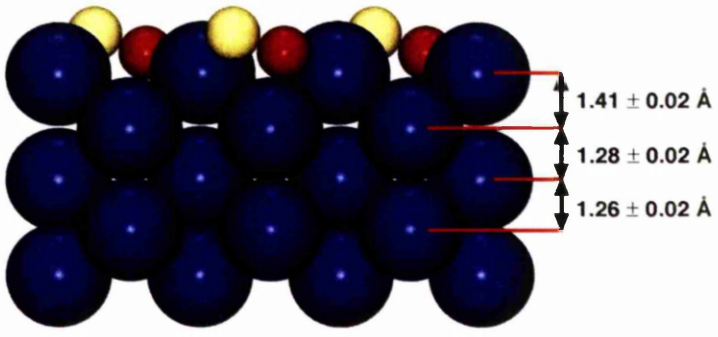


Figure 5.5: Side view of the optimised geometry, with values of the optimised structural parameters inserted. No values for CN are given as the SXRD analysis resulted in an ill-defined position.

## 5.4 Discussion

In Table 5.1 the percentage expansion, derived from this study, of the spacing ($\mathbf{z}_{12}$) between the top two Ni layers relative to bulk separation is compared to results obtained from earlier work [10–12] and recent DFT calculations [15]. This list clearly demonstrates that all the studies are consistent in that a significant increase in this spacing is found. The value obtained in this work ($11 \pm 2\%$) agrees well, within experimental uncertainty, with those obtained from PhD ($15 \pm 10\%$) [10], LEED-IV ($9 \pm 4\%$) [12] and DFT (11%) [15]. In contrast, the $21 \pm 2\%$ expansion obtained from MEIS [11] is significantly larger than any of the other determinations. Currently, the origin of this discrepancy is not readily apparent, although given the agreement between the other results it is the MEIS study [11] that should probably be re-evaluated.

Besides determination of simple vertical relaxation, further distortion or reconstruction of the substrate was rigorously investigated in the LEED-IV study [12].

| Technique | $z_{12}$ expansion |
|---|---|
| This work (SXRD) | 11 ± 2% |
| PhD [10] | 15 ± 10% |
| MEIS [11] | 21 ± 2% |
| LEED [12] | 9 ± 4% |
| DFT [15] | 11% |

Table 5.1: Expansion of spacing ($z_{12}$) between top two Ni layers relative to bulk separation, derived from the various experimental and theoretical studies

It was found that the most significant displacement was a lateral zigzag distortion of the second Ni layer in the [001] azimuth, having an amplitude of 0.17±0.09 Å. On the contrary, despite similarly exhaustive searching, no evidence for this or any other distortion was found in the present case. In fact, constraining the model to incorporate such a zigzag, causes the experiment-theory fit diverge, with $\chi^2_\nu$ increasing somewhat to 2.44. The source of this disparity between the studies is not clear, however recent DFT investigations [15] explicitly test this motion and find it is not energetically favourable. Acquisition of further SXRD data at a third generation light source where greater flux is available at shorter wavelengths would resolve this issue, both by providing greater sensitivity to the typically weak fractional-order overlayer data, and extending the volume of reciprocal space probed.

It is intriguing to note that c(2×2)-CN overlayers are reported on the (110) surfaces of three fcc transition metals; Ni [10], Rh [4] and Pd [5], and in each case cyanide is found in the same position with a tilt in the range 18–25°. However

in contrast to results for adsorption on Ni, where no reconstruction was found, formation of the c(2×2)-CN overlayer on Rh leads to a rumpling of the second layer of the substrate with a vertical Rh-Rh separation of $0.09 \pm 0.02$ Å. In light of this difference, it will be of some interest to see if the formation of a c(2×2)-CN overlayer on Pd gives rise to any reconstruction of the substrate. As far as the author is aware no attempt has yet been made to investigate the substrate structure in this case. SXRD and LEED-IV are obvious methods for such an investigation, and it is noted that a study of CO on Ni(110) [20] implies that SXRD measurements at a third generation source should be able to resolve the position of the CN molecule.

## 5.5 Summary

SXRD has been used to study the structure of Ni(110)c(2×2)-CN, focusing primarily on the geometry of the metal substrate. It has been determined that the ordered CN phase produces significant substrate relaxation, but no significant reconstruction of the metal is demonstrated. A value of $11 \pm 2\%$ has been derived for the expansion of the spacing between the top two Ni layers, relative to bulk termination. This value agrees well with earlier determinations of this parameter, using PhD [10] and LEED [12] as well as the results of subsequent DFT calculations [15].

# References


[1] R.M. van Hardeveld, A.J.G.W. Schmidt, R.A. van Santen, and J.W. Niemantsverdriet. *J. Vac. Sci. Technol. A*, 15:1642–1646, 1997.

[2] D.R. Mullins, L. Kundakovic, and S.H. Overbury. *J. Catal.*, 195:169–179, 2000.

[3] F.P. Netzer and M.G. Ramsey. *Crit. Rev. Sol. State.*, 17:397–475, 1992.

[4] F. Bondino, A. Baraldi, H. Over, G. Comelli, P. Lacovig, S. Lizzit, G. Paolucci, and R. Rosei. *Phys. Rev. B*, 64:085422, 2001.

[5] F. Bondino, E. Vesselli, A. Baraldi, G. Comelli, A. Verdini, A. Cossaro, L. Floreano, and A. Morgante. *J. Chem. Phys.*, 118:10735–10740, 2003.

[6] M.G. Ramsey, D. Steinmuller, F.P. Netzer, M. Neuber, L. Ackermann, J. Lauber, and N. Rosch. *Surf. Sci.*, 260:163–174, 1992.

[7] M.G. Ramsey, D. Steinmuller, F.P. Netzer, S. Kostlmeier, J. Lauber, and N. Rosch. *Surf. Sci.*, 309:82–88, 1994.

[8] I. Kardinal, F.P. Netzer, and M.G. Ramsey. *Surf. Sci.*, 376:229–236, 1997.

[9] R.I.R. Blyth, I. Kardinal, F.P. Netzer, M.G. Ramsey, D. Chrysostomou, and D.R. Lloyd. *Surf. Sci.*, 415:227–240, 1998.

[10] N.A. Booth, R. Davis, D.P. Woodruff, D. Chrysostomou, T. Mccabe, D.R. Lloyd, O. Schaff, V. Fernandez, S. Bau, K.M. Schindler, R. Lindsay, J.T. Hoeft, R. Terborg, P. Baumgartel, and A.M. Bradshaw. *Surf. Sci.*, 416:448–459, 1998.

[11] D. Brown, D.P. Woodruff, T.C.Q. Noakes, and P. Bailey. *Surf. Sci.*, 476:L241–L246, 2001.

[12] C. Bittencourt, E.A. Soares, and D.P. Woodruff. *Surf. Sci.*, 526:33–43, 2003.

[13] H. Over. *Prog. Surf. Sci.*, 58:249–376, 1998.

[14] B.G. Daniels, F. Schedin, O. Bikondoa, G. Thornton, and R. Lindsay. *Surf. Sci.*, 572:433–438, 2004.

[15] M.J. Knight, J. Robinson, and D.P. Woodruff. *Surf. Sci.*, 580:145–152, 2005.

[16] E. Vlieg and I.K. Robinson. Two-dimensional crystallography. In P. Coppens, editor, *Synchrotron Radiation Crystallography*. Academic Press, 1992.

[17] C. Norris, M.S. Finney, G.F. Clark, G. Baker, P.R. Moore, and R. Vansilfhout. *Rev. Sci. Instrum.*, 63:1083–1086, 1992.

[18] J.S.G. Taylor, C. Norris, E. Vlieg, M. Lohmeier, and T.S. Turner. *Rev. Sci. Instrum.*, 67:2658–2659, 1996.

[19] O. Svensson and D-M Smilgies. *Manual for Svenssons extension to ROD.*

[20] K.F. Peters, C.J. Walker, P. Steadman, O. Robach, H. Isern, and S. Ferrer. *Phys. Rev. Lett.*, 86:5325–5328, 2001.

# Chapter 6

# A surface X-ray diffraction study of $TiO_2(110)(3\times1)$-S

## 6.1 Introduction

The absorption of elemental sulphur and sulphur-containing molecules on metal and metal oxide surfaces has been extensively studied; see [1, 2] for reviews of previous work. Whilst atomic scale studies of the adsorption of sulphur on well ordered surfaces is an interesting field of fundamental research in its own right, major motivators for such work include the study of sulphur poisoning of catalysts and the development of novel desulphurisation catalysts. Such work is particularly relevant to the petrochemical industry; sulphur containing compounds are ubiquitous in petrochemical feedstocks [3], and the annual cost to the industry of sulphur poisoning runs to many millions of dollars [4, 5]. However catalyst

poisoning by sulphur is a complex process and remains poorly understood [6]. Increasingly stringent controls on sulphur emissions stemming from environmental concerns are motivating considerable research into so called "deep desulphurisation" [7] which aims to produce very low sulphur fuels. The prediction by some observers that currently rising oil prices presage an irreversible fall in global oil production, and concomitant steep rises in oil prices within the present decade [8], can only strengthen the social and economic imperative of such work.

The development of improved catalysts that are more resistant to sulphur poisoning, and more efficient desulphurisation catalysts, will be facilitated by a fundamental understanding of the structure and electronic properties of surfaces with adsorbed sulphur. Such an understanding of complex real life systems is dependent on studies of well ordered model systems, particularly low-index single crystal surfaces. The study of sulphur adsorption on metal oxides is of particular interest; they are widely used as catalysts and catalyst supports [5] and, as they offer both metal and oxygen sites, they allow the formation of surface species with considerably different electronic properties (sulphides and sulphates). In general, $SO_2$ species are seen to react with oxygen sites and form $SO_x$, whereas molecular sulphur, and sulphur generated by dissociation of sulphur containing molecules tends to react with metal sites [2]. Titanium dioxide, which is the subject of the present work, is sometimes employed as a catalyst in the Claus hydrodesulphurisation process, which is widely used on a commercial scale [5], and is employed in at least one novel hydrodesulphurisation catalyst [9].

Although a number of studies of adsorption of sulphur containing molecules ($SO_2$

and $H_2S$) on $TiO_2$ surfaces have been undertaken [10], until recently no studies of adsorption of elemental sulphur had been published. In two papers Diebold and co-workers have identified a variety of surface phases arising from the absorption of elemental sulphur using STM, LEED and XPS [6, 11]. This work has been supplemented by various photoemission studies [12–14], thermal desorption mass spectroscopy [14], a first principles DFT investigation [14], and a study of the effect of the reduction state of the substrate [12]. More recently first principle molecular dynamics simulations published by Langel [15] have attempted to elucidate the mechanisms by which sulphur adsorbs on the surface.

At room temperature, STM shows sulphur adsorbing on the rows of 5-fold coordinated titanium atoms with considerable mobility in the [001] direction, but no long range order has been reported [6]. Molecular sulphur is thought to adsorb dissociatively and bind weakly to the 5-fold titanium atoms — see section 1.2 for a description of the clean $TiO_2$(110) surface. UPS studies show a shallow defect state in the band gap of the clean surface, attributed to bridging oxygen vacancies, which rapidly disappears on adsorption of sulphur at room temperature, indicating the small number of bridging oxygen vacancies as a preferred adsorption site [12, 13]. This interpretation has been confirmed by two independent sets of density functional theory calculations [14, 15]. High-resolution S 2p photoemission resolves features attributed to sulphur adsorbed on the 5-fold titanium rows, sulphur in bridging oxygen vacancies and additionally reveals a minority of $SO_x$ species [14]. In agreement with the UPS work, sulphur is seen to occupy the bridging oxygen vacancies first. DFT calculations indicate that the adsorption

energy of sulphur on different sites decreases in the following sequence [14]:

$$\begin{matrix}\text{bridging oxygen}\\\text{vacancies}\end{matrix} > \begin{matrix}\text{atop 5-fold titanium}\\\text{atoms}\end{matrix} > \begin{matrix}\text{bridging oxygen}\\\text{rows } (SO_x)\end{matrix}$$

Hence the defects are populated first and only then does sulphur adsorb on the 5-fold rows. Recent first principle molecular dynamics simulations [15] confirm that $S_2$ dissociates at room temperature but in contrast to the other work, sulphur on the 5-fold titanium atoms was not found to be stable, rapidly reacting with bridging oxygens to form SO.

On heating a surface dosed with sulphur at room temperature to between 390 K and 700 K, or dosing sulphur directly onto a surface in this temperature range, the S 2p photoemission peak is seen to shift to a 2 eV lower binding energy than found for sulphur dosed at room temperature. This is attributed to the formation of S–Ti rather than S–O species [6, 11]. On annealing above 420 K a low binding energy shoulder on the titanium $2p_{3/2}$ XPS peak, attributed to $Ti^{3+}$ states, is observed. This suggests formation of under-coordinated titanium atoms due to the loss of surface oxygen, hence sulphur is thought to replace oxygen atoms in this regime [6, 11]. Adsorption at higher temperatures leads to larger saturation sulphur coverage [14], and larger $Ti^{3+}$ shoulders [11].

A series of well ordered surface structures have been observed with LEED and STM. Adsorption between 470 K and 570 K gives rise to a $(3\times1)$-S structure [6, 11], which is the subject of the present work. STM images at low sulphur coverage show the adsorption of sulphur on the bridging oxygen rows. Taken with the shift in the S 2p peak, and a 6% contribution of the $Ti^{3+}$ shoulder to the Ti $2p_{3/2}$ XPS peak, it was concluded that the $(3\times1)$ structure is formed by

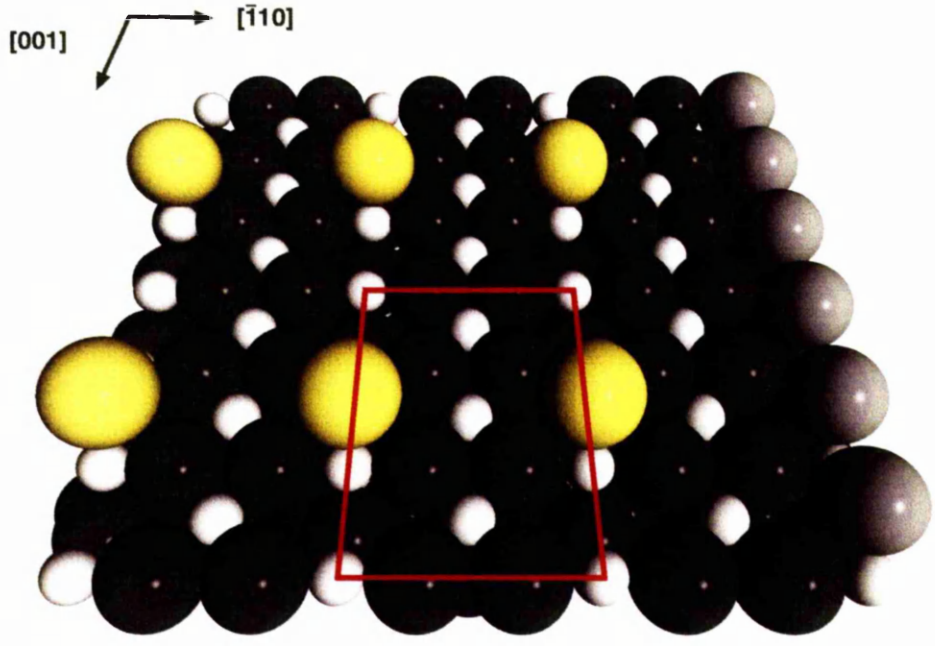


Figure 6.1: Space filling model of the $TiO_2$(110)(3×1)-S structure proposed by Diebold [6]. Sulphur adsorbs bridging 6-fold co-ordinated titanium atoms, displacing all bridging oxygens. Sulphur is represented by yellow spheres, oxygen by black spheres and titanium by white spheres. At the right of the figure a row of bridging oxygen atoms (over 6-fold titanium atoms) represented by grey spheres, is retained for comparison. A (3×1) unit cell is outlined in red.

the complete removal of bridging oxygens, one of which is replaced by a sulphur atom [6], see illustration in figure 6.1. This model is supported by subsequent temperature programed high-resolution photoemission of a room temperature dosed surface, which on heating to 550 K, shows the disappearance of features attributed to sulphur on the 5-fold titanium rows, leaving only sulphur previously associated with bridging oxygen vacancy sites [14]. The stability of the proposed (3×1)-S phase has been confirmed by recent first principles molecular dynamics simulations, however a model where one bridging oxygen per (3×1) unit cell is retained was also found to be stable [15].

Sulphur adsorption between 570 K and 670 K gives rise to a (3×3)-S structure at intermediate coverage and a (4×1)-S structure at saturation coverage [11]. From STM and XPS, these patterns are attributed to sulphur pairs replacing some in-plane oxygen pairs as well as the loss of bridging oxygens. In the case of the (4×1)-S overlayer the $Ti^{3+}$ shoulder contributes 16% of the total peak area, suggesting more oxygen is removed than in the (3×1)-S case. In a subsequent photoemission study, the shallow defect state previously alluded to is seen to be enhanced and shifted to a lower binding energy on formation of a (4×1) LEED pattern. Coupled with a strongly reduced O 2s peak, this suggests replacement of a significant portion of surface oxygens with sulphur [13]. Hence a model was proposed in which sulphur replaces 50% of the in-plane oxygens [11]. High-resolution S 2p photoemission of a surface saturated with sulphur at 600 K and 700 K shows a small amount of sulphur in the position previously attributed to sulphur in bridging oxygen vacancies, and a dominant doublet at 1.4 eV lower binding energy, attributed to sulphur replacing in-plane oxygen atoms [14].

It has been demonstrated that the sulphur coverage increases as a function of the bulk defect concentration of the substrate, as indicated by its colour [12], and it is thus proposed that the rate of oxygen-sulphur site exchange depends on the rate of arrival of bulk defects at the surface. It has been pointed out that this behaviour is of considerable interest as regards the creation of catalysts resistant to sulphur poisoning. Defects due to both oxygen vacancies and titanium interstitials are present in reduced surfaces and in the temperature regime 400–700 K it is thought that both types of defects are mobile [16]. However, density

functional theory calculations favour migration of bulk oxygen vacancies over the migration of titanium interstitials [14].

First principle molecular dynamics simulations recently published by Langel [15] suggest an alternative mechanism for removal of bridging oxygen. At room temperature sulphur on 5-fold titanium atoms are not found to be stable, and rapidly react with surface oxygens to form SO species which may desorb. The limited cell size used in these calculations does not allow modeling of defect migration from the bulk, so it is not possible from this work to identify the relative importance of this mechanism. However high-resolution photoemission of a surface after adsorption of sulphur at 300 K shows only a small minority of $SO_x$ species, and temperature programed desorption indicates that only S and $S_2$ species are desorbed [14]. These observations would be consistent with this mechanism for the removal of bridging oxygen only if SO desorbs rapidly so it is not detected. That this happens to a significant degree can be ruled out by the absence of a significant $Ti^{3+}$ shoulder to the Ti $2p_{3/2}$ peak on adsorption of sulphur at room temperature [14]. It is thus reasonable to suppose that Langel identifies a minority mechanism.

Returning to the $(3\times1)$-S phase which is the subject of this chapter; whilst the proposed model (figure 6.1) is intuitively reasonable, a number of aspects of the structure have not been rigorously determined. Whilst the binding energy of the S 2p XPS peak is a strong indication that sulphur bonds to titanium, and on the basis of STM, it is reasonable to place sulphur on the rows of 6-fold co-ordinated titaniums rows, there is as yet no evidence for the registry of sulphur atoms in

the [001] direction. The $Ti^{3+}$ peak is attributed to under-coordinated titanium atoms arising from missing oxygen atoms, however it is not possible to rigorously determine the occupancy of bridging oxygens from this observation. Moreover, Langel [15] has demonstrated the stability of models where one or no bridging oxygen per unit cell are present. Clearly a rigorous structural probe such as surface X-ray diffraction (SXRD) is necessary to fully elucidate the geometry of the surface in this case. In addition such a study can be expected to yield precise values for any adsorbate-induced restructuring of the substrate.

## 6.2 Experimental details

Surface X-ray diffraction measurements were undertaken at beamline 9.4 [17] of the Synchrotron Radiation Source, Daresbury, employing the ultra high vacuum endstation INGRID. A full description of the beamline and instrumentation are given in chapter 2. A $TiO_2$ (110) single crystal was prepared by cycles of bombardment with 1 keV $Ar^+$ ions and annealing to approximately 1000 K in UHV until partial reduction of the bulk was detectable by a change in sample colour from yellow to dark blue. The presence of a clean well ordered (1×1) surface was confirmed with LEED, and Auger electron spectroscopy (AES). The clean surface, heated to approximately 570 K, was exposed to a beam of $S_2$ produced by the sulphur source described in chapter 4, operated at a temperature of 480 K and a driving voltage of 0.2 V. Under these circumstances an electrolysis current of approximately 8 mA was generated, and it was found that a dosing time of

approximately one minute was adequate to generate a well ordered (3×1) LEED pattern across the surface.

For the SXRD measurements, INGRID was coupled to a five-circle diffractometer, equipped with an additional manual sixth circle, which almost doubles the amount of accessible reciprocal space in the out-of-plane direction [18]. An X-ray wavelength of 0.9 Å was selected to maximise the available reciprocal space, whilst maintaining a usable photon flux. Data were accumulated using rocking scans, in which the sample was rotated about its surface normal while the scattered X-ray intensity was recorded with a cryogenically cooled, single element, germanium detector. Such scans were performed for a given integer $(h, k)$ as a function of $l$, providing profiles of scattered intensity versus perpendicular momentum transfer — crystal truncation rods (CTRs). Also in-plane rocking scans were acquired at both integer and appropriate fractional $(h, k)$ points, using small incidence and exit angles for the X-rays to give small values of perpendicular momentum transfer ($l = 0.3$). All data were recorded with the substrate at room temperature. During X-ray measurements, surface integrity was monitored by repeatedly measuring the $(h, k, l) = (3, 1, 0.3)$ and $(0, 1, 1.8)$ reflections. After completion of X-ray measurements, the integrity of the surface was confirmed with LEED and AES.

The resulting scans were integrated and corrected for effective sample area, X-ray beam polarisation and Lorentz factor to give structure factor amplitudes. Wherever possible, one or more symmetry-equivalent reflections were recorded and equivalent structure factors were averaged together to give the final data set.

The variation between equivalent data points was used to estimate the systematic error, which at $\sim \pm 9\%$ is the dominant error in the data set. The data are indexed with reference to the (1×1) unit cell, defined such that $\mathbf{a_1}$ and $\mathbf{a_2}$ are orthogonal in the plane of the (110) surface, in the [$\bar{1}$10] and [001] directions, respectively, with $\mathbf{a_3}$ perpendicular to the surface in the [110] direction. The magnitudes of the vectors are $a_1 = a_3 = 6.495$ Å and $a_2 = 2.958$ Å. Reciprocal space axes $h, k$ and $l$ are parallel to $\mathbf{a_1}$,$\mathbf{a_2}$ and $\mathbf{a_3}$ respectively. Hence integer $h, k$ corresponds to crystal truncation rods, and $h = integer$ , $k = \frac{1}{3}, \frac{2}{3}, \frac{4}{3}, \frac{5}{3} \ldots$ corresponds to "fractional order" data.

## 6.3 Results

The data consists of 168 symmetry inequivalent reflections including three CTRs $(h, k) = (0, 1)(0, 2)(1, 1)$ and an in-plane data set of 44 points up to $h_{max} = 9$ and $k_{max} = 4$. Crystal truncation rod data is displayed in figure 6.2 and in-plane data in figure 6.3. Despite measuring some fractional order points over periods in the region of five hours, no fractional order peaks could be resolved above the baseline noise of the scan.

### 6.3.1 Adsorption site

The first stage of analysis was concerned with determining the sulphur adsorption site. The four possible high symmetry adsorption sites were considered; atop

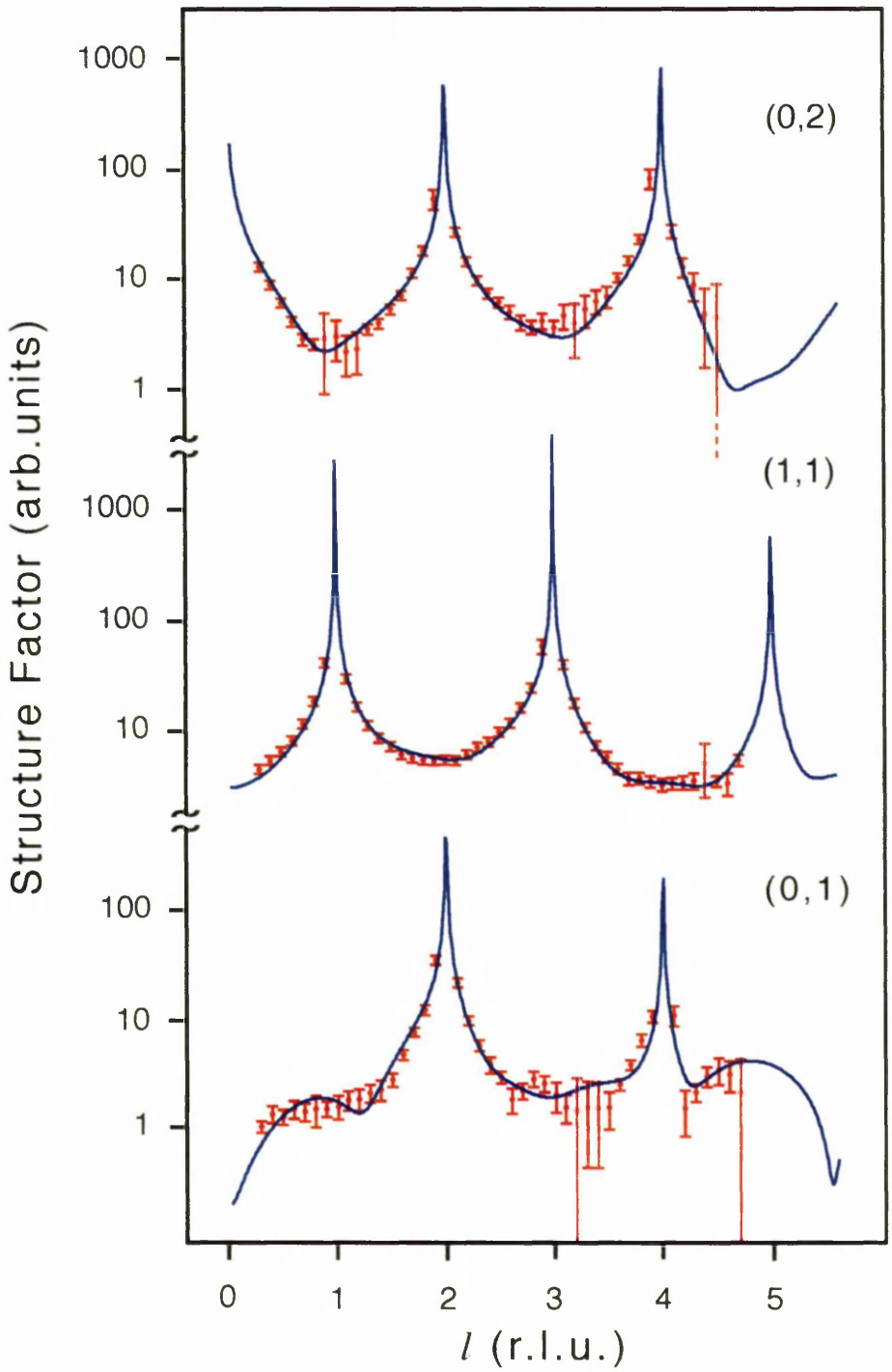


Figure 6.2: Comparison of crystal truncation rod data and calculated best fit model data. Structure factors (F) are given in arbitrary units, out-of-plane momentum transfer ($l$) is given in reciprocal lattice units. Experimental data is plotted in red with error bars, calculated data is shown as a continuous blue line. The truncated error bars at (0,2,4.5),(0,1,3.2) and (0,1,4.7) indicate a lower limit that extends to zero.

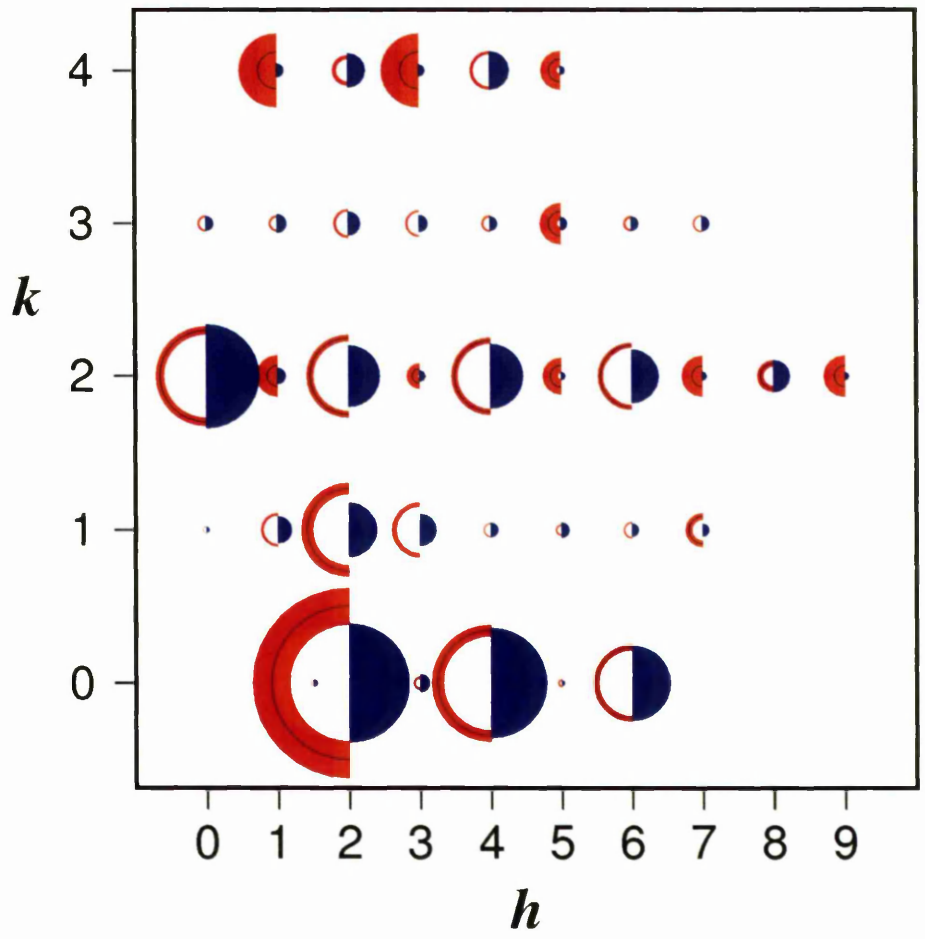


Figure 6.3: Reciprocal space diagram of in-plane structure factors measured at $l = 0.3$. No fractional order data points are shown. Calculated structure factors are represented by filled blue semi-circles with radius proportional to the structure factor. Experimental data is represented by a red arc whose inner and outer radii represent the lower and upper error bars. For $F_{h,k,0.3} > 0.7$ the measured structure factor is represented as a thin black arc. The data point at $(h, k) = (1, 0)$ has been displaced to $(h, k) = (1, 0.5)$ for clarity.

or bridging titanium atoms that are 5-fold or 6-fold co-ordinated in the clean, stoichiometric surface, as shown in figure 6.4. In the clean stoichiometric surface the 5-fold titaniums fall between the bridging oxygen rows, and the 6-fold titaniums under the bridging oxygen rows. Sulphur occupancies from one to three per (3×1) unit cell, were considered. The occupancy of bridging oxygens was also considered, as it will be a key parameter for any models where sulphur is thought to co-ordinate to 6-fold titanium atoms, and first principles molecular dynamics calculations suggest that sulphur adsorption bridging 6-fold titaniums is equally stable with zero or one oxygens per unit cell [15]. Initially these models were compared with only the in-plane portion of the data, which will be largely insensitive to any out-of-plane distances. Table 6.1 shows $\chi^2_\nu$ for these cases without any attempt at optimising geometric parameters. To minimise additional assumptions about the structure, and to seek general trends in the data, sulphur occupancies of between 1 and 3 atoms per unit cell and bridging oxygen occupancies between stoichiometric (3 per unit cell) and no oxygens were considered. It is noted that some of the implied surface models are rather implausible, and some could only be formed if S–O species were permitted.

For any given model and given oxygen occupancy, it can be seen that S = 2 leads to a significantly larger $\chi^2_\nu$ than S = 1, and likewise $\chi^2_\nu$ for S = 3 is significantly larger than for S = 2. This strongly indicates that the overlayer consists of a single sulphur atom per unit cell. Analysis continued by optimising in-plane motions that retained *p2mm* symmetry for models with one sulphur per unit cell. Table 6.2 shows optimised $\chi^2_\nu$ for these models. In the case where one sulphur

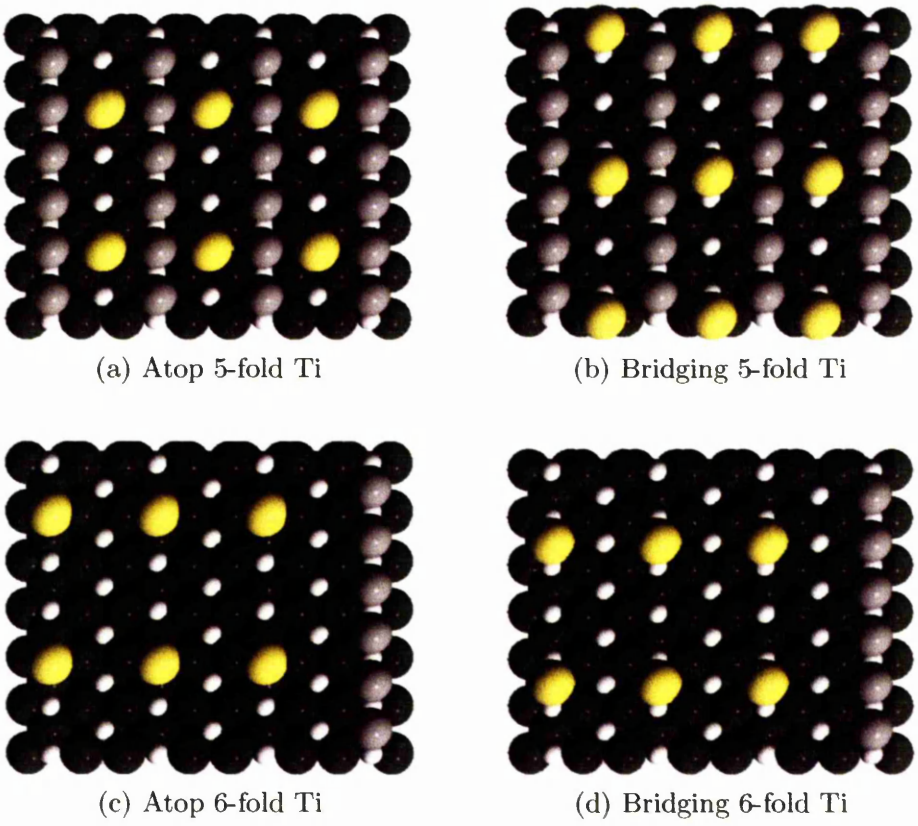

(a) Atop 5-fold Ti

(b) Bridging 5-fold Ti

(c) Atop 6-fold Ti

(d) Bridging 6-fold Ti

Figure 6.4: Ball models of the four high symmetry sulphur adsorption sites considered. Sulphur is represented by yellow spheres, oxygen by black spheres, bridging oxygen by grey spheres and titanium by white spheres. In the cases where sulphur is adsorbed on 6-fold titanium atoms, bridging oxygens have been removed for clarity, but a compete bridging oxygen row is retained at the right of the model.

| | S = 1 | | | |
|---|---|---|---|---|
| | Ox = 0 | Ox = 1 | Ox = 2 | Ox = 3 |
| Atop 5f Ti | 25.41 | 16.01 | 10.86 | 9.92 |
| Bridge 5f Ti | 31.60 | 17.27 | 9.73 | 8.37 |
| Atop 6f Ti | 32.19 | 26.03 | 25.83 | 32.10 |
| Bridge 6f Ti | 8.88 | 12.26 | 18.81 | 30.65 |
| | S = 2 | | | |
| | Ox = 0 | Ox = 1 | Ox = 2 | Ox = 3 |
| Atop 5f Ti | 55.52 | 40.23 | 29.98 | 25.89 |
| Bridge 5f Ti | 77.61 | 53.64 | 34.77 | 22.50 |
| Atop 6f Ti | 75.50 | 69.64 | 70.52 | 78.17 |
| Bridge 6f Ti | 18.49 | 30.68 | 49.17 | 74.33 |
| | S = 3 | | | |
| | Ox = 0 | Ox = 1 | Ox = 2 | Ox = 3 |
| Atop 5f Ti | 107.35 | 88.36 | 75.87 | 69.64 |
| Bridge 5f Ti | 151.93 | 116.02 | 86.47 | 62.12 |
| Atop 6f Ti | 149.08 | 144.16 | 146.11 | 154.94 |
| Bridge 6f Ti | 50.74 | 75.91 | 107.37 | 144.52 |

Table 6.1: Quality of fit ($\chi^2_\nu$) to the in-plane portion of the data for sulphur adsorption in different high symmetry sites without any geometric optimisation. Sulphur occupancies of between 1 and 3 atoms per $(3\times1)$ unit cell were considered, and are denoted S = 1, 2, 3. Bridging oxygen occupancies between stoichiometric (3 per unit cell) and no oxygens were considered, and are denoted Ox = 0, 1, 2, 3

| | Ox = 0 | Ox = 1 | Ox = 2 | Ox = 3 |
|---|---|---|---|---|
| Atop 5f Ti | 10.75 | 7.01 | 4.84 | 4.52 |
| Bridge 5f Ti | 12.09 | 8.67 | 6.35 | 6.47 |
| Atop 6f Ti | 11.44 | 13.71 | 18.44 | 29.49 |
| Bridge 6f Ti | 5.83 | 9.90$^{\dagger}$ | 17.92 | - |

Table 6.2: Quality of fit ($\chi^2_\nu$) to in-plane portion of the data with optimised in-plane geometric parameters; $^{\dagger}$ indicates the case where the symmetry of the surface is lowered to $p1m1$

is adsorbed bridging 6-fold titanium atoms, with one bridging oxygen retained ($^{\dagger}$), the symmetry of the surface is *a priori* lowered to $p1m1$, indicating that additional motions consistent with the lower symmetry need to be considered. However exhaustive investigation found no significant improvement in $\chi^2_\nu$ when these motions were allowed.

Ideally it would be possible to clearly determine the adsorption site and bridging oxygen occupancy from the X-ray diffraction data alone, however a number of possible models are favoured. STM data [6] for a surface presenting a clear (3×1) LEED pattern show a predominance of bright moieties on the 6-fold titanium rows suggesting the choice of models could be constrained to those where sulphur falls on the 6-fold titanium rows i.e. atop or bridging 6-fold titanium atoms. If this is the case then adsorption bridging 6-fold titanium is strongly indicated, and models without any bridging oxygens are favoured, in agreement with photoemission results. This is identical to the model proposed by Diebold on the basis of STM and photoemission data [6].

For sulphur bridging 6-fold titanium atoms, first principle molecular dynamics simulations suggest that configurations with zero or one oxygen per (3×1) unit cell will both be stable [15]. On changing from zero bridging oxygens per unit cell to one per unit cell there is an increase in $\chi^2_\nu$ of nearly 70%, whilst this may be interpreted as indicating that only the surface without bridging oxygen is present, it may also indicate that a mixture of these two surfaces is present. This possibility was investigated by fitting the in-plane data with bridging oxygen occupancies between zero and one per (3×1) unit cell, both with geometric parameters fixed, and optimised. Figure 6.5 shows plots of $\chi^2_\nu$ against oxygen occupancy, and clearly demonstrates that even small increases in occupancy above zero lead to an increase in $\chi^2_\nu$, indicating that the ordered portion of the surface is completely denuded of bridging oxygen.

It is possible that the similarity in $\chi^2_\nu$ between some of these models may arise from the absence of out-of-plane data. However repeating geometric optimisation with the full data set (including out-of-plane data) for models with $\chi^2_\nu < 7.0$ did not allow any clearer distinction between surface models.

### 6.3.2 Optimised surface model

For the preferred model, both in-plane and out-of-plane geometric parameters were optimised, geometric parameters were chosen which maintained the *p2mm* symmetry of the surface. Figure 6.6 on page 132 shows a schematic of the surface with atom labels. Care was taken to consider the different combinations of

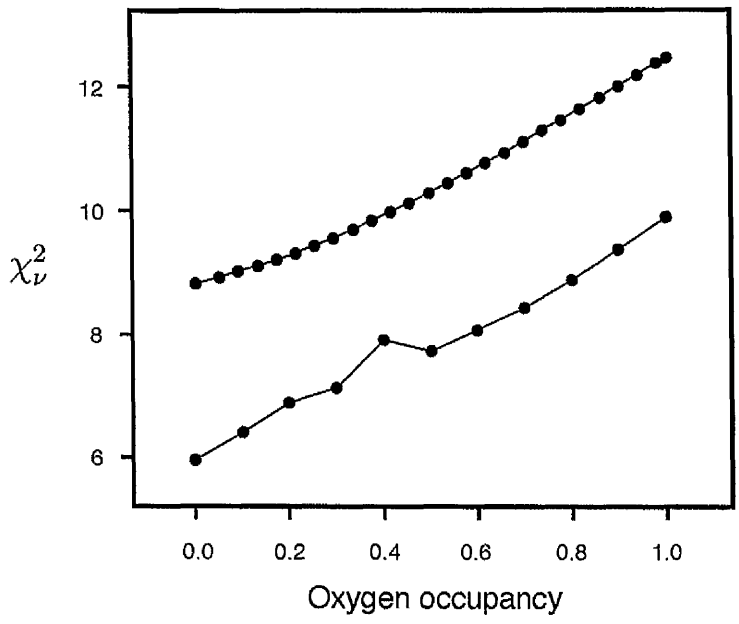


Figure 6.5: Value of $\chi^2_\nu$ for oxygen occupancies between zero and one per $(3\times1)$ unit cell, with one sulphur atom per unit cell, bridging 6-fold titanium atoms. The upper trace represents calculations with atoms kept at bulk positions; the lower trace represents calculations where the surface geometry has been optimised.

motions that maintain *p2mm* symmetry, and to eliminate motions that did not improve $\chi^2_\nu$. A best fit value $\chi^2_\nu = 1.83$ was obtained. Optimised parameters are given in table 6.3. For simplicity, motions are described as being in **x** or **y** directions (in-plane) and **z** (out-of-plane). The **x** direction is parallel to $[\bar{1}10]$; the **y** direction is parallel to [001], and the **z** direction is parallel to [110]. A positive shift denotes a motion out of the surface in the the **z** direction, or towards the center of the cell in the **x** and **y** directions. The best value of $\chi^2_\nu$ was found when constraining some symmetry inequivalent atoms to have the same magnitude of motion in a given direction, for example all the 5-fold titaniums move by the same amount in the **z** direction. In the following, layers of the selvedge are identified by a number, layer 1 ($L_1$) refers to the topmost complete layer of the substrate

(not the layer that would contain bridging oxygen atoms), layer 2 ($L_2$) is the oxygen only layer beneath this etc.

Allowing oxygen motions in the fourth layer, or motions deeper in the selvedge did not lead to improved $\chi^2_\nu$. Non-geometric parameters considered included Debye-Waller (thermal vibration) factors, surface roughness and proportion of clean, relaxed surface. It was found that adding the latter two parameters did not meaningfully improve the quality of fit. As well as an isotropic Debye-Waller factor for the adsorbed sulphur, separate isotropic Debye-Waller factors for titanium and oxygen atoms in layer 1 were employed; allowing Debye-Waller factors to vary from bulk values for deeper layers did not lead to an improved quality of fit. Likewise allowing additional Debye-Waller factors for the top layer did not lead to an improved quality of fit. Experimental and theoretical crystal truncation rods are compared in figure 6.2, and experimental and theoretical in-plane data in figure 6.3.

The absence of fractional order data means that in effect atoms, and their associated motions can be moved an arbitrary number of $(1\times1)$ unit cells in the [001] direction. In practice this means that only the magnitude of motions in the [001] direction are known and not whether the motion is directed towards or away from the center of the cell, this is discussed in detail in appendix 1. Examining the best fit model parameters it was found in the cases of Ti(3)**y**,O(3)**y** and O(5)**y** that only one direction of motion gave rise to physically plausible bond lengths. However both positive and negative values of Ti(2)**y**,Ti(6)**y**,Ti(7)**y** and O(2)**y** give rise to physically plausible bond lengths, so the length of some associated

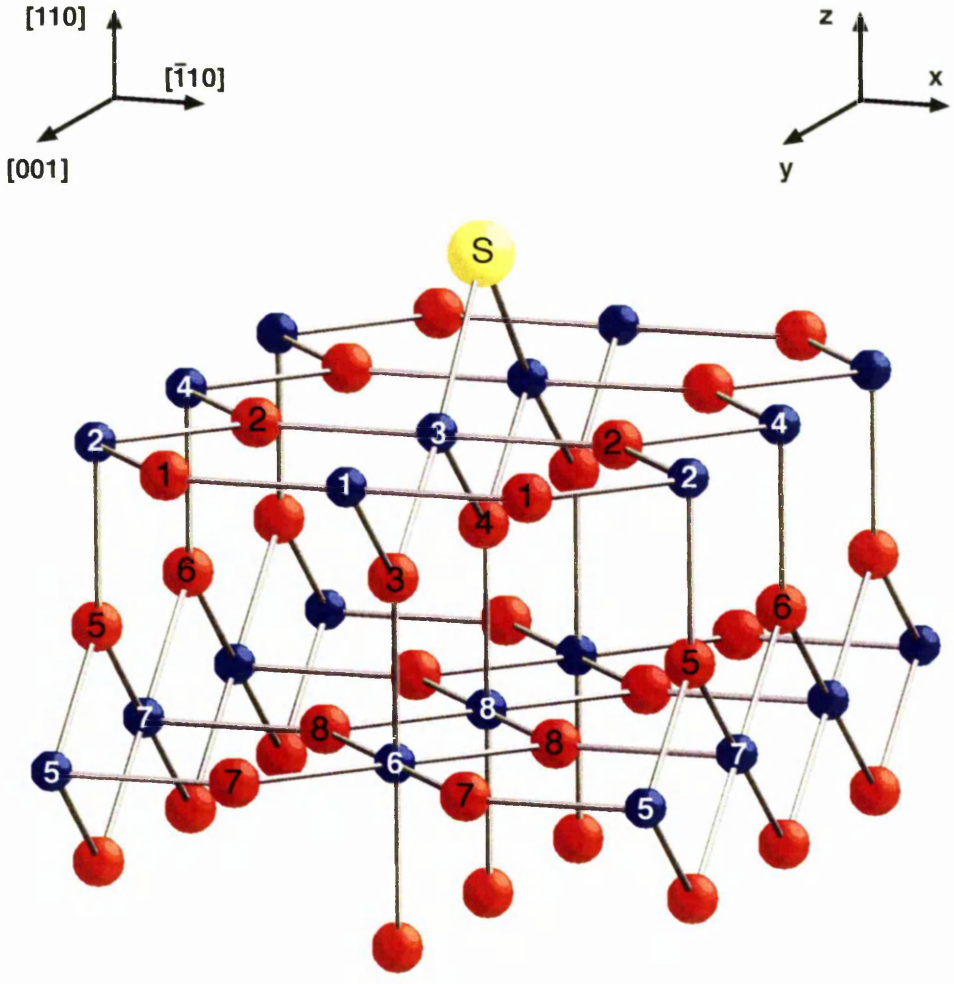


Figure 6.6: Schematic of the surface model of $TiO_2$(110)(3×1)-S showing the atom labels. Sulphur is represented by a yellow sphere, oxygen by red spheres, and titanium by blue spheres.

| Atom motion | Displacement (Å) | | |
|---|---|---|---|
| | $TiO_2$(110)(3×1)-S | $TiO_2$(110)(1×1) | |
| | Present work | SXRD [19] | LEED-IV [20] |
| Ti (1) **z** | 0.12 ± 0.02 | 0.25 ± 0.01 | 0.25 ± 0.03 |
| Ti (2) **y** | ±0.13 ± 0.01 | — | — |
| Ti (2) **z** | 0.05 ± 0.01 | -0.11 ± 0.01 | -0.19 ± 0.03 |
| Ti (3) **y** | -0.38 ± 0.01 | — | — |
| Ti (3) **z** | -0.08 ± 0.02 | 0.25 ± 0.01 | 0.25 ± 0.03 |
| Ti (4) **z** = Ti (2) **z** | | — | — |
| Ti (5) **z** | 0.27 ± 0.02 | -0.08 ± 0.01 | -0.09 ± 0.07 |
| Ti (6) **y** | ±0.06 ± 0.02 | — | — |
| Ti (6) **z** | -0.04 ± 0.01 | 0.19 ± 0.01 | 0.14 ± 0.05 |
| Ti (7) **y** | ±0.01 ± 0.05 | — | — |
| Ti (7) **z** | -0.01 ± 0.01 | -0.08 ± 0.01 | -0.09 ± 0.07 |
| Ti (8) **z** = Ti (6) **z** | | — | — |
| O (1) **x** | -0.26 ± 0.04 | 0.01 ± 0.05 | -0.17 ± 0.15 |
| O (1) **z** | 0.02 ± 0.01 | 0.17 ± 0.03 | 0.27 ± 0.08 |
| O (2) **x** | 0.21 ± 0.02 | 0.01 ± 0.05 | -0.17 ± 0.15 |
| O (2) **y** | ±0.13 ± 0.02 | — | — |
| O (2) **z** = O (1) **z** | | — | — |
| O (3) **y** | -0.26 ± 0.02 | — | — |
| O (3) **z** | -0.20 ± 0.03 | 0.07 ± 0.04 | 0.06 ± 0.10 |
| O (4) **z** | 0.32 ± 0.11 | 0.07 ± 0.04 | 0.06 ± 0.10 |
| O (5) **y** | 0.28 ± 0.03 | — | — |
| O (5) **z** | 0.01 ± 0.02 | 0.00 ± 0.03 | 0.00 ± 0.08 |
| O (6) **z** = O (5) **z** | | — | — |
| S $\mathbf{z}_{top\ layer}$ | 1.92 ± 0.02 | — | — |
| S $\mathbf{z}_{bridging\ oxygen}$ | 0.56 ± 0.02 | — | — |
| Thermal vibration | (Å$^2$) | | |
| B(Ti top layer) | 0.70 ± 0.10 | | |
| B(Sulphur) | 0.32 ± 0.51 | | |
| B(O top layer) | 0.01 ± 0.23 | | |

Table 6.3: Atomic displacements from bulk structure, compared with reported shifts for $TiO_2$(110)(1×1). Atom labels refer to figure 6.6, the directions of the motions are described in the text. The S position is given as a height above bulk terminated $L_1$ (S $\mathbf{z}_{top\ layer}$), and also as a shift from the bridging oxygen position (S $\mathbf{z}_{bridging\ oxygen}$).

bonds take more than one value. The large number of bonds in the model meant particular care was required to identify unphysical bonds, the physical plausibility of bonds was assessed by comparison with a comprehensive databases of inorganic and organic crystal structures [21]. A list of symmetry inequivalent bond lengths is given in table 6.4.

## 6.4 Discussion

Taken in concert with existing STM and photoemission data [6], the sulphur adsorption site can convincingly be assigned to a position bridging 6-fold co-ordinated titaniums. Whilst oxygen is the weakest scattering element on the surface, there is a clear dependence of $\chi^2_\nu$ on the bridging oxygen occupancy (table 6.2, figure 6.5), indicating the total absence of bridging oxygen. If the model proposed by Langel [15] where one bridging oxygen is retained were present, then it is expected that substrate motions consistent with $p1m1$ symmetry would be found; hence the observation that symmetry lowering motions are not favoured also militates against the case where one oxygen is retained. Taking these various considerations together, it is clear that the present work favours adsorption of sulphur bridging 6-fold titanium atoms with all bridging oxygen atoms lost on formation of the $(3\times1)$ overlayer. This is consistent with the model proposed by Diebold [6], and which first principle molecular dynamics simulations show to be thermodynamically stable [15].

| Layer | Atom pair | Bond length (Å) | | | | | $TiO_2$(110)(1×1) | |
|---|---|---|---|---|---|---|---|---|
| | | | | | | | SXRD [19] | LEED-IV [20] |
| S - $L_1$ | S(1) – Ti(3) | 2.74 | | | ± | 0.02 | — | — |
| $L_1$ | Ti(1) – O(1) | 2.24 | | | ± | 0.04 | 1.98 | 2.16 |
| | Ti(2) – O(1) | 1.68 | 1.90 | | ± | 0.02 | 1.97 | 1.89 |
| | Ti(2) – O(2) | 1.90 | 2.08 | 2.28 | ± | 0.02 | 1.97 | 1.89 |
| | Ti(3) – O(2) | 1.80 | 1.85 | | ± | 0.02 | 1.98 | 2.16 |
| | Ti(4) – O(2) | 2.00 | 2.19 | | ± | 0.02 | 1.97 | 1.89 |
| $L_1$ - $L_2$ | Ti(1) – O(3) | 2.00 | | | ± | 0.03 | 2.06 | 2.07 |
| | Ti(3) – O(3) | 1.93 | | | ± | 0.03 | 2.06 | 2.07 |
| | Ti(3) – O(4) | 2.05 | | | ± | 0.05 | 2.06 | 2.07 |
| $L_1$ - $L_3$ | Ti(2) – O(5) | 2.03 | 2.06 | | ± | 0.02 | 1.88 | 1.80 |
| | Ti(4) – O(6) | 2.02 | | | ± | 0.02 | 1.88 | 1.80 |
| $L_2$ - $L_4$ | Ti(6) – O(3) | 1.83 | 1.85 | | ± | 0.03 | 1.87 | 1.91 |
| | Ti(8) – O(4) | 2.34 | | | ± | 0.11 | 1.87 | 1.91 |
| $L_3$ - $L_4$ | Ti(5) – O(5) | 2.03 | | | ± | 0.03 | 2.00 | 2.00 |
| | Ti(7) – O(5) | 1.75 | 1.76 | | ± | 0.04 | 2.00 | 2.00 |
| | Ti(7) – O(6) | 1.96 | 1.97 | | ± | 0.04 | 2.00 | 2.00 |
| $L_4$ | Ti(5) – O(7) | 2.00 | | | ± | 0.00 | 1.94 | 2.06 |
| | Ti(6) – O(7) | 1.90 | 2.00 | | ± | 0.01 | 1.98 | 1.90 |
| | Ti(6) – O(8) | 1.90 | 1.99 | | ± | 0.01 | 1.98 | 1.90 |
| | Ti(7) – O(8) | 1.98 | | | ± | 0.00 | 1.94 | 2.06 |
| | Ti(8) – O(8) | 1.95 | | | ± | 0.00 | 1.98 | 1.90 |
| $L_5$ - $L_{6,7}$ | Ti(5) – O(9) | 2.13 | | | ± | 0.01 | 1.89 | 1.89 |
| | Ti(6) – O(11) | 1.95 | | | ± | 0.01 | 2.17 | 2.12 |
| | Ti(7) – O(9) | 1.93 | | | ± | 0.04 | 1.89 | 1.89 |
| | Ti(7) – O(10) | 1.95 | | | ± | 0.04 | 1.89 | 1.89 |
| | Ti(8) – O(12) | 1.95 | | | ± | 0.01 | 2.17 | 2.12 |

Table 6.4: Inequivalent best fit bond lengths obtained in the present work. Bond lengths obtained in studies of the clean surface are given for comparison; bulk bond lengths take values of 1.94 Å and 1.99 Å. The origin of multiple bond lengths is discussed in the main text.

Despite the absence of fractional order data, a significant amount of meaningful structural information has been determined. The formation of the (3×1) sulphur overlayer gives rise to significant substrate motions that are not present on the clean surface. If a reconstruction is taken to be substrate motions that change the periodicity of the substrate such that the new surface symmetry would be apparent without the adsorbate, then SXRD reveals an adsorbate-induced reconstruction of the substrate extending several layers into the selvedge. This contrasts with the structural study of Ni(110)c(2×2)-CN presented in chapter 5 where, despite the presence of a LEED pattern with sharp overlayer spots, no reconstruction of the surface was found.

Motions not present on the clean surface include shifts in the **y** direction in the first three substrate layers; the 6-fold co-ordinated titaniums Ti(3) move away from the adsorbed sulphur by 0.38 Å, the co-ordinating oxygens in the second layer, O(3), move in the same direction but by only 0.26 Å, O(5) in the third layer moves towards the center of the cell by 0.28 Å. Out-of-plane motions are generally reduced compared to values obtained for the clean surface [19, 20], but a strong rumpling of the second (oxygen) layer with a magnitude of approximately ±0.25 Å relative to the clean positions is found, as is a 0.27 Å outward relaxation of Ti(5) in the fourth (mixed) layer.

The most striking feature of the optimised surface model is the substantial **y** motion (0.38 Å) of the 6-fold co-ordinated titaniums, Ti(3), away from the adsorbed sulphur, accompanied by a small inward **z** motion relative to the bulk terminated surface. It is reasonable to suppose that the motion of Ti(3) is steric

in origin — the replacement of a bridging oxygen atom with a significantly larger sulphur causes Ti(3) to move away from the adsorbate. The ionic radii of $S^{2-}$ and $O^{2-}$ are 1.84 Å and 1.32 Å, respectively [22]. Also it may be supposed that the motion of Ti(3) away from the sulphur is the cause of the **y** motion of O(3), and the rumpling of second layer oxygens O(3) and O(4), which both co-ordinate to Ti(3). The movement of Ti(3) away from the center of the cell allows O(4) to relax outward, whereas O(3) moves downward and away from the center of the cell. It is noted that this motion keeps the length of bonds between the first and second layer close to bulk values (1.94 & 1.99 Å) and clean surface values (1.93 – 2.05 Å), but the outward motion of O(3), and modest motion of Ti(8) leads to a considerable expansion of Ti(8) – O(4) to $2.34 \pm 0.11$ Å.

The motion of Ti(3) away from the adsorbate is accompanied by an inward **x** motion of the co-ordinated in-plane oxygen, O(2), by 0.21 Å, and a **y** motion with undetermined sign; O(1) also moves in the **x** direction with a similar magnitude, but away from the center of the cell. The **z** motions of O(1) and O(2) away from bulk positions are both small, representing a considerable contraction relative to the clean surface. The 6-fold titanium atoms in the top layer both move inward relative to the clean surface; Ti(1) moves out from its bulk position by 0.12 Å, whereas Ti(3) moves inward from its bulk position by 0.08 Å. The best fit model includes constraining the **z** motions of all 5-fold titanium atoms in the top layer to the same value. This motion takes a modest value of 0.05 Å, which constitutes an outward motion relative to the clean surface. The ambiguity in bond lengths introduced by the absence of fractional order data mean it is not always possible

to discern a meaningful change in bond lengths as compared with the clean or bulk terminated values. This is a particular difficulty in the top layer, however it is can be seen that the bond Ti(1) – O(1) expands (2.24 Å) whereas the bond Ti(3) – O(2) contracts (1.80 or 1.85 Å), relative to the bulk terminated and clean surface values.

The motion of O(5) in the **y** direction and the outward motion of the co-ordinated Ti(5) would seem to be connected — the combination of motions is such that the length of the Ti(5) – O(5) bond stays near bulk and clean values (2.03 Å) — however the origin of this motion is unclear, the motion of co-ordinating atoms being modest. The bond Ti(7) – O(5) is considerably reduced to approximately 1.75 Å due to the **y** motion of O(5) whereas although Ti(5) moves out sharply, the bond Ti(5) – O(7) increases to only 2.00 Å. The length of bonds connecting the first and third layers increase a small amount from bulk values and fall in a narrow range (2.02–2.06 Å), whereas there is greater variation in the length of bonds connecting the third and fourth layers (1.75–2.03 Å). It is interesting to note that bonds to layers above and below the second (oxygen) layer show similar behaviour. Other than the motions of O(5) in the **y** direction and Ti(5) in the **z** direction, the third (oxygen) and fourth (mixed) layers exhibit only modest perturbations from the bulk structure, other than bonds involving Ti(5), bonds lengths in the fourth layer and between the fourth layer and lower layers stay very close to bulk values.

If experimental errors are considered, the magnitude of atomic shifts in the out-of-plane direction fall within the range of values already reported for the clean

surface [19, 20, 23]. In-plane motions exceed those for the clean surface by no more than 0.1 Å and fall well within the range reported for the copper covered $TiO_2(110)$ surface [24]. Titanium-oxygen bond lengths fall between 1.68 Å and 2.28 Å with an outlying value of $2.34 \pm 0.11$ Å, arising from the large but ill defined oxygen relaxation beneath the adsorbed sulphur. The shortest distance constitutes a contraction of 13% and the longer distances both constitute an expansion of 18%, as compared with bulk values. Bulk bond lengths take values of 1.94 Å and 1.99 Å, and values between 1.80 Å and 2.17 Å are reported in recent structural studies of the clean surface [19, 20]. Ti–O bond lengths in the present case fall within the range of values reported in a large databases of organic and inorganic bulk structures [21], the S–Ti distance of 2.74 Å is somewhat larger than S–Ti distance reported for simple, binary inorganic compounds (2.26 – 2.61 Å) [25] but a number of studies of complex metal-titanium oxysulphide structures report similar bond lengths [26–29].

As in any structural studies that require fitting of a non-trivial model to a set of experimental data, there is a risk that the optimisation will become stuck in a local minima on the $\chi^2_\nu$ hypersurface, and not reach the true best fit to the data. It is also possible that there will not be a single unique surface model that gives a distinguishably better $\chi^2_\nu$ than other models. These problems will be more acute if, as with the present data, a relatively flat $\chi^2_\nu$ hypersurface is expected. Whilst it has been difficult to discriminate between different surface models using the present data set, no physically plausible alternative minima have been found when sulphur is constrained to the present adsorption site. Considerable care

has been exercised to avoid local minima (as described in section 2.4.3) but as with all such structural studies there remains a risk of unsuspected minima with similar or smaller values of $\chi^2_\nu$ to the known best fit.

Calculations employing the best fit model indicate that at least some fractional order diffraction peaks should have been large enough to be detectable. Here a possible explanation for their absence is considered. Whilst it is relatively easy to form very large domains of clean $TiO_2$(110), giving rise to very sharp diffraction peaks, more diffuse overlayer spots were observed in the LEED pattern of the sulphur covered surface. One possible cause of this disorder is the formation of many small domains of the sulphur overlayer on each large substrate domain. If a vector $\mathbf{I}$ connecting equivalent atoms in two domains is expressed as multiples ($l_1$ and $l_2$) of in-plane substrate unit cell vectors $\mathbf{a_1}$ and $\mathbf{a_2}$ thus:

$$\mathbf{I} = l_1\mathbf{a_1} + l_2\mathbf{a_2} \tag{6.1}$$

then the phase shift between domains is given as [30]:

$$\Delta\phi = 2\pi(hl_1 + kl_2) \tag{6.2}$$

In the present case the domains may be shifted by one or more substrate unit cells in the [001] direction, hence:

$$\mathbf{I} = n\mathbf{a_2} \qquad \text{and} \qquad \Delta\phi = 2\pi(kn) \tag{6.3}$$

where $n = 1, 2, 3, 4 \ldots$. It can thus be seen that at integer $k$ the term in brackets is always an integer, hence the out of phase domains give rise to no phase shift at CTR positions. For $k = \frac{1}{3}, \frac{2}{3}, \frac{4}{3}, \frac{5}{3} \ldots$ the phase shift will take a value of $\pm\frac{2\pi}{3}$.

This phase shift is expected to broaden and reduce the intensity of fractional order peaks relative to the integer order peaks, hindering their detection [31].

In contrast to the Ni(110)c(2×2)-CN surface investigated in chapter 5, which has been the subject of a number of different structural probes as well as theoretical investigations, the work presented in this chapter is the first rigorously quantitative attempt to investigate the structure of the (3×1)-S surface. Ideally future work will lead to a similarly convincing consensus between models obtained with different experimental methods and those determined theoretically.

An obvious extension of the present work would be to repeat the measurements at a third generation synchrotron source, however a LEED-IV study would be a valuable complement to the present work. Not only is it likely to give a convincing determination of adsorption site, but as data will be collected in back-scattering geometries, where out-of-plane momentum transfer dominates, it should allow for more accurate determination of small out-of-plane motions. As well as revealing small motions deeper in the selvedge, small rumplings in the cases where symmetry inequivalent atoms have been constrained to have the same out-of-plane motion may also be found. High quality first principles *ab initio* calculations employing a full (3×1) unit cell should give values for atom motions as well as give some insight into the electronic structure of the surface; however it is noted that the comparatively large unit cell means such calculations consume considerable computational resources [32].

Looking further into the future, the other well ordered structures formed by

sulphur on $TiO_2$(110) would be interesting candidates for structural investigations which would rigorously test the proposed models for the (3×3)-S and (4×1)-S surfaces, and investigate the significant restructuring that can be expected from surfaces denuded of bridging oxygen, and with sulfur replacing oxygens in the top layer of the substrate.

## 6.5 Summary

Taken in concert with existing STM and photoemission data [6] it has been shown that on formation of a (3×1)-S overlayer on $TiO_2$(110), by dosing sulphur onto a clean (1×1) surface at 570 K, sulphur adsorbs in a position bridging 6-fold titanium atoms, and all bridging oxygens are lost. Sulphur adsorption gives rise to significant restructuring of the substrate which has been detected as deep as the fourth layer of the selvedge. The replacement of a bridging oxygen atom with sulphur is thought to give rise to a significant motion of co-ordinated 6-fold titanium atoms away from the adsorbate, along with a concomitant rumpling of the second (oxygen) substrate layer.

# References


[1] J.A. Rodriguez, S. Chaturvedi, M. Kuhn, and J. Hrbek. *J. Phys. Chem. B*, 102:5511–5519, 1998.

[2] J.A. Rodriguez and J. Hrbek. *Acc. Chem. Res.*, 32:719–728, 1999.

[3] J.G. Speight. *The Chemistry and Technology of Petroleum.* Dekker, 2nd edition, 1991.

[4] J. Oudar and H. Wise, editors. *Deactivation and Poisoning of Catalysts.* Dekker, 1991.

[5] G. Ertl, H. Knözinger, and J. Weitkamp, editors. *Handbook of Heterogeneous Catalysis.* Wiley-VCH, 1997.

[6] E.L.D. Hebenstreit, W. Hebenstreit, and U. Diebold. *Surf. Sci.*, 461:87–97, 2000.

[7] M. Sevignon, M. Macaud, A. Favre-Reguillon, J. Schulz, M. Rocault, R. Faure, M. Vrinat, and M. Lemaire. *Green Chem.*, 7:413–420, 2005.

[8] J.K. Leggett. *Half gone; oil, gas, hot air and the global energy crisis.* Portobello, 2005.

[9] S.H. Wang, B.L. Shen, and L.L. Qu. *Catal. Today*, 98:339–342, 2004.

[10] U. Diebold. *Surf. Sci. Rep.*, 48:53–229, 2003.

[11] E.L.D. Hebenstreit, W. Hebenstreit, and U. Diebold. *Surf. Sci.*, 470:347–360, 2001.

[12] E.L.D. Hebenstreit, W. Hebenstreit, H. Geisler, C.A. Ventrice, P.T. Sprunger, and U. Diebold. *Surf. Sci.*, 486:L467–L474, 2001.

[13] E.L.D. Hebenstreit, W. Hebenstreit, H. Geisler, S.N. Thornburg, C.A. Ventrice, D.A. Hite, P.T. Sprunger, and U. Diebold. *Phys. Rev. B*, 64:115418, 2001.

[14] J.A. Rodriguez, J. Hrbek, Z. Chang, J. Dvorak, T. Jirsak, and A. Maiti. *Phys. Rev. B*, 65:235414, 2002.

[15] W. Langel. *Surf. Sci.*, 600:1884–1890, 2006.

[16] M.A. Henderson. *Surf. Sci.*, 419:174–187, 1999.

[17] C. Norris, M.S. Finney, G.F. Clark, G. Baker, P.R. Moore, and R. Vansilfhout. *Rev. Sci. Instrum.*, 63:1083–1086, 1992.

[18] J.S.G. Taylor, C. Norris, E. Vlieg, M. Lohmeier, and T.S. Turner. *Rev. Sci. Instrum.*, 67:2658–2659, 1996.

[19] G. Cabailh, X. Torrelles, R. Lindsay, O. Bikondoa, I. Joumard, J. Zegenhagen, and G. Thornton. *Phys. Rev. B*, 75:241403, 2007.

[20] R. Lindsay, A. Wander, A. Ernst, B. Montanari, G. Thornton, and N.M. Harrison. *Phys. Rev. Lett.*, 94:246102, 2005.

[21] D.A. Fletcher, R.F. McMeeking, and D.J. Parkin. *J. Chem. Inf. Comp. Sci.*, 36:746–749, 1996.

[22] R.C. Weast, editor. *CRC Handbook of Chemistry and Physics.* CRC Press, 61st edition, 1980-1981.

[23] G. Charlton, P.B. Howes, C.L. Nicklin, P. Steadman, J.S.G. Taylor, C.A. Muryn, S.P. Harte, J. Mercer, R. McGrath, D. Norman, T.S. Turner, and G. Thornton. *Phys. Rev. Lett.*, 78:495–498, 1997.

[24] G. Charlton, P.B. Howes, C.A. Muryn, H. Raza, N. Jones, J.S.G. Taylor, C. Norris, R. McGrath, D. Norman, T.S. Turner, and G. Thornton. *Phys. Rev. B*, 61:16117–16120, 2000.

[25] F.M.R. Engelsma, G.A. Wiegers, F. Jellinek, and B. Vanlaar. *J. Solid State Chem.*, 6:574–582, 1973.

[26] V. Meignen, L. Carlo, A. Lafond, Y. Moelo, C. Guillot-Deudon, and A. Meerschaut. *J. Solid State Chem.*, 177:2810–2817, 2004.

[27] G. Hyett, O.J. Rutt, Z.A. Gal, S.G. Denis, M.A. Hayward, and S.J. Clarke. *J. Am. Chem. Soc.*, 126:1980–1991, 2004.

[28] V. Meignen, A. Lafond, L. Cario, C. Deudon, and A. Meerschaut. *Acta Crystallogr. C*, 59:I63–I64, 2003.

[29] J. A. Cody and J.A. Ibers. *J. Solid State Chem.*, 114:406–412, 1995.

[30] L.J. Clarke. *Surface crystallography - An introduction to low energy electron diffraction.* Wiley-Interscience, 1985.

[31] E. Vlieg, J.F. Van der Veen, S.J. Gurman, C. Norris, and J.E. Macdonald. *Surf. Sci.*, 210:301–321, 1989.

[32] P.J.D. Lindan and B. Nikolaidi. Private communication.

# Chapter 7

# Ordered overlayers of calcium on $TiO_2$(110)-1×1

## 7.1 Introduction

The growth of ultra-thin metal layers on metal oxide substrates has attracted considerable interest, and in particular a remarkably complete body of studies exists for the adsorption of metals on $TiO_2$ substrates — a number of authors have published reviews [1–4]. Alkali and alkaline earth metals are of interest as they are known to significantly alter the surface properties of metal oxides [5]. In contrast to noble metals that tend to stay in metallic states when deposited on metal oxides [3], the higher oxygen affinity of alkali and alkaline earth metals has been seen to lead to the transfer of electrons to the substrate, oxidising the adsorbate [6–9]. The study of these systems is expected to illuminate the design

and understanding of technology as diverse as heterogeneous catalysts [10–13], gas sensors and microelectronic devices [14] and bio-compatible materials [15, 16].

Whilst the adsorption of almost all the alkali metals on $TiO_2$ has been investigated, fewer studies have considered the alkaline earth metals, with such work as has been published concentrating on the adsorption of calcium and barium. Calcium is a common trace impurity of commercial titanium dioxide crystals, and tends to segregate to the surface on high temperature annealing [4], a number of studies have employed this as a convenient method of forming calcium overlayers on $TiO_2$ single crystals.

An STM study of the calcium segregated $TiO_2$(011)-(2×1) surface shows calcium forming stripe-like domains running in the [0$\bar{1}$1] direction [17]. Bright moieties within the selvedge appear to have a (2×1) or c(2×1) periodicity, however this data alone suggests no particular surface model.

Several studies have investigated segregated calcium overlayers formed on the $TiO_2$(110) surface, and two distinct surface structures have been proposed. A c(6×2) structure was proposed by Zhang *et al.* [18] based on low energy electron diffraction (LEED) and scanning tunneling microscopy (STM) results. The STM images exhibit rows along the [001] and [1$\bar{1}$0] directions of the $TiO_2$(110)-1×1 substrate, which were assigned to the formation of a $CaTiO_3$-like compound. In more recent studies, Nörenberg and Harding [19–21] reported a highly ordered p(3×1) adlayer and explained the observed c(6×2) LEED pattern in terms of anti-phase boundaries. This interpretation was supported by atomistic simulations.

Nörenberg and Harding also report a (7×2) and a "disordered" (1×4) reconstruction [21]. It was found that the p(3×1) reconstruction may be converted into the (1×4) reconstruction by annealing or electron beam irradiation, and that the two reconstructions may coexist on the same substrate terrace.

In the present work metal vapor deposition (MVD) has been used to form calcium overlayers. This approach allows precise control of calcium coverage and avoids any complications that may arise from population of the selvedge by calcium during the segregation process. Surfaces formed by MVD are also compared with those formed by bulk segregation.

## 7.2 Experimental details

Both MVD and bulk segregation experiments used rutile substrates that were slightly reduced as indicated by their transparent blue colour, all measurements were undertaken at room temperature. STM images were recorded in constant current mode with a tungsten tip held at ground potential and the sample biased positively (empty states regime) in the range 1.2 to 1.8 V, with the tunneling current in the range 0.04 to 1.2 nA. Scanning tunneling microscopy usually images titanium atom as bright rows under these conditions [22]. A detailed description of the experimental apparatus is given in chapter 3. Calcium coverages were calculated on the basis that the c(6×2) overlayer defines 1 ML of calcium.

### 7.2.1 Metal vapour deposition experiments

The MVD experiments were performed with an Omicron GmbH UHV low temperature STM, calibrated with a Cu(100)-(2×1)O surface and operating at a base pressure of $1\times10^{-11}$ mbar. The sample was prepared by repeated cycles of bombardment with 1 keV $Ar^+$ ions, and annealing to approximately 1100 K. The cleanliness of the sample was checked with Auger electron spectroscopy (AES) before calcium was deposited from a well-degassed evaporator operating at approximately 600 K. The presence of calcium on the surface was confirmed with Auger electron spectroscopy (AES) and the sample was subsequently annealed to 1100 K to order the surface calcium.

### 7.2.2 Bulk segregation experiments

The bulk segregation experiments employed an Omicron GmbH UHV room temperature STM/AFM calibrated with atomically resolved images of Si(111)-(7×7) and operating at a base pressure of $1\times10^{-10}$ mbar. The sample was prepared by repeated cycles of bombardment with 1 keV $Ar^+$ ions, and annealing to approximately 1100 K in vacuum until calcium was detected by AES and a corresponding c(6×2) LEED pattern was observed.

## 7.3 Results

### 7.3.1 Low coverage: row structure

In the low coverage regime ordered calcium overlayers were formed both by metal vapour deposition and by bulk segregation, in both cases weak c(6×2) LEED patterns were present. Figure 7.1 shows a STM image of $\sim$ 0.4 ML coverage of vapour deposited calcium on the $TiO_2$(110) surface. The image shows the substrate 1×1 rows together with short added rows in the [001] and [1$\bar{1}$0] directions. The rows have a height of 0.21 $\pm$ 0.05 nm and a width of 1.1 $\pm$ 0.2 nm (full-width at half maximum), in very good agreement with the values reported by Zhang *et al.* [18]. Their lengths in the [001] and the [1$\bar{1}$0] directions are up to $\sim$ 5 nm and up to $\sim$ 10 nm, respectively. At this coverage calcium starts to form 2D layers.

A similar structure was obtained by bulk segregation. Figure 7.2 shows a STM image with a coverage of $\sim$ 0.3 ML bulk segregated calcium. Rows extending up to $\sim$ 6.5 nm in the [001] direction are formed, whereas the length of the rows in the [1$\bar{1}$0] direction remains at $\sim$ 5 nm. Between the bright rows oxygen vacancies/hydroxyl groups can be seen This allows identification of the bright rows as containing 5-fold co-ordinated titanium atoms [22].

At higher calcium coverages obtained by MVD or bulk segregation, a denser arrangement of the calcium induced rows is formed. The rows cover most of the surface, with those in the [1$\bar{1}$0] direction extending across entire terraces.

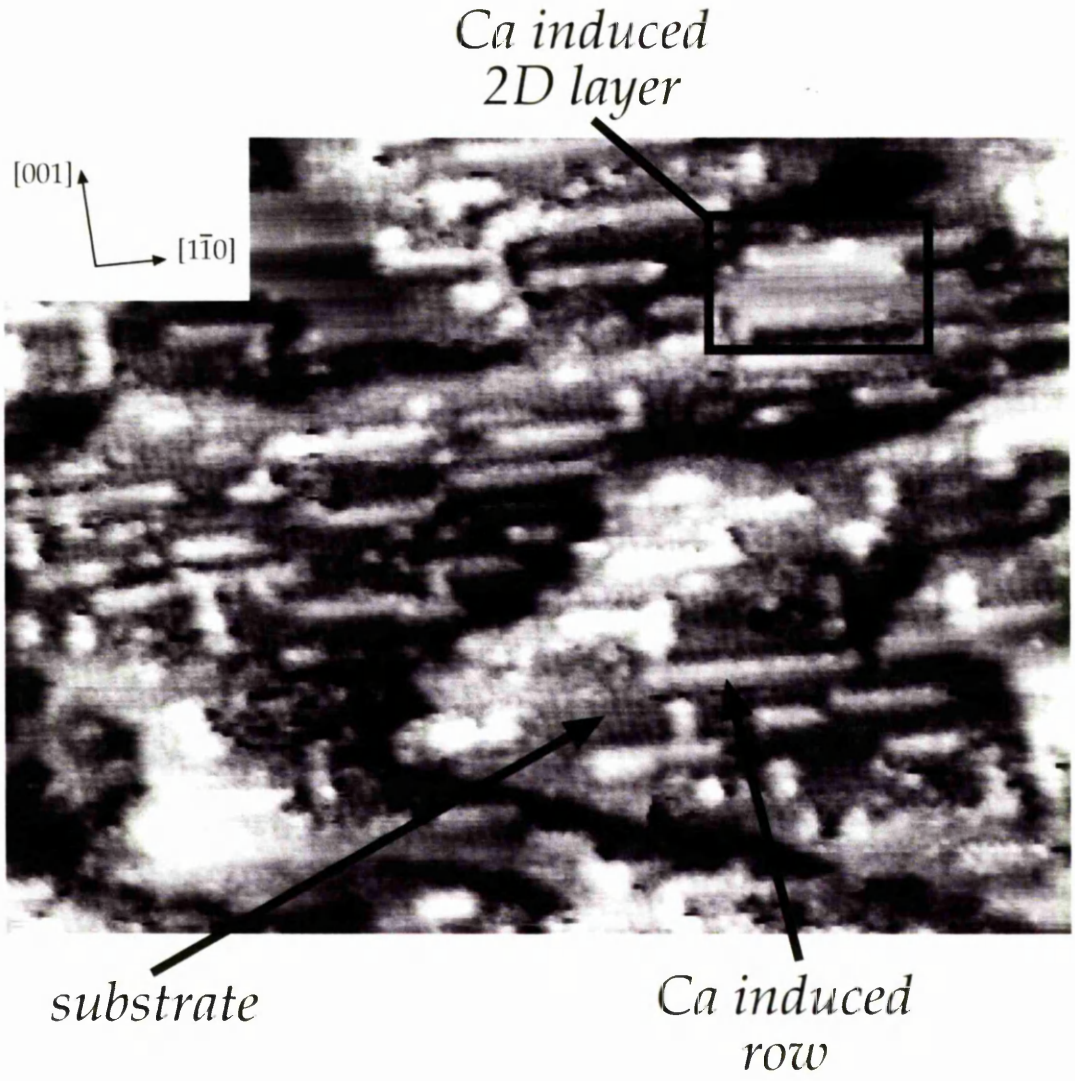


Figure 7.1: STM image (50 nm × 40 nm) of ∼ 0.4 ML of Ca/$TiO_2$(110) prepared by calcium vapor deposition.

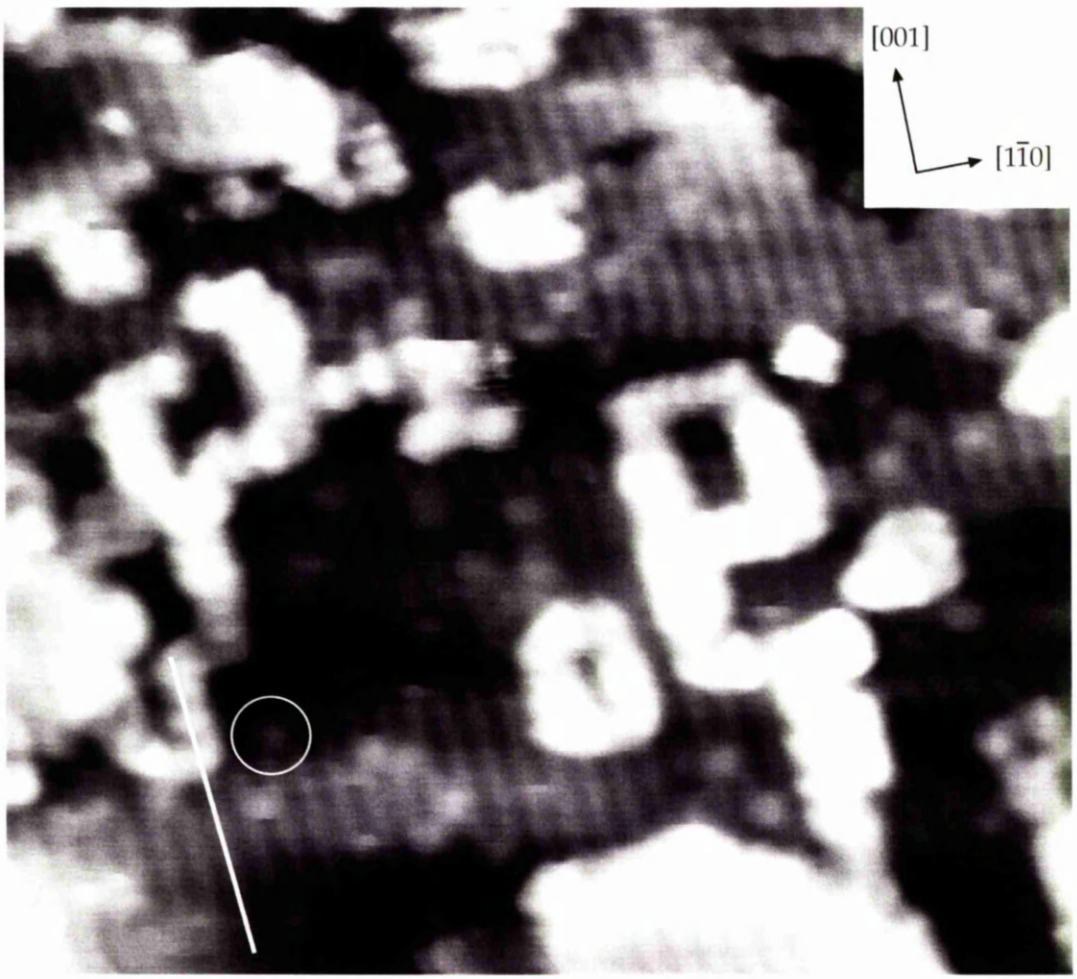


Figure 7.2: STM image (20 nm × 20 nm) of ∼ 0.3 ML of Ca/$TiO_2$(110) prepared by bulk segregation. The circle indicates the presence of an O-vacancy or a bridging hydroxyl group. The center of the overlayer calcium rows is on the bright lines of the substrate.

### 7.3.2 Monolayer coverage: c(6×2) overlayer

Metal vapour deposition was used to form a surface exhibiting a sharp c(6×2) LEED pattern, see figure 7.5. STM images of this surface shown an overlayer with a c(6×2) honeycomb structure which completely covers the rutile substrate, see figures 7.3 and 7.4a. The honeycomb network is shown schematically in figure 7.4b. In the [001] direction, the bright features are separated alternately by two substrate unit cells (2 × 0.296 nm) and four substrate unit cells (see line profile in figure 7.4c). The same configuration of bright features is seen in adjacent [001] direction rows but shifted by three unit cells in the [001] direction. Equivalent [001] direction rows are separated by two substrate unit cells (2 × 0.650 nm) in the $[1\bar{1}0]$ direction.

Ordered overlayers were also prepared by bulk segregation (see figure 7.6) leading to the same c(6×2) honeycomb structure as the overlayer formed by MVD, however it was more difficult to control the coverage formed by bulk segregation than that formed by MVD.

### 7.3.3 High coverage: $\begin{pmatrix} 2 & 0 \\ -\frac{1}{5} & 1 \end{pmatrix}$ structure

Metal vapour deposition allowed easy preparation of coverages in excess of 1 ML. At doses slightly above 1 ML, an additional structure is formed, which appears disordered and is difficult to image with STM, see figure 7.7. At higher calcium coverages the surface is completely covered by this structure and the LEED pattern of this surface exhibits a high background and weak spots, (see figure 7.8).

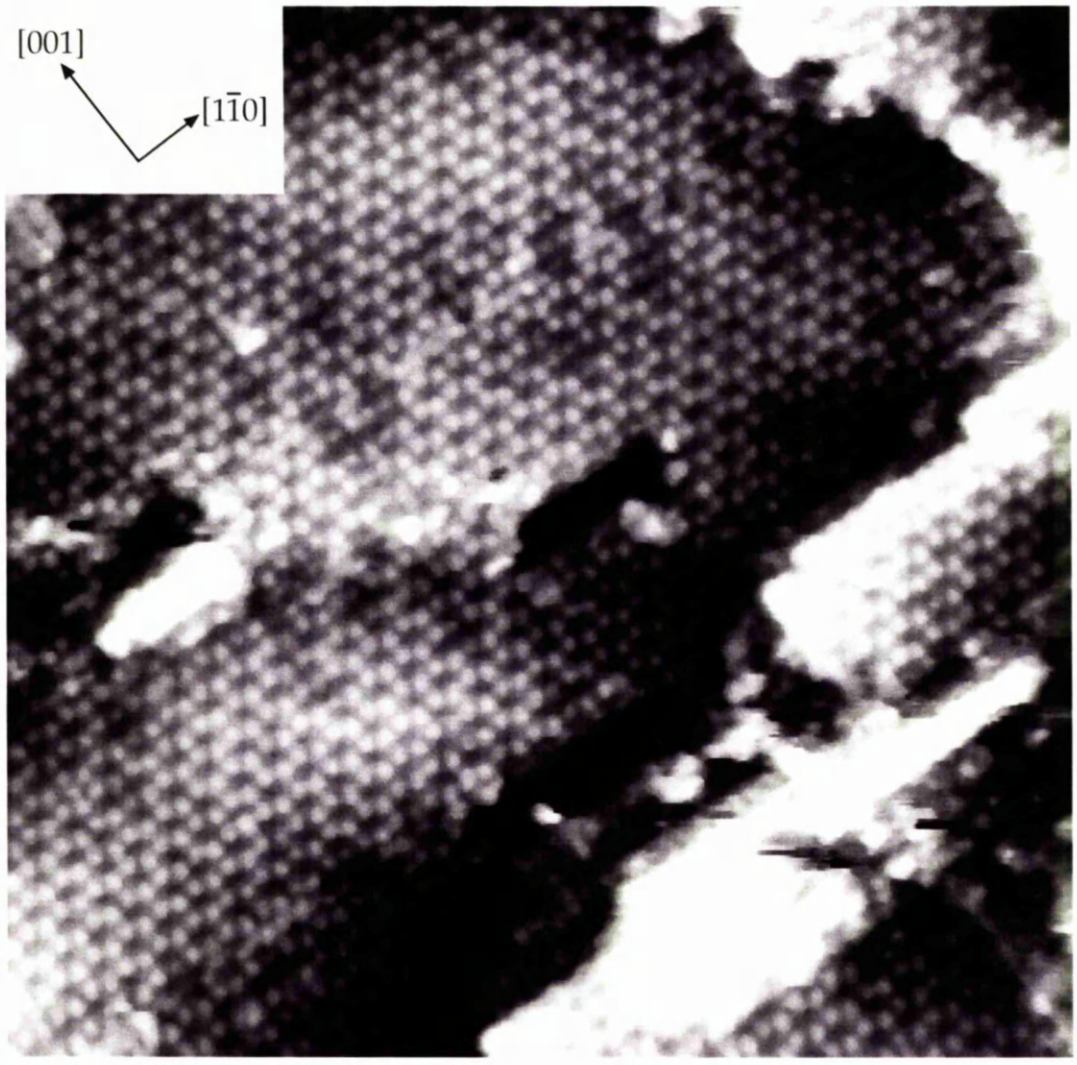


Figure 7.3: STM image (30 nm × 30 nm) of 1 ML of Ca/$TiO_2$(110) formed by calcium vapor deposition.

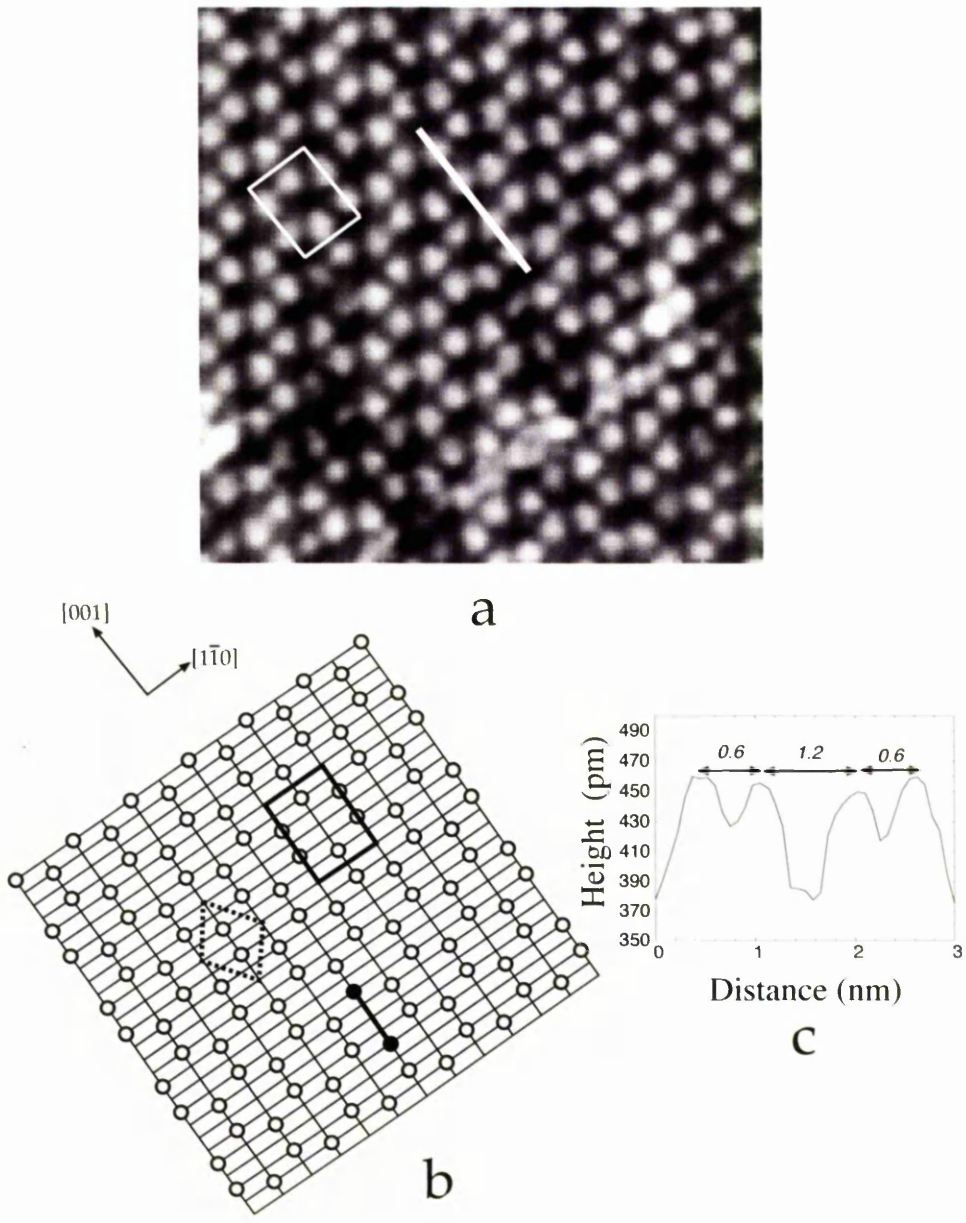


Figure 7.4: (a) STM image (9.4 nm × 9.4 nm) magnified from figure 7.3. A c(6×2) unit cell is superimposed. (b) Schematic representation of the c(6×2) overlayer superimposed on a grid representing the $TiO_2$(110) surface mesh. A c(6×2) (Wood notation) or $\begin{pmatrix} 6 & 0 \\ 0 & 2 \end{pmatrix}$ (Park and Madden notation) unit cell is delineated by a full line; a primitive unit cell $\begin{pmatrix} 3 & 1 \\ -3 & 1 \end{pmatrix}$ is delineated by a dotted line. The motif repeated at each lattice point is highlighted. (c) Line profile along the white line indicated in part a. The distance between peaks is indicated in nanometers.

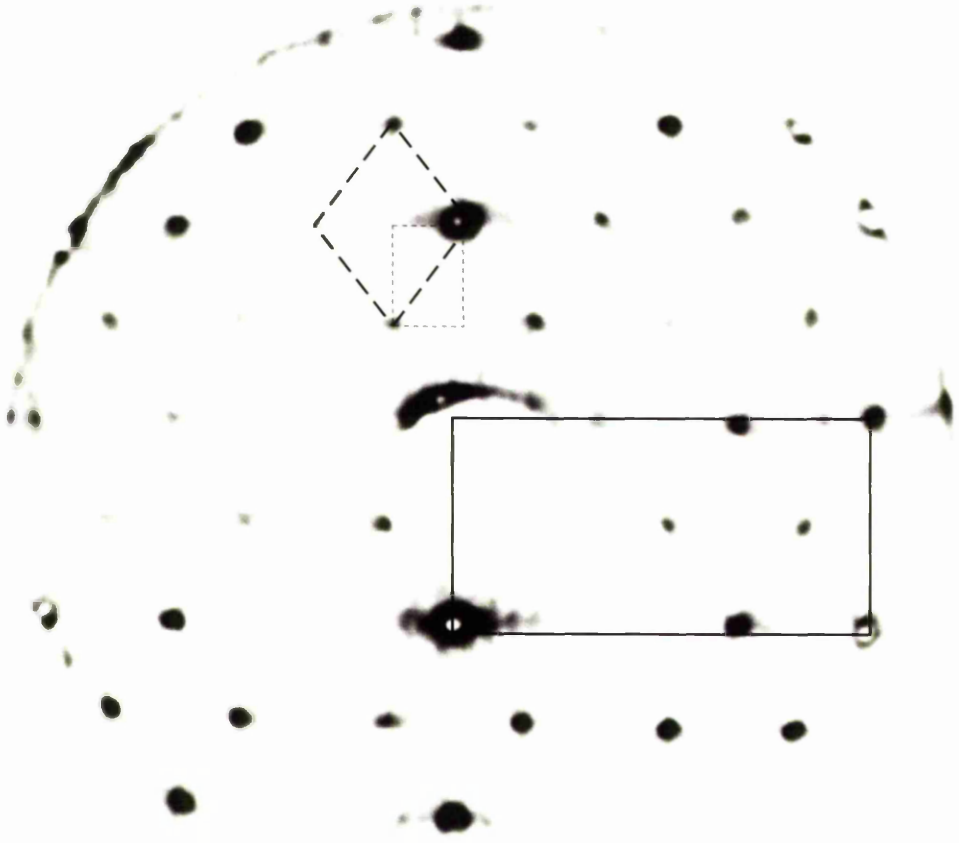

Figure 7.5: LEED pattern recorded from the calcium covered $TiO_2$(110) surface (E = 60 eV). The reciprocal space unit cell of the $TiO_2$(110) substrate is represented by a solid line. Unit cells of the selvedge are shown by dashed lines; the heavy dashed line is equivalent to the $\begin{pmatrix} 3 & 1 \\ -3 & 1 \end{pmatrix}$ cell, and the light dashed line is equivalent to the c(6×2) unit cell, note that with this choice of unit cell alternate spots are systematically absent.

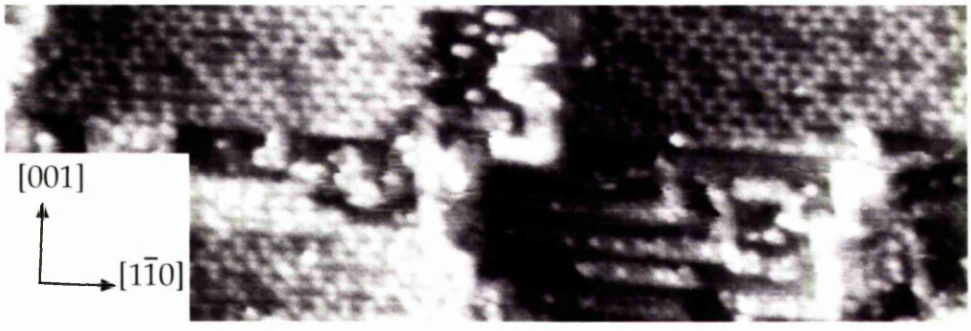


Figure 7.6: STM image (50 nm × 17 nm) of 0.7 ML of Ca/$TiO_2$(110) prepared by bulk segregation of calcium.

The c(6×2) pattern can no longer be seen, although the 1×1 unit cell of the titania substrate is still visible. A new pattern consisting of two symmetry equivalent domains of an oblique (parallelogram) surface net is superimposed. It can be seen that the titania surface and the new reconstruction are commensurate in the $[1\bar{1}0]$ direction.

The unit vectors of the new unit cell can be expressed in terms of the substrate vectors $\mathbf{b_1}$ and $\mathbf{b_2}$. If $\mathbf{b_1}$ is taken to be the longer reciprocal space vector of the substrate (horizontal in figure 7.8), then the new reciprocal space unit cell is described by the vectors:

$$\begin{aligned} \mathbf{b}_1^{\mathrm{rec}} &= \frac{\mathbf{b_1}}{2} + \frac{\mathbf{b_2}}{10} \\ \mathbf{b}_2^{\mathrm{rec}} &= \mathbf{b_2} \end{aligned} \tag{7.1}$$

The new unit cell may then be described using the notation due to Park and Madden, which expresses the vectors of the reconstruction as the product of the substrate unit vectors and a square matrix [23]. The value of this matrix has previously been given as $\begin{pmatrix} 2 & 0 \\ -\frac{1}{10} & 1 \end{pmatrix}$ [24], however it can be seen from the calculation in appendix B that the correct value is $\begin{pmatrix} 2 & 0 \\ -\frac{1}{5} & 1 \end{pmatrix}$.

Additional weak satellites are also visible around some substrate spots. Whilst these extra spots may conceivably arise from the presence of longer range surface structures, on the basis of the small number of visible spots these features are tentatively attributed to multiple scattering processes (the re-scattering of substrate spots by the overlayer and vice versa) which give rise to LEED spots at positions given by linear combinations of substrate and overlayer reciprocal

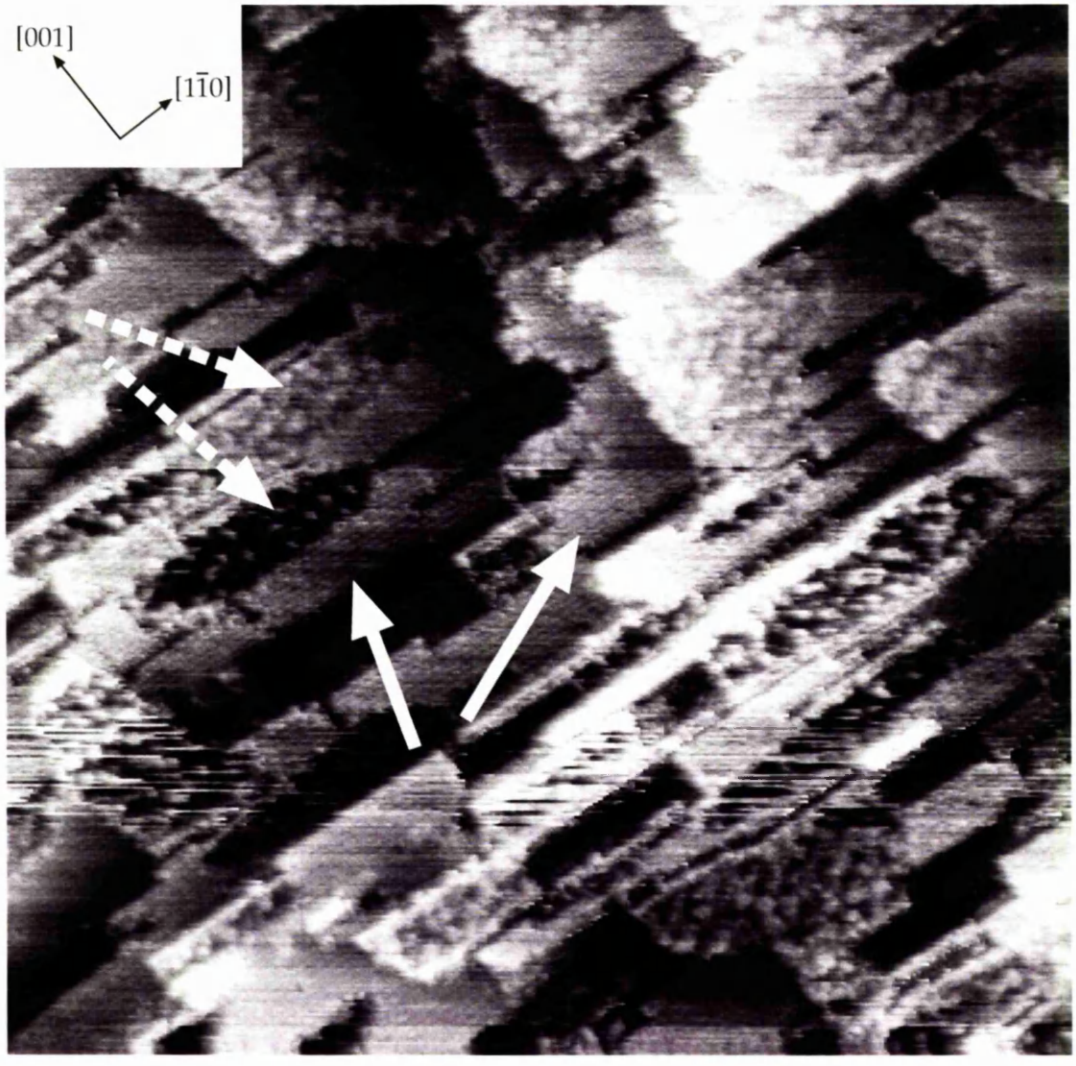


Figure 7.7: STM image (50 nm × 50 nm) of 1.2 ML of Ca/$TiO_2$(110) prepared by calcium vapor deposition. Two co-existing structures are observed; the ordered c(6×2) (indicated with solid arrows) and a new, apparently disordered structure (dashed arrows).

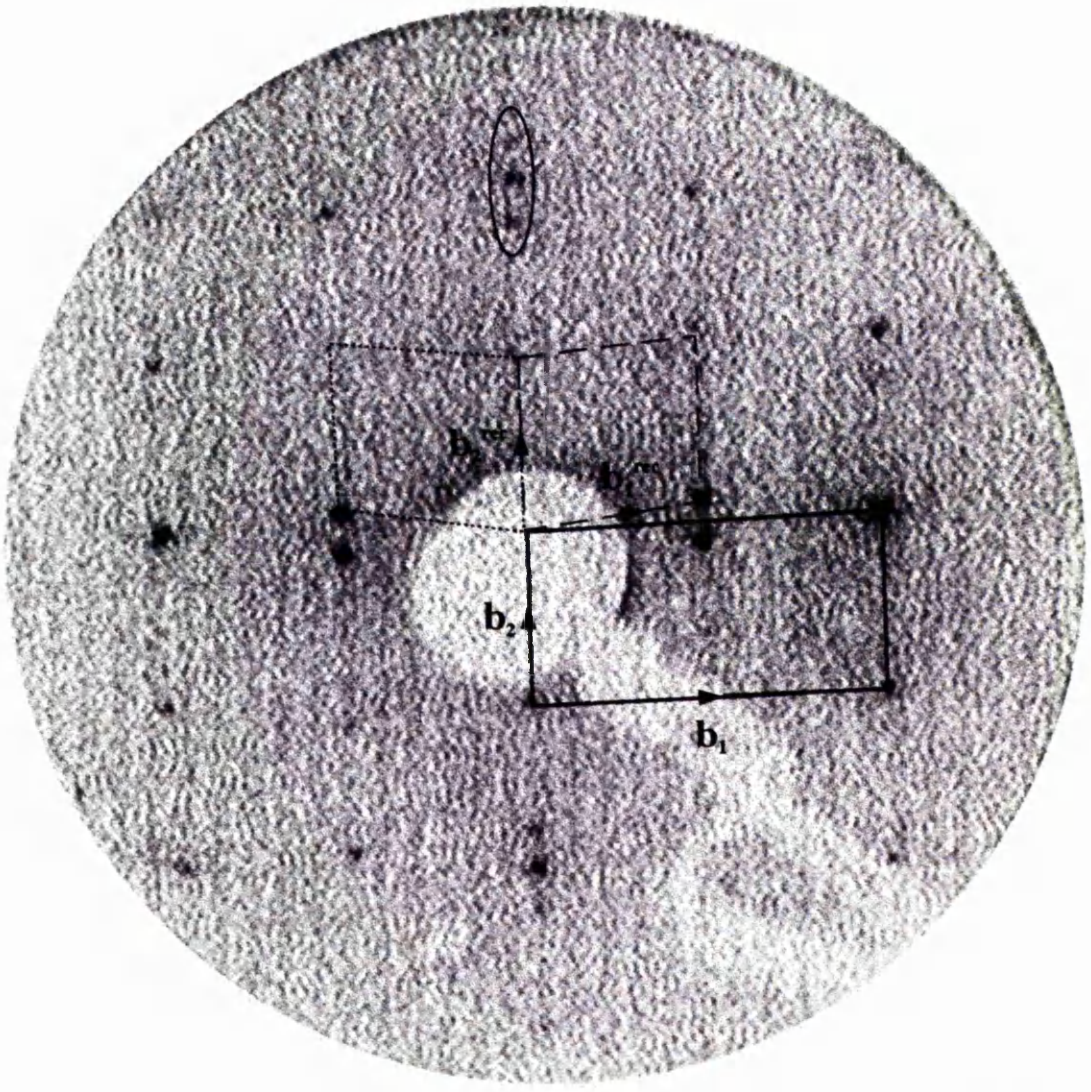


Figure 7.8: LEED pattern of the $\begin{pmatrix} 2 & 0 \\ -\frac{1}{5} & 1 \end{pmatrix}$ overlayer on $TiO_2$(110) (E = 87 eV). The $TiO_2$(110) reciprocal unit cell is indicated with full lines. The two domains of the reconstruction are indicated with dotted and dashed lines. A substrate spot with satellites is highlighted by a black ellipse.

space unit vectors. [25]. The satellite and substrate spots are separated by a vector $\pm\frac{1}{5}\mathbf{b_2}$ implying the satellites arise from scattering of substrate spots through a vector $\pm 2\mathbf{b}_1^{rec}$. It is noted that within the range of reciprocal space probed in the present work, scattering of substrate spots through a vector $\pm\mathbf{b}_1^{rec}$ simply generates spots at expected overlayer positions.

## 7.4 Discussion

In the low-coverage regime, results from the bulk segregation experiment are essentially the same as those found for MVD. The results for calcium coverages up to $\sim$ 1 ML indicate a 2D layer growth mode consistent with Ca/$TiO_2$ interfacial interaction being stronger than the Ca-Ca interaction, as predicted by Hu *et al.* on the basis of thermodynamic criteria for the growth mode of different metals on $TiO_2$(110) [26].

Turning to the structure obtained at monolayer coverage, it has previously been suggested that the apparent c(6×2) unit cell of the LEED pattern arises from the presence of anti-phase boundaries between different domains of a p(3×1) structure [19, 20]. The present STM and LEED data demonstrate that this cannot be so in the present case. The STM image in figure 7.3 shows clearly that the well ordered overlayer consists of a genuine c(6×2) structure. A LEED pattern with sharp c(6×2) overlayer spots has been recorded (figure 7.5) this observation is only consistent with the p(3×1) model if a significant density of anti-phase boundaries are present, yet high-resolution STM images such as figure

7.3 indicate an overlayer with very large domains, and very few boundaries. The symmetry of the titania substrate permits only translational or mirrored domains of a p(3×1) structure, which in the limit of large domains (see, for example, [27]), would yield a p(3×1) LEED pattern and not c(6×2). Hence the p(3×1) structure can be comprehensively rejected.

It is interesting to note that barium has recently been shown to exhibit very similar behaviour to calcium when adsorbed on $TiO_2$(110). At sub-monolayer coverages barium forms [1$\bar{1}$0] and [001] oriented rows, and in the region of monolayer coverage, STM shows a c(6×2) overlayer with the same honeycomb structure that is seen in the present work [28].

Although the c(6×2) calcium overlayer is described by the basic symmetry model shown in figure 7.4b, it is clearly not possible to rigorously determine the calcium adsorption site from the present data alone. A number of plausible adsorption sites are presented in figure 7.9. Zhang *et al.* have suggested a model where calcium atoms replace in-plane oxygen atoms to form a locally $CaTiO_3$-like structure with the bridging oxygen and the 6-fold co-ordinated titanium atoms [18]. However no modulation was detected in calcium 2p angle scan X-ray photoelectron diffraction (XPD) data [29], which rules out models where calcium substitutes in-plane oxygen atoms. Nörenberg and Harding have suggested that calcium substitutes for the 5-fold titanium atoms of the substrate, however this assertion is based on calculations employing a p(3×1) unit cell. Several experimental and theoretical studies of alkali metals on $TiO_2$(110)-1×1 point to a 3-fold hollow site (for a review, see [4]). Recent DFT investigations [8, 9] of barium adsorbed on

$TiO_2$(110) suggest barium also adsorbs in a three-fold hollow site, bound to two bridging oxygens and one in-plane oxygen — this site is labeled 3h1 in figure 7.9. As overlayers with the same periodicity are formed in both cases, it seems plausible that calcium may also adsorb in this site.

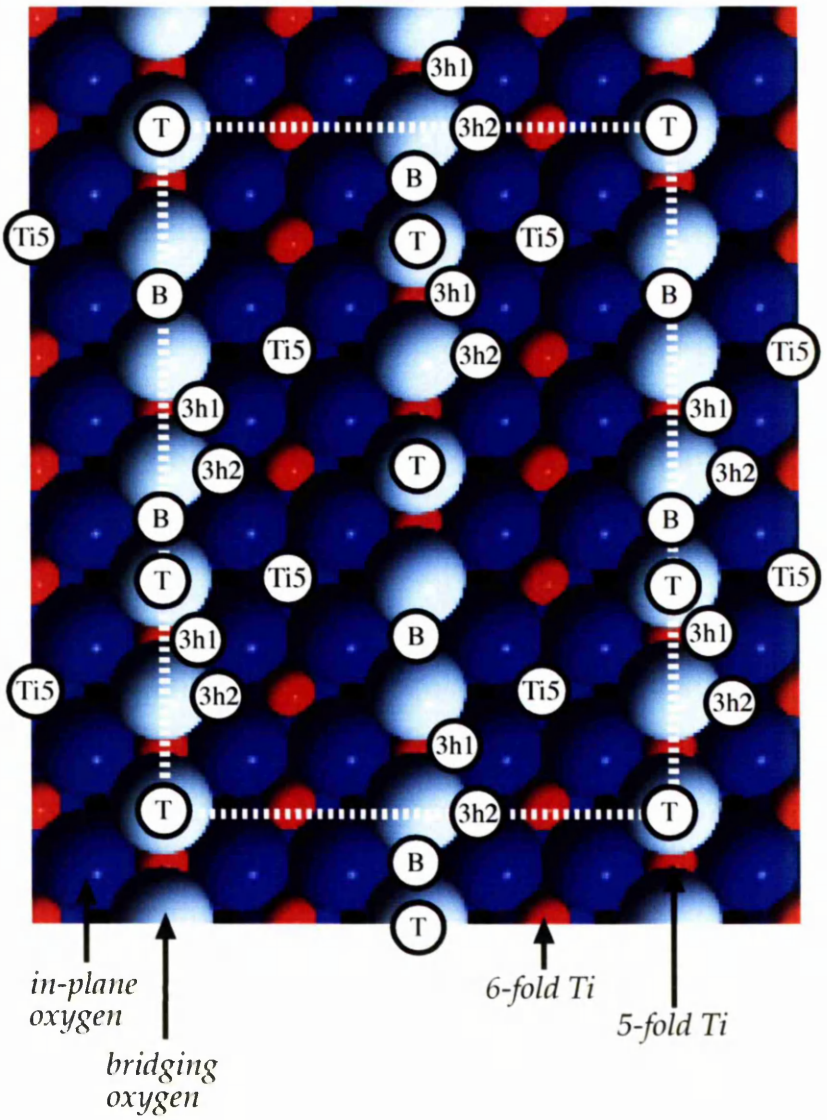


Figure 7.9: Ball model of possible adsorption sites of calcium in a c(6×2) overlayer on $TiO_2$(110): T (top), B (bridge), Ti5 (substitution of 5-fold co-ordinated titanium), 3h1 (between two bridging oxygens and one in-plane oxygen atom), and 3h2 (between one bridging oxygen and two in-plane oxygen atoms).

As alluded to above, any further investigations of the c(6×2) barium overlayers can be expected to be illuminating to the present work. Barium is a significantly more powerful scatterer of X-rays than calcium, this coupled with the ease of forming barium overlayers (commercial UHV sources are available) make it an ideal choice for SXRD measurements at a second generation light source.

Finally the $\begin{pmatrix} 2 & 0 \\ -\frac{1}{5} & 1 \end{pmatrix}$ structure is discussed. The weak spots in the LEED pattern (figure 7.8) suggest that either the overlayer has some order or it modifies the titania substrate in an ordered fashion. The apparent absence of periodicity in STM images of the this structure suggests the second possibility. A "disordered" (1×4) structure, obtained by bulk segregation, has been reported by Nörenberg and Harding [21]. STM images of this surface show that the periodicity along the $[1\bar{1}0]$ substrate direction takes the form of trenches every four substrate unit cells. As no trenches were observed in the present work, it seems most likely that the present disordered phase is not identical with the previously reported (1×4) phase. The formation of the present structure is evidently due to the increased amount of calcium on the surface, although it is not clear how the calcium excess effects and modifies the ordered c(6×2) overlayer and substrate. Given the expected variation in charge transfer with coverage, it would be instructive in future work to investigate the oxidation state of calcium and the work function through the transition from the ordered to disordered phases.

## 7.5 Summary

The low-coverage calcium reconstructions obtained by vapor deposition or bulk segregation are similar, a well ordered c(6×2) overlayer being formed in both cases. MVD allows the formation of highly ordered surface with large domains and the unambiguous assignment of a c(6×2) unit cell. With vapor deposition to coverages above a monolayer, the calcium excess gives rise to a highly disordered overlayer structure and is thought to induce a modification of the titania substrate.

# References


[1] R. Persaud and T.E. Madey. *Growth, structure and reactivity of ultrathin metal films on $TiO_2(110)$ surfaces*, volume 8 of *The chemical physics of solid surfaces*. Elsevier, 1997.

[2] C.T. Campbell. *Surf. Sci. Rep.*, 27:1–111, 1997.

[3] U. Diebold, J.M. Pan, and T.E. Madey. *Surf. Sci.*, 333:845–854, 1995.

[4] U. Diebold. *Surf. Sci. Rep.*, 48:53–229, 2003.

[5] D.P. Woodruff, editor. *Oxide Surfaces*, volume 9 of *The chemical physics of solid surfaces*. Elsevier, 2001.

[6] H. Onishi, T. Aruga, C. Egawa, and Y. Iwasawa. *Surf. Sci.*, 199:54–66, 1988.

[7] R. Lindsay, E. Michelangeli, B.G. Daniels, M. Polcik, A. Verdini, L. Floreano, A. Morgante, J. Muscat, N.M. Harrison, and G. Thornton. *Surf. Sci.*, 547:L859–L864, 2003.

[8] M.A. San Miguel, J. Oviedo, and J.F. Sanz. *J. Mol. Structure-Theochem*, 769:237–242, 2006.

[9] M.A.S. Miguel, J. Oviedo, and J.F. Sanz. *J. Phys. Chem. B*, 110:19552–19556, 2006.

[10] K. Coulter, D.W. Goodman, and R.G. Moore. *Catal. Lett.*, 31:1–8, 1995.

[11] T. Hirano. *Appl. Catal.*, 28:119–132, 1986.

[12] T. Hirano. *Appl. Catal.*, 26:65–79, 1986.

[13] T. Hirano. *Appl. Catal.*, 26:81–90, 1986.

[14] H.J. Freund. *Surf. Sci.*, 500:271–299, 2002.

[15] M. Svetina, L.C. Ciacchi, O. Sbaizero, S. Meriani, and A. De Vita. *Acta Mater.*, 49:2169–2177, 2001.

[16] E. Wieser, I. Tsyganov, W. Matz, H. Reuther, S. Oswald, T. Pham, and E. Richter. *Surf. Coat. Tech.*, 111:103–109, 1999.

[17] O. Dulub, C. Di Valentin, A. Selloni, and U. Diebold. *Surf. Sci.*, 600:4407–4417, 2006.

[18] L.P. Zhang, M. Li, and U. Diebold. *Surf. Sci.*, 413:242–251, 1998.

[19] H. Norenberg and J.H. Harding. *Appl. Surf. Sci.*, 142:174–176, 1999.

[20] H. Norenberg and J.H. Harding. *Phys. Rev. B*, 59:9842–9845, 1999.

[21] H. Norenberg and J.H. Harding. *Surf. Sci.*, 473:151–157, 2001.

[22] U. Diebold, J.F. Anderson, K.O. Ng, and D. Vanderbilt. *Phys. Rev. Lett.*, 77:1322–1325, 1996.

[23] R.L. Park and H.H. Madden. *Surf. Sci.*, 11:188, 1968.

[24] O. Bikondoa, C.L. Pang, C.A. Muryn, B.G. Daniels, S. Ferrero, E. Michelangeli, and G. Thornton. *J. Phys. Chem. B*, 108:16768–16771, 2004.

[25] L.J. Clarke. *Surface crystallography - An introduction to low energy electron diffraction.* Wiley-Interscience, 1985.

[26] M. Hu, S. Noda, and H. Komiyama. *Surf. Sci.*, 513:530–538, 2002.

[27] M.A. Van Hove, W.H. Weinberg, and C-M Chan. *Low-energy electron diffraction; experiment, theory and surface structure determination*, volume 6 of *Springer series in surface science.* Springer-Verlag, 1986.

[28] C.L. Pang, A. Sasahara, and H. Onishi. *J. Phys. Chem. C*, 111:9221–9226, 2007.

[29] E. Michelangeli and R. Lindsay. Private communication.

# Chapter 8

# Conclusions and further work

The work presented in this thesis concerns structural investigations of adsorbate covered metal and metal oxide surface, concentrating on well ordered, low index, single crystal surfaces with adsorbate coverages in the region of one monolayer. Surface structure has been probed with Surface X-ray diffraction (SXRD), a rigorously quantitative probe of surface geometry, as well as scanning tunneling microscopy (STM) and low energy electron diffraction (LEED). The theory and practice of SXRD is described in chapter 2, scanning tunnelling microscopy is described in chapter 3.

In chapter 5 a SXRD study of the Ni(110)c(2×2)-CN surface is described. It was found that the formation of the ordered CN overlayer gives rise to an expansion of the top Ni-Ni interlayer spacing by $11 \pm 2\%$ from the bulk value, but no other restructuring of the selvedge was apparent. This relaxation is in excellent agreement with several other theoretical and experimental studies of this system

[1–3], but at odds with a MEIS study [4] which reports a significantly larger expansion ($21 \pm 2\%$). As can be seen from table 5.1 on page 108, this work confirms the validity of the smaller value and indicates that the MEIS result is probably anomalous and should be re-investigated. This discrepancy highlights the relative immaturity of the currently available probes of surface structure as compared with better established techniques used in bulk crystallography, and points up the importance of applying several different structural probes when investigating surface structure.

The present SXRD study, and DFT calculations [3] are unable to reproduce a number of small substrate motions reported in a LEED-IV study of the Ni(110)c(2×2)-CN surface, including a lateral zigzag distortion of the second Ni layer in the [001] azimuth [2]. In the absence fractional order data the sensitivity to such small motions is to some degree open to question. A more rigorous experimental test for the presence of such motions would be provided by a further SXRD investigation of this surface employing a third generation light source. The much greater available X-ray flux can be expected to allow resolution of the fractional order data; an SXRD study of CO on Ni(110) [5] suggests that measurements at a third generation source should be able to resolve fractional order data on a reasonable time scale, even if the cyanide overlayer is the only portion of the selvedge to adopt the c(2×2) translational symmetry. A third generation source will also provide X-rays at shorter wavelengths, extending the volume of reciprocal space probed, and thus increasing sensitivity to atomic motions.

Looking further it is noted that c(2×2)-CN overlayers have been reported on the

(110) surfaces of three fcc transition metals; Ni [1], Rh [6] and Pd [7], and in each case cyanide was found in the same position on the surface with a tilt in the range 18–25°. In contrast to the Ni(110) case, where no reconstruction has been found, formation of the c(2×2)-CN overlayer on Rh leads to a rumpling of the second layer of the substrate, altering its translation symmetry. It will thus be interesting to investigate whether the formation of a c(2×2)-CN overlayer on Pd gives rise to any reconstruction of the substrate. SXRD and LEED-IV are obvious methods for such an investigation. Another fcc transition metal, copper, has a similar lattice constant to those already discussed, and can be prepared to give a (110)-1×1 surface. It would be pertinent to investigate if a c(2×2)-CN layer may be formed on this surface, and to investigate the structure of the selvedge in this case. Photoelectron diffraction has the great advantage of not requiring any long range surface order, so if an ordered layer is not formed, scanned energy photoelectron diffraction (PhD) from C and N 1s core levels — as employed in the case of Ni(110)c(2×2)-CN [1] — could be used to investigation the CN adsorption site.

In chapter 6 a second SXRD study is described which aimed to elucidate the structure of the $TiO_2$(110)(3×1)-S surface. Taken together with existing STM and photoemission data [8], it was shown that on formation of a (3×1)-S overlayer on $TiO_2$(110), sulphur adsorbs in a position bridging 6-fold titanium atoms, and all bridging oxygens are lost. The replacement of a bridging oxygen atom with sulphur is thought to give rise to the significant motion of co-ordinated 6-fold titanium atoms away from the adsorbate, along with a concomitant rumpling

of the second (oxygen) substrate layer. In contrast to the Ni(110)c(2×2)-CN surface which has been the subject of a number of different structural probes as well as theoretical investigations, the work in chapter 6 is the first rigorously quantitative attempt to investigate the structure of the (3×1)-S surface. It is also noted that whilst the Ni(110)c(2×2)-CN surface gives rise to a LEED pattern with sharp spots, no reconstruction of the selvedge is found, whereas in the case of $TiO_2$(110)(3×1)-S surface a significant degree of reconstruction of the substrate is indicated.

In light of the difficulty encountered in distinguishing between adsorption sites, and the ambiguities due to the absence of fractional order data, an obvious extension of such work would be to repeat the SXRD measurements at a third generation light source, though if the inter-domain phase shift described in section 6.4 is responsible for the absence of fractional order data it may be necessary to form a more ordered overlayer before it is possible to resolve fractional order rods. Experimenting with varied sulphur coverage and annealing temperature would be the first approach to this problem. However it is thought that the adsorption of sulphur on $TiO_2$(110) above 390 K is driven by diffusion of bulk defects to the surface [9], and so the rate of arrival of defects at the surface may be an important parameter. This raises the possibility that forming a highly ordered overlayer requires the optimisation of not only annealing temperature, but also degree of bulk reduction and dosing rate. As the degree of bulk reduction is difficult to measure *in-situ* and is subject to change with repeated sample

preparation, optimising the conditions for the formation of highly ordered sulphur overlayers may be very demanding. Given that fractional order spots have been clearly and reproducibly observed in LEED patterns, LEED-IV may be the most promising approach for future determination of this surface structure.

An alternative approach would be to use scanned energy photoelectron diffraction (PhD) from a sulphur core levels to determine the adsorption site of the sulphur. PhD will be able to distinguish between bridge and atop sites, and it is reasonable to suppose that it will be able to distinguish between sites on 5 and 6-fold rows [10], or reveal previously unconsidered sites. Precise knowledge of the adsorption site would provide a significant constrain on optimisation when modeling the present, modest, SXRD data set. Ideally future work will lead to a convincing consensus between models obtained with different experimental methods and those determined theoretically, as has been reached in the case of Ni(110)c(2×2)-CN.

Other well ordered structures formed by sulphur on $TiO_2$(110) would be interesting candidates for structural investigations which would rigorously test the proposed models for the (3×3)-S and (4×1)-S surfaces [11], and investigate the significant restructuring that can be expected from surfaces denuded of bridging oxygen, and with sulfur replacing in-plane oxygens.

The dynamics of sulphur adsorption on $TiO_2$ is an area of particular interest, which can be expected to be particularly illuminating to the development of poisoning resistant and more efficient desulphurisation catalysts. Dynamical

considerations largely fall beyond the scope of the structural probes which have been employed in this thesis, however the author suggests two experiments which may illuminate some aspects of the surface dynamics.

It is thought that when dosing sulphur at room temperature, a small number of bridging oxygen vacancies are the preferred sulphur adsorption sites [9, 12, 13], and that the sulphidation of the surface is driven by the arrival of bulk defects at the surface [9]. It would be straightforward to employ a variable temperature STM which may image at elevated temperatures [14] to determine whether sulphur adsorbed at surface defects acts as nucleation centres for high temperature adsorption, or whether sulphur adsorbs at essentially random positions on the surface.

One unresolved point is Langel's assertion, on the basis of first principle molecular dynamics simulations [15], the retention of one bridging oxygens per (3×1) unit cell is as energetically favourable as the case with no bridging oxygen indicated by the present work. The presence of one bridging oxygen per (3×1) cell lowers the symmetry so two distinct orientations of the unit cell may exist on the surface, rotated by 180° relative to each other. As both orientations will be equally likely to form, the author suggests that the growth of large domains of one configuration may be impeded by the presence of the rotated configuration. If this is the case it follows that although the surface structure containing a single bridging oxygen and one sulphur per (3×1) unit cell is thermodynamically stable, it does not easily form large, well ordered domains, and the presence of a high quality (3×1) LEED pattern is predicated on the formation of a surface denuded of bridging oxygen.

It has been observed with STM and LEED, that whilst (3×1) ordering can be created by dosing sulphur at 470 K, dosing to a similar coverage at 420 K leads to a surface with sulphur on bridging oxygen rows, but without long range ordering [9]. On the basis of existing work [8, 9, 11], it is reasonable to suppose that more bridging oxygen will be retained when dosing at lower annealing temperatures, in which case it is suggested that the surface prepared at the lower temperature may retain a population of bridging oxygens in the region of $\frac{1}{3}$ of a monolayer, and would be dominated by very small domains of a surface phase consisting of one bridging oxygen and one sulphur per (3×1) unit cell. A second experiment could test this supposition using some form of photelectron diffraction. This technique is sensitive to the local environment of the adsorbate probed, and thus can be expected to indicate the presence or absence of a significant population of bridging oxygens adjacent to sulphur atoms on the disordered surface prepared at 420 K. It would probably be sensible to pair such an investigation with measurement of the photoemission peaks previously investigated, LEED, and if possible STM.

Chapter 7 describes the use of STM and LEED to investigate the structure of Ca adlayers on $TiO_2$(110) formed by metal vapour deposition and bulk segregation. It was found that similar structures were formed by both methods. At low calcium coverages, rows with widths in the region 1 nm developed in the [1$\bar{1}$0] and [001] azimuths. At coverages equivalent to a single calcium layer, a c(6×2) overlayer was formed, calcium vapour deposition allowed the formation of a highly ordered surface with large domains and hence, the unambiguous assignment of a c(6×2) unit cell. Vapour deposition also allowed the formation of higher coverage

overlayers with a LEED pattern indicating the formation of a $\begin{pmatrix} 2 & 0 \\ -\frac{1}{5} & 1 \end{pmatrix}$ surface structure. In this case the overlayer itself is though to be disordered, with the new periodicity arising from restructuring of the substrate.

The c(6×2) structure is a clear candidate for structural investigation. Whilst angle scan X-ray photoelectron diffraction (XPD) has yielded little structural information, scanned energy mode photoelectron diffraction (PhD) should reveal the calcium adsorption site. The highly ordered surface is well suited to LEED-IV or SXRD investigations that can be expected to yield a full structure including adsorption site and substrate structure. It is noted that models trialed should include, but not be limited to, those including two calcium atoms per primitive unit cell (see fig 7.4 on page 156) as it is well understood that bright moieties on the surface do not necessarily correspond to individual atoms [16, 17]. Given the potential complexity of the surface structure, the results of a PhD study revealing the calcium adsorption site and local geometry would be a valuable constraint, simplifying the analysis of LEED-IV or SXRD data.

Barium has also been seen to form a c(6×2) overlayer, and the same honeycomb structure is observed with STM, so any structural investigation of this surface will be illuminating to the study of calcium. Barium is a significantly more powerful scatterer of X-rays than calcium, this coupled with the ease of forming barium overlayers (commercial UHV sources are available) make it an ideal choice for SXRD measurements at a second generation light source.

Determining the structure of the $\begin{pmatrix} 2 & 0 \\ -\frac{1}{5} & 1 \end{pmatrix}$ surface is a particularly demanding

proposition. If, as suggested, the reconstructed substrate lies under a disordered overlayer then in principle, the structure of the ordered part can be determined by SXRD, though the poorly ordered structure is probably ill suited to crystallographic investigation. X-ray reflectivity is insensitive to lateral structure, giving only structural information perpendicular to the surface, but unlike crystal truncation rod data, reflectivity data would be sensitive to the presence of a disordered layer. A reflectivity investigation can then be expected to yield some structural information from both the ordered and disordered parts of the surface, and is probably the most fruitful method by which to begin investigating this surface phase.

# References


[1] N.A. Booth, R. Davis, D.P. Woodruff, D. Chrysostomou, T. Mccabe, D.R. Lloyd, O. Schaff, V. Fernandez, S. Bau, K.M. Schindler, R. Lindsay, J.T. Hoeft, R. Terborg, P. Baumgartel, and A.M. Bradshaw. *Surf. Sci.*, 416:448–459, 1998.

[2] C. Bittencourt, E.A. Soares, and D.P. Woodruff. *Surf. Sci.*, 526:33–43, 2003.

[3] M.J. Knight, J. Robinson, and D.P. Woodruff. *Surf. Sci.*, 580:145–152, 2005.

[4] D. Brown, D.P. Woodruff, T.C.Q. Noakes, and P. Bailey. *Surf. Sci.*, 476:L241–L246, 2001.

[5] K.F. Peters, C.J. Walker, P. Steadman, O. Robach, H. Isern, and S. Ferrer. *Phys. Rev. Lett.*, 86:5325–5328, 2001.

[6] F. Bondino, A. Baraldi, H. Over, G. Comelli, P. Lacovig, S. Lizzit, G. Paolucci, and R. Rosei. *Phys. Rev. B*, 64:085422, 2001.

[7] F. Bondino, E. Vesselli, A. Baraldi, G. Comelli, A. Verdini, A. Cossaro, L. Floreano, and A. Morgante. *J. Chem. Phys.*, 118:10735–10740, 2003.

[8] E.L.D. Hebenstreit, W. Hebenstreit, and U. Diebold. *Surf. Sci.*, 461:87–97, 2000.

[9] E.L.D. Hebenstreit, W. Hebenstreit, H. Geisler, C.A. Ventrice, P.T. Sprunger, and U. Diebold. *Surf. Sci.*, 486:L467–L474, 2001.

[10] R. Lindsay. Private communication.

[11] E.L.D. Hebenstreit, W. Hebenstreit, and U. Diebold. *Surf. Sci.*, 470:347–360, 2001.

[12] E.L.D. Hebenstreit, W. Hebenstreit, H. Geisler, S.N. Thornburg, C.A. Ventrice, D.A. Hite, P.T. Sprunger, and U. Diebold. *Phys. Rev. B*, 64:115418, 2001.

[13] J.A. Rodriguez, J. Hrbek, Z. Chang, J. Dvorak, T. Jirsak, and A. Maiti. *Phys. Rev. B*, 65:235414, 2002.

[14] A.J. Limb. *Scanning Tunnelling Microscopy: Studies of Fe, Cr and $SO_2$ Adsorption on Rutile $TiO_2$ (110).* PhD thesis, University of Manchester, 2002.

[15] W. Langel. *Surf. Sci.*, 600:1884–1890, 2006.

[16] M.A. van Hove, J. Cerda, P. Sautet, M.L. Bocquet, and M. Salmeron. *Prog. Surf. Sci.*, 54:315–329, 1997.

[17] D.P. Woodruff. *Surf. Sci*, 500:147–171, 2000.

# Appendix A

# Effect of missing fractional order data

The contribution of the surface to the structure factor, assuming thermal vibrations may be ignored is given as [1]:

$$F_{surface,hkl} = \sum_{unit\ cell} f_i e^{2\pi i(hx_i+ky_i+lz_i)} \tag{A.1}$$

where $f_i$ is the atomic form factor, $h, k, l$ are reciprocal space indices of the data and $x_i, y_i, z_i$ are fractional, real space co-ordinates of atom $i$. The contribution to this sum from a single atom is then:

$$F_{atom} = f_{atom} e^{2\pi i(hx+ky+lz)} \tag{A.2}$$

In the present case only CTR data is present; as the rods are indexed against the (1×1) unit cell then $h = \pm 0, 1, 2, 3, 4 \cdots$ and $k = \pm 0, 1, 2, 3, 4 \cdots = \pm n$. Fractional order data occurs at $h = \pm 0, 1, 2, 3, 4 \ldots$ and $k = \pm \frac{1}{3}, \frac{2}{3}, \frac{4}{3}, \frac{5}{3} \ldots$ hence

for CTR data only:

$$F_{atom} = f_{atom} e^{2\pi i(hx+ny+lz)} \tag{A.3}$$

Invoking the identity that:

$$e^{i\theta_1} = e^{i\theta_2} \quad \text{when} \quad \theta_1 = \theta_2 \pm 2m\pi \quad \text{where} \quad m = integer \tag{A.4}$$

It becomes clear that:

$$f_{atom} e^{2\pi i(hx+ny+lz)} = f_{atom} e^{2\pi i(hx+n(y+1)+lz)} = f_{atom} e^{2\pi i(hx+n(y+2)+lz)} \ldots \tag{A.5}$$

Hence for CTR data, the value for $F_{hkl}$ will be invariant under any motion of an atom an integer number of (1×1) unit cells in the [001] direction. This will be true irrespective of the number of domains, and whether they add coherently or incoherently, but is not true for fractional order data. This is equivalent to modeling the data with a (1×1) periodicity where some of the atoms are allowed to split — the information that is lost in the absence of fractional order data is which of the three (1×1) unit cells a given atom or motion falls in. Whilst in principle this means it is not possible to differentiate between a large number of surface structures, in practice only the small subset of the possibilities retaining *p2mm* symmetry need be considered. In the remaining part of this appendix, two particular consequences of the absence of fractional order data are considered.

For the case of one sulphur replacing a bridging oxygen and one bridging oxygen per (3×1) unit cell retained, there are three mirror image pairs of possible surface configurations shown schematically in figure A.1. It can readily be seen that with the present data set all these cases give rise to the same values of $F_{hkl}$ even if substrate motions consistent with *p2mm* or *p1m1* symmetry are permitted.

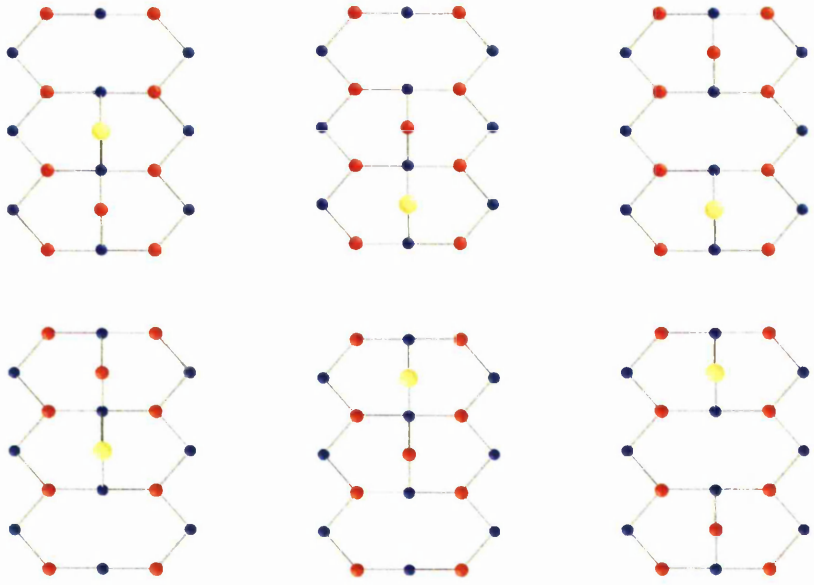

Figure A.1: Schematics of the the six possible surface configurations for the case of one sulphur adsorbed bridging 6-fold titaniums and one bridging oxygen per (3×1) unit cell. Sulphur is represented by yellow spheres, oxygen by red spheres, and titanium by blue spheres. For clarity atoms below the top substrate layer ($L_1$) are not shown.

Hence investigating this case requires the computation of only one of the illustrated surface structures, though in the event of excessively short or long bonds it is necessary to check if reasonable bond lengths can be achieved by shifting bridging oxygen or sulphur by a number of (1×1) unit cells in the [001] direction.

Examining figure 6.6 on page 132 it can be seen that there is a single choice of motions in the [110] and [$\bar{1}$10] directions that give the maximum possible number of motions that retain *p2mm* symmetry. In the [001] direction there is a unique choice of atoms that can be moved, e.g.Ti(2) and Ti(3) may move in this direction but not Ti(1) or Ti(4), however allowing shifts of an arbitrary number of (1×1) unit cells in the [001] direction means there are always two choices of motions —

inward and outward. In practice this means that whilst the amplitude of [001] motions is defined, the direction of motions is not, so some bond lengths in the surface may adopt two, or more, distinct values. On encountering a model with problematic bond lengths a careful search must be made for interchanges of [001] motions that may give rise to a more reasonable bond lengths.

# References

[1] E. Vlieg and I.K. Robinson. Two-dimensional crystallography. In P. Coppens, editor, *Synchrotron Radiation Crystallography*. Academic Press, 1992.

# Appendix B

# Determination of real space unit cell

When presented with a novel LEED pattern arising from the reconstruction of a surface or formation of an overlayer, it is often possible to directly identify the real space unit cell of the new surface. In the case of more complex structures, an analytical method of determining the real space unit cell from the reciprocal space unit cell may be required. In this appendix a suitable transformation is derived, and is then employed to determine the real space unit cell of the high calcium coverage surface described in section 7.3.3.

The real space substrate unit cell is described by vectors $\mathbf{a_1}$ and $\mathbf{a_2}$, and the new surface unit cell is described by vectors $\mathbf{a_1^{rec}}$ and $\mathbf{a_2^{rec}}$ which can be expressed in

terms of the substrate vectors:

$$\begin{aligned} \mathbf{a}_1^{\mathrm{rec}} &= m_{11}\mathbf{a}_1 + m_{12}\mathbf{a}_2 \\ \mathbf{a}_2^{\mathrm{rec}} &= m_{21}\mathbf{a}_1 + m_{22}\mathbf{a}_2 \end{aligned} \tag{B.1}$$

This is equivalent to generating the vectors of the new unit cell from the product of a square matrix $M$ and substrate unit vectors:

$$\begin{pmatrix} \mathbf{a}_1^{\mathrm{rec}} \\ \mathbf{a}_2^{\mathrm{rec}} \end{pmatrix} = \begin{pmatrix} m_{11} & m_{12} \\ m_{21} & m_{22} \end{pmatrix} \begin{pmatrix} \mathbf{a}_1 \\ \mathbf{a}_1 \end{pmatrix} \tag{B.2}$$

or:

$$\mathbf{a}^{\mathrm{rec}} = M \cdot \mathbf{a} \tag{B.3}$$

Likewise the substrate surface is described by reciprocal space vectors $\mathbf{b_1}$ and $\mathbf{b_2}$, and the new surface unit cell by reciprocal space vectors $\mathbf{b}_1^{\mathrm{rec}}$ and $\mathbf{b}_2^{\mathrm{rec}}$ thus:

$$\mathbf{b}^{\mathrm{rec}} = N \cdot \mathbf{b} \tag{B.4}$$

where:

$$N = \begin{pmatrix} n_{11} & n_{12} \\ n_{21} & n_{22} \end{pmatrix} \tag{B.5}$$

The vectors $\mathbf{b}^{\mathrm{rec}}$ and hence matrix $N$ may be derived from observation of the new LEED pattern. A direct transformation between $N$ and $M$ may be derived as follows; in chapter 2 general reciprocal space vectors were defined such that:

$$\mathbf{a_i} \cdot \mathbf{b_j} = 2\pi\delta_{i,j} \tag{B.6}$$

where $\delta_{i,j}$ is the Kronecker delta which takes a value of unity when $i = j$ and is zero otherwise. This condition can be expressed in matrix form as:

$$\begin{pmatrix} a_1 \\ a_2 \end{pmatrix} \cdot \begin{pmatrix} b_1 & b_2 \end{pmatrix} = \mathbf{a} \cdot (\mathbf{b})^{\mathrm{T}} = 2\pi \begin{pmatrix} 1 & 0 \\ 0 & 1 \end{pmatrix} = 2\pi I \tag{B.7}$$

where $I$ is the unit matrix, hence:

$$\mathbf{a}^{-1} = \frac{(\mathbf{b})^{\mathrm{T}}}{2\pi} \tag{B.8}$$

An expression for $M$ can be obtained from equation B.3:

$$M = \mathbf{a}^{\mathbf{rec}} \cdot \mathbf{a}^{-1} = \mathbf{a}^{\mathbf{rec}} \cdot \frac{(\mathbf{b})^{\mathrm{T}}}{2\pi} \tag{B.9}$$

and from equation B.4:

$$M = \frac{1}{2\pi}\mathbf{a}^{\mathbf{rec}} \cdot \left((N)^{-1} \cdot \mathbf{b}^{\mathbf{rec}}\right)^{\mathrm{T}} \tag{B.10}$$

Effecting the inversion of matrix $N$ yields:

$$M = \frac{1}{2\pi}\frac{1}{det\ N}\,\mathbf{a}^{\mathbf{rec}} \cdot \left(\begin{pmatrix} n_{22} & -n_{12} \\ -n_{21} & n_{11} \end{pmatrix} \cdot \mathbf{b}^{\mathbf{rec}}\right)^{\mathrm{T}} \tag{B.11}$$

Evaluating the multiplications in the equation above will give rise to terms consisting of $n_{11}, n_{12}, n_{21}$ or $n_{22}$ with coefficients $\mathbf{a}_{\mathbf{i}}^{\mathbf{rec}} \cdot \mathbf{b}_{\mathbf{j}}^{\mathbf{rec}}$. From equation B.6, in the cases where $i \neq j$ the coefficient term will be zero, in cases where $i = j$ the coefficient will be $2\pi$. Carrying out these matrix multiplications gives:

$$M = \frac{1}{det\ N}\begin{pmatrix} n_{22} & -n_{21} \\ -n_{12} & n_{11} \end{pmatrix} \tag{B.12}$$

where:

$$det\ N = n_{11}n_{22} - n_{21}n_{12} \tag{B.13}$$

This is equivalent to the result given without proof by Clarke [1].

Turning to the case of the high calcium coverage surface described in section 7.3.3, if $\mathbf{b}_1$ is taken to be the longer reciprocal space vector of the substrate (horizontal

in figure 7.8 on page 160), as is usual in LEED studies then the reciprocal space unit cell is described by the vectors:

$$\begin{aligned} \mathbf{b_1^{rec}} &= \frac{\mathbf{b_1}}{2} + \frac{\mathbf{b_2}}{10} \\ \mathbf{b_2^{rec}} &= \mathbf{b_2} \end{aligned} \tag{B.14}$$

which is equivalent to the matrix:

$$N = \begin{pmatrix} \frac{1}{2} & \frac{1}{10} \\ 0 & 1 \end{pmatrix} \tag{B.15}$$

hence the real space unit cell is described by the matrix:

$$M = 2 \begin{pmatrix} 1 & 0 \\ -\frac{1}{10} & \frac{1}{2} \end{pmatrix} = \begin{pmatrix} 2 & 0 \\ -\frac{1}{5} & 1 \end{pmatrix} \tag{B.16}$$

In the present case *det* $N$ is a rational fraction indicating that the substrate and overlayer lattices come into coincidence at regular intervals, the surface is best described as a coincidence lattice [2].

# References

[1] L.J. Clarke. *Surface crystallography - An introduction to low energy electron diffraction.* Wiley-Interscience, 1985.

[2] D.P. Woodruff and T.A. Delchar. *Modern techniques of surface science.* Cambridge university press, 2nd edition, 1994.